Distributed Cooperative Communications and Wireless Power Transfer

by

Rui Wang

A Dissertation

Submitted to the Faculty

of the

WORCESTER POLYTECHNIC INSTITUTE

In partial fulfillment of the requirements for the

Degree of Doctor of Philosophy

in

Electrical and Computer Engineering

by

February 2018

APPROVED:

Professor D. Richard Brown III, Major Advisor

Professor Lifeng Lai, Department of ECE, UC Davis

Professor Andrew G. Klein, Department of Engineering and Design, WWU

To my family.

Abstract

In telecommunications, distributed cooperative communications refer to techniques which allow different users in a wireless network to share or combine their information in order to increase diversity gain or power gain. Unlike conventional point-to-point communications maximizing the performance of the individual link, distributed cooperative communications enable multiple users to collaborate with each other to achieve an overall improvement in performance, e.g., improved range and data rates.

The first part of this dissertation focuses the problem of jointly decoding binary messages from a single distant transmitter to a cooperative receive cluster. The outage probability of distributed reception with binary hard decision exchanges is compared with the outage probability of ideal receive beamforming with unquantized observation exchanges. Low-dimensional analysis and numerical results show, via two simple but surprisingly good approximations, that the outage probability performance of distributed reception with hard decision exchanges is well-predicted by the SNR of ideal receive beamforming after subtracting a hard decision penalty of slightly less than 2 dB. These results, developed in non-asymptotic regimes, are consistent with prior asymptotic results (for a large number of nodes and low per-node SNR) on hard decisions in binary communication systems.

We next consider the problem of estimating and tracking channels in a distributed transmission system with multiple transmitters and multiple receivers. In order to track and predict the effective channel between each transmit node and each receive node to facilitate coherent transmission, a linear time-invariant state-space model is developed and is shown to be observable but nonstabilizable. To

quantify the steady-state performance of a Kalman filter channel tracker, two methods are developed to efficiently compute the steady-state prediction covariance. An asymptotic analysis is also presented for the homogenous oscillator case for systems with a large number of transmit and receive nodes with closed-form results for all of the elements in the asymptotic prediction covariance as a function of the carrier frequency, oscillator parameters, and channel measurement period. Numeric results confirm the analysis and demonstrate the effect of the oscillator parameters on the ability of the distributed transmission system to achieve coherent transmission.

In recent years, the development of efficient radio frequency (RF) radiation wireless power transfer (WPT) systems has become an active research area, motivated by the widespread use of low-power devices that can be charged wirelessly. In this dissertation, we next consider a time division multiple access scenario where a wireless access point transmits to a group of users which harvest the energy and then use this energy to transmit back to the access point. Past approaches have found the optimal time allocation to maximize sum throughput under the assumption that the users must use all of their harvested power in each block of the "harvest-then-transmit" protocol. This dissertation considers optimal time and energy allocation to maximize the sum throughput for the case when the nodes can save energy for later blocks. To maximize the sum throughput over a finite horizon, the initial optimization problem is separated into two sub-problems and finally can be formulated into a standard box-constrained optimization problem, which can be solved efficiently. A tight upper bound is derived by relaxing the energy harvesting causality.

A disadvantage of RF-radiation based WPT is that path loss effects can significantly reduce the amount of power received by energy harvesting devices. To overcome this problem, recent investigations have considered the use of distributed transmit beamforming (DTB) in wireless communication systems where two or more

individual transmit nodes pool their antenna resources to emulate a virtual antenna array. In order to take the advantages of the DTB in the WPT, in this dissertation, we study the optimization of the feedback rate to maximize the energy efficiency in the WPT system. Since periodic feedback improves the beamforming gain but requires the receivers to expend energy, there is a fundamental tradeoff between the feedback period and the efficiency of the WPT system. We develop a new model to combine WPT and DTB and explicitly account for independent oscillator dynamics and the cost of feedback energy from the receive nodes. We then formulate a "Normalized Weighted Mean Energy Harvesting Rate" (NWMEHR) maximization problem to select the feedback period to maximize the weighted averaged amount of net energy harvested by the receive nodes per unit of time as a function of the oscillator parameters. We develop an explicit method to numerically calculate the globally optimal feedback period.

ACKNOWLEDGEMENTS

There are so many people I want to thank, for without their help and accompany, I would have never made it this far. My words here are insufficient to capture all of my appreciation.

First, and most importantly, I want to thank Mom and Dad unconditional support and love. They are the people who give me life and are my personal heroes in the world. They have been my guides in this world from my first, tentative, unsure steps, both as an infant and as a young man attending university aboard. No matter where I am or how much space, or how many zones, separate us, they always give me power and encourage me to struggle in front of difficulties. I am forever indebted to them.

I feel incredibly fortunate to have the most awesome Professor Rick Brown as my advisor. I am very appreciated that he promoted me to a Ph.D. student after one year entering WPI when I was a master at that time. I have been extremely lucky to have a supervisor who cared so much about my work, and who responded to my questions and queries so promptly. I am very thankful to him for his efforts on helping me to understand problems, revise each paper and bring new ideas to my research. His advice on both research as well as on my career have been priceless.

Besides my advisor, I am thankful to the rest of my dissertation committee members, Professor Lai and Professor Andy Klein, for reviewing my dissertation, participating in my dissertation defense, and for asking me challenging questions and giving me professional comments on my dissertation. I also thank them for always being kind enough to give me valuable comments and ideas on my research.

I would also like to thank everyone who I interacted with over the weekly teleconference calls. I want to thank Professor Dasgupta for letting me cooperate with him and Professor Madhow for his insightful feedback and comments on my first

paper in life.

Thanks also go to my current/previous labmates at WPI who all make my experience here special. I would like to thank Min who gave me lots of unselfish helps both in research and daily life when I entered the laboratory. I would also like to thank my other labmates who have made the lab a better workplace: Radu, Sabah, Shahab, Kirty, Kim.

Finally, I wish to thank my friends Chenyun and Bingwen, who were also my roommates during the second year of my Ph.D. career. I am grateful to them not only for their insights and discussions on many problems and also lots of unselfish helps in my daily life.

BIOGRAPHICAL SKETCH

Rui Wang was born and raised in Nanjing, which is not only the largest but also a famous historical city in Jiangsu province in China. Being the only child of Xiaowei Wang and Chungui Wang, he is receiving meticulous care and high expectations from his parents since he was born, which made him a carefree and happy childhood. When he grew up to 4 years old, he showed great interest in art, especially in drawing. He often stood alone on the balcony for a whole afternoon to observe the opposite buildings, the people walking on the street, the distant mountains, and the birds flying in the sky, and then drew them all down. His drawings impressed one teacher in an art school and she thought he was gifted in painting and suggested his parents to send him to art school. His parents are quite happy after hearing that and treated him as a future artist.

After entering the elementary school, Rui gradually lost interest in drawing, instead, he showed much more curiosity in science. He often liked to talk about the Loch Ness Monster, the Sasquatch, and E.T. in front of his little friends after reading the stories in the books. He dreamed that he could be a scientist one day in the future to unveil all those mysteries. During his second year of the primary school, he met one of the most important teachers during his life, a young professor from the department of the biology of Nanjing Normal University, who wanted to carry out the extracurricular activities in the elementary school. After participating in those activities, he was deeply attracted by the amazing world of creatures. Every day after school, regardless of wind or rain, with the schoolbag on his back, he always went into the mountains that were located in the university. There was only one thing he wanted to do was to observe and record the species and habits of the birds in the university. Under the guidance of the young professor, after one year's observations and recordings, he finished his first "academic" paper in his life within

2 weeks. This was the first time that he attempted to read other's academic papers and solve problems independently, which he thought was a precious experience in his early time and had a far-reaching impact to his future Ph.D. career.

In 2004, Rui was recommended for admission to the High School Affiliated to Nanjing Normal University, one of the top high schools in Nanjing, due to his good performance in the junior high school. In the high school, Rui met a lot of talented schoolmates. They were a group of smart guys, who were always full of new ideas and strong desires for knowledge. With the communications of them, Rui was gradually addicted to physics since he found that solving difficult problems in physics made him feel fulfilled and satisfied. Rui then participated in the physics competitions every year and obtained quite good performance. He thought he should enter the department of physics and continued learning physics in university. However, this time, his parents opposed him to enter the department of physics, instead, they wanted him to learn engineering in the university. After thinking for a long time, Rui made an important decision in his life: entering the department of electrical and computer engineering in university, which he thought he made a good choice several years later.

In 2007, after taking the national higher education entrance exam, Rui successfully entered the department of electrical and computer engineering of Nanjing University of Aeronautics and Astronautics (NUAA), which is one of the top engineering universities in Jiangsu province. In the university, he met another most important teacher in his life, Zhiming Gu, a professor from the department of mathematics. He was the mentor who led Rui to the sacred palace of mathematics and taught him how to learn mathematics in the correct ways. Until nowadays, Rui still remembers those impressive words from the professor, for example, "Every theorem in the book is the most important exercise and every exercise in the book is the

least important theorem." Those words are just like the lighthouse in the darkness, guiding Rui to learn the scientific knowledge and do the research in his later Ph.D. career.

After Rui's graduation from the university, he decided to study abroad. Fortunately, he was accepted by the department of electrical and computer engineering of Worcester Polytechnic Institute (WPI) in 2011 fall as a master student. More luckily, he was promoted to a Ph.D. student by Professor Brown after one year's study in WPI due to his good performance in the course of ECE 503 (Digital Signal Processing) and Professor Brown, who is also one of the most important teacher in Rui's life, became Rui's advisor for his Ph.D. program. After entering the signal processing and information networking laboratory (SPINLAB) in 2012 fall, Rui enjoyed the daily life in the lab: reading papers, writing papers, making discussion with Professor Brown, which might be tedious in the eyes of others, and Rui thought he was one step closer to his childhood dream.

As Rui completes his studies at WPI this spring, he decides to go to work in the industry. Although finding a job is a tough process, Rui believes that all is not gold that glitters and he will never give up and enjoy what life offers him.

Contents

List of Figures

List of Tables

List of Abbreviations

Abbreviation	Meaning
SNR	signal-to-noise ratio
RF	radio frequency
WPT	wireless power transfer
DTB	distributed transmit beamforming
WISP	wireless identification and sensing platform
IC	inductive coupling
IC-WPT	inductive coupling-based wireless power transfer
MRC	magnetic resonant coupling
MRC-WPT	magnetic resonant coupling-based wireless power transfer
PTE	power transmission efficiency
SWIPT	simultaneous wireless information and power transfer
MIMO	Multi-Input Multi-Output
CSIT	channel state information at the transmitter
TDD	time-division duplexed
NWMEHR	normalized weighted mean energy harvesting rate

List of Symbols

Symbol	Meaning
$\mathbb{N}^+$	nonzero natural numbers
$\mathbb{R}$	real numbers
$\mathbb{R}^{a\times b}$	the space of $a \times b$ matrices with real entries
$\boldsymbol{I}_n$	$n \times n$ identity matrix
$\mathbf{1}_n$	a length n vector of all ones
$\otimes$	Kronecker product
$\boldsymbol{S} \succ \mathbf{0}$	$\boldsymbol{S}$ is positive definite for a symmetric matrix
$\lvert\boldsymbol{R}\rvert$	the determinant of $\boldsymbol{R}$ for a square matrix
$\lVert\boldsymbol{M}\rVert_F$	Frobenius norm of $\boldsymbol{M}$ for an arbitrary-size matrix
$\boldsymbol{M}^{\mathrm{T}}$	transpose of $\boldsymbol{M}$ for an arbitrary-size matrix
$\mathcal{N}(\mu, \sigma^2)$	the distribution of a Gaussian random vector with mean μ and variance σ^2
$\overset{\text{i.i.d.}}{\sim}$	"independent and identically distributed as"
$\mathbb{E}[\cdot]$	statistical expectation
cov	statistical covariance
$f(x) = O(g(x))$ for $x \to 0$	there exist constants $\epsilon > 0$ and C such that $\lvert f(x)\rvert \leq C\lvert g(x)\rvert$ for all x with $\lvert x\rvert < \epsilon$
$\int_{x\in A} f(x)\, dx$	the integration of $f(x)$ over a specified set $A \subseteq \mathbb{R}$

Chapter 1

Introduction.

With the explosive growth in the use of Internet and wireless services, such as smartphones, HD video streaming and real-time gaming, etc., in recent years, the data rate and quality of service requirements for the next generation of wireless devices have an order of magnitude higher in order to meet the increasing demands of such a large variety of high-data-rate multimedia services, for which the conventional point-to-point communication can no longer meet. To overcome this situation, in wireless communications, a break-through is the innovation of cooperative communication, which allows different users or nodes in a wireless network to share resources to create collaboration through distributed transmission/reception. It presents a new communication paradigm promising significant improvement in system capacity and reliability. Although wireless networks have existed for many years already, explicit concern about their energy efficient operation has emerged only recently. Prolonging the lifetime of battery powered devices in wireless networks is becoming a significant problem due to the widespread use of those devices. Recently, wireless power transfer (WPT) using radio frequency signals is attracting attention as a viable approach to the energy harvesting problem. A disadvantage of all WPT techniques

over longer ranges is that path loss effects can significantly reduce the amount of power received by energy harvesting devices. To overcome this problem, recently, researchers have considered the use of distributed transmit beamforming (DTB) in wireless communication systems where two or more individual transmit nodes pool their antenna resources to emulate a virtual antenna array, which naturally allows for low-cost deployment of robust large-aperture arrays suitable for efficient wireless communications and WPT.

1.1 Motivation.

In the last two decades, the advantages of multiple-input multiple-output (MIMO) systems have been widely acknowledged, to the extent that certain transmit diversity methods (i.e., Alamouti signaling) have been incorporated into wireless standards. Although transmit diversity is clearly advantageous on a cellular base station, it may not be practical for other scenarios. Specifically, transmit diversity generally requires more than one antenna at the transmitter. However, in many applications, such as sensor networks and ad-hoc networks, wireless devices are limited by size or hardware complexity to one antenna [115]. To overcome these situations, cooperative communications have been proposed to exploit the spatial diversity gains inherent in multiuser wireless systems without the need of multiple antennas at each node [66, 111, 113, 114, 133]. The basic idea of cooperative communication is to allow users to cooperate in transmitting and/or receiving at the physical layer in a manner that forms a virtual multi-antenna system. Cooperative communication can be applied in a wide variety of wireless networks including sensor networks, cellular networks, and ad-hoc networks [111, 133].

Distributed reception is a technique where multiple receivers in a wireless net-

work combine their observations to increase diversity and power gain and, consequently, improve the probability of successfully decoding noisy transmissions. In 1983, cooperative reception was the first time to be applied in the context of aperture synthesis for radio astronomy, e.g., the Very Large Array [92], where each antenna typically forwards observations over a high-speed optical backhaul network to a processing center for subsequent alignment and combining.

Recently, the distributed reception has been considered for wireless networks with limited backhaul capabilities. For example, soft handoff [93, 132], has been successfully used in cellular systems since the 1990s. Recent information-theoretic studies [5, 61, 108, 134] have shown that more sophisticated cooperative reception techniques have significant potential to increase diversity, improve capacity, and improve interference rejection, even with tight backhaul constraint.

Distributed transmit beamforming (DTB) is a form of cooperative communication in which two or more information sources simultaneously transmit a common message and control the phase of their transmissions so that the signals constructively combine at an intended destination. Ideal DTB with N antennas results in an N^2-fold gain in received power. Compared to single-antenna transmission, DTB can therefore yield increased range (an N-fold increase for free space propagation), increased rate (an N^2-fold increase in a power-limited regime), or increased power efficiency (an N-fold decrease in the net transmitted power for a fixed desired received power) [83]. Moreover, since more power is directed in the desired direction, less is scattered in undesired directions, resulting in reduced interference and increased security [83]. In order to perform DTB using a network of cooperating single-antenna sources, the sources must agree on a common message, transmit it at the "same time", synchronize their carrier frequencies, and control their carrier phases so that their signals combine constructively at the destination. Hence, practical realization

of this concept requires the development of implementable distributed techniques for information sharing, timing synchronization, and carrier synchronization, which becomes especially complicated in a large-scale distributed Multi-Input Multi-Output (MIMO) system.

Since coherent transmission techniques require channel state information at the transmitters (CSIT), several techniques have been proposed to address this issue for distributed MIMO systems, with the goal of providing CSIT either implicitly or explicitly. These include receiver-coordinated explicit feedback [17, 18, 32, 33, 35, 50, 129], receiver-coordinated summarized feedback [86–88], master-slave synchronization with retrodirective transmission [82], round-trip retrodirective transmission [19, 34, 98], and two-way synchronization with retrodirective transmission [102, 103]. Each of these techniques has advantages and disadvantages in particular applications, as discussed in the survey article [85].

Although wireless networks have existed for many years already, explicit concern about their energy efficient operation has emerged only recently. With the widespread use of battery powered devices in daily life, such as cell phones, laptops, tablets, etc., prolonging the lifetime of those devices in wireless networks becomes a significant problem [53]. Replacing or recharging batteries may be inconvenient (e.g., for a sensor network with massive distributed sensor nodes), dangerous (e.g., for devices positioned in toxic environments), or even impossible (e.g., for the medical sensors implanted inside human bodies) [136]. To overcome such situations, *wireless power transfer* (WPT), which generally refers to the transmissions of electrical energy from a power source to one or more electrical loads without any interconnecting wires, has become an attractive approach with the potential of extending the lifetime of these devices.

WPT technologies can be dated back to early 20th century. Nikola Tesla, a

pioneering electronic engineer, invented the Tesla Coil aiming to produce radial electromagnetic waves with about 8 Hz frequency transmitted between the earth and its ionosphere, thereby transferring energy [81]. Nowadays, WPT is widely used in daily life for charging mobile devices and have been proved useful in wireless sensor networks, whose lifetime can be extended [48, 95, 97, 116]. For the time-varying electromagnetic field, there are two main types of WPT technologies, the near-field WPT and the far-field WPT [104]. The near-field WPT is non-radiative and can transfer energy over a distance of less than one wavelength. Inductive coupling (IC) is a popular near-field WPT technique, in which the transmitter and receiver coils together form a transformer and power is transferred between the coils by a magnetic field [110]. One significant drawback of the IC-based WPT (IC-WPT) is its short transmission distance. Moreover, when the transmitter coil and the receiver coil are not well aligned, the power transmission efficiency (PTE) drops significantly. Despite these weaknesses, IC-WPT is often advantageous with respect to its simple design and high safety, therefore has been broadly used in many applications including the charging of toothbrush, laptops, mobile phones, and medical implants [81]. Compared with the IC technique, the magnetic resonant coupling (MRC) technique can transfer power to a longer distance. Furthermore, since it is non-radiative, MRC does not require line of sight and has almost no harm to human [142]. However, similar to the IC, the MRC technique is also sensitive to misalignment. Moreover, it is difficult to adjust the resonance frequency when charging multiple devices [78].

Radiative power transfer, or far-field WPT technique, uses the propagation of electromagnetic waves in long distance. In particular, recently, the development of efficient radio frequency (RF) radiation WPT systems has become an active research area, motivated in part by the widespread use of low-power devices that can be

charged wirelessly [30]. Different from IC-WPT and MRC-WPT, which operate in the near-field, RF-WPT can be more efficient over longer range links and can be suitable for powering a larger number of devices distributed in a wide area [74]. On the other hand, since RF signals that carry energy can at the same time be used as a vehicle for transporting information, RF-WPT can be used for simultaneous wireless information and power transfer (SWIPT) [30].

A disadvantage of all WPT techniques over longer ranges is that path loss effects can significantly reduce the amount of power received by energy harvesting devices. To overcome this problem, recent investigations have considered the use of transmit beamforming with RF-WPT, e.g., [143,144]. To achieve coherency in a narrowband setting, the transmit array must have estimates of the channel phases to each receive node. This channel state information at the transmitter (CSIT) is typically obtained via feedback from the receive nodes. Alternatively, in systems with channel reciprocity, e.g., time-division duplexed (TDD) channels, CSIT can be obtained by having the transmitter directly estimate the channel phases from periodic sounding signals transmitted by the receive nodes. Irrespective of the method in which the CSIT is obtained, the transmit array uses the CSIT to adjust the phases of the passband transmissions so that the signals constructively combine at the intended receiver and the efficiency of WPT is improved.

While transmit beamforming can be more efficient than omnidirectional radiation, a limitation of these techniques is that they require the transmitter to have an antenna array with elements spaced sufficiently far apart to provide a desired level of directivity. The required antenna spacing of a conventional transmit beamformer is typically a significant fraction of a carrier wavelength, e.g., half wavelength or quarter wavelength antenna spacing, and hence the actual antenna separation may be quite large at carrier frequencies of interest for WPT over distance. Moreover,

to achieve significant power gains from the transmit beamformer, many antenna elements may be necessary. Hence, a conventional transmit beamforming system for WPT over distance may be quite large and costly and may also be difficult to deploy in some WPT applications, e.g., wireless charging.

Recently, researchers have considered the use of *distributed* transmit beamforming (DTB) in wireless communication systems where two or more individual transmit nodes pool their antenna resources to emulate a virtual antenna array [83]. In principle, the distributed array works in the same way as the conventional (centralized) array: the individual transmit nodes use the CSIT obtained either by feedback ("feedback-based" DTB, e.g., [31,46,71,89,112,137]) or through channel reciprocity ("reciprocity-based" DTB, e.g., [84, 103]) to form a beam by controlling the phase of their passband transmissions so that the signals constructively combine at an intended receive node. Unlike conventional transceivers, however, a distributed transmit beamformer naturally allows for low-cost deployment of robust large-aperture arrays suitable for efficient wireless communications and WPT.

Figure 1.1 shows an example wireless charging application of DTB for WPT. The goal in this setting is for the receive nodes (the $N_r = 4$ cellphones shown on the table in Figure 1) to charge wirelessly by receiving power from the transmit nodes (the $N_t = 5$ white boxes mounted on the walls of the room in Figure 1.1. Note that the transmit nodes are autonomous and are not connected to a central controller. To facilitate efficient WPT, the receive nodes periodically estimate the forward link channels and provide channel state feedback to the transmit nodes. The transmit nodes use the CSIT to form beams toward the receive nodes and the receive nodes use energy harvesting devices to collect the wireless energy and charge their batteries.

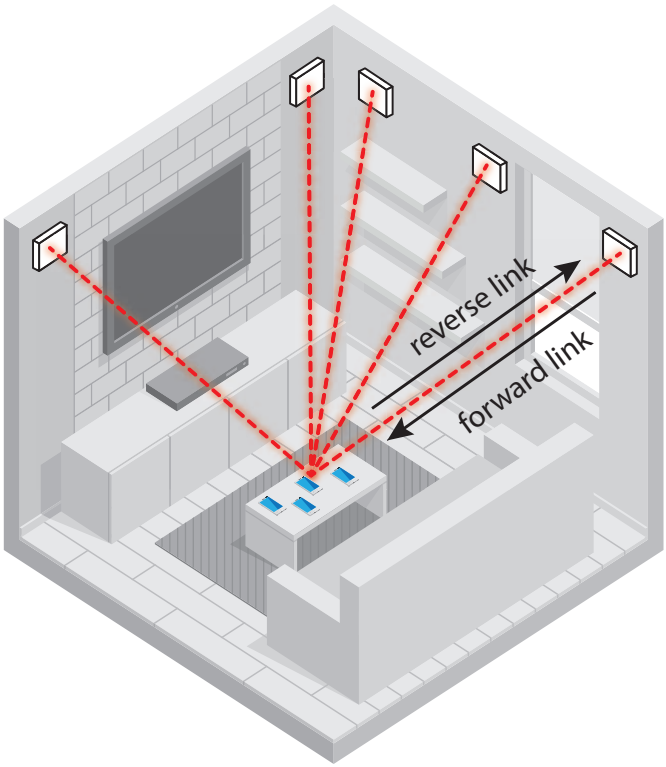

Figure 1.1: System model example with $N_t = 5$ transmit nodes and $N_r = 4$ receive nodes.

1.2 Dissertation Overview

The main body of this dissertation is organized into four chapters:

- Outage Probability Analysis of Distributed Reception with Hard Decision Exchanges (Chapter 2).
- Channel State Tracking for Large-Scale Distributed MIMO Communication Systems (Chapter 3).
- Throughput Maximization in Wireless Powered Communication Networks with Energy Saving (Chapter 4).
- Optimal Wireless Power Transfer with Distributed Transmit Beamforming (Chapter 5).

and is followed by a conclusion and a discussion of potential research below.

Chapter 2 considers the problem of jointly decoding binary messages from a single distant transmitter to a cooperative receive cluster. The goal is to communicate messages over the forward link from the distant transmitter to all of the receive nodes. The receive nodes form a fully-connected network and can reliably exchange information to jointly decode the messages from the distant transmitter. In this chapter we analyze the outage probability of distributed reception with hard decision exchanges in the case of a binary modulated forward link and independent and identically distributed Rayleigh fading forward link channels. Unlike [21] where locally unquantized information at each receive node is combined with the quantized information from other receive nodes, we make the simplifying assumption that all observations are either quantized (distributed reception with hard decision exchanges) or unquantized (ideal receive beamforming). Low-dimensional analysis and numerical results show, via two simple but surprisingly good approximations,

that the outage probability performance of distributed reception with hard decision exchanges is well-predicted by the SNR of ideal receive beamforming after subtracting a hard decision penalty of slightly less than 2 dB.

Chapter 3 considers the problem of estimating and tracking channels in a distributed transmission system with N_t transmit nodes and N_r receive nodes. The transmit cluster is assumed to use coherent transmission techniques, e.g., distributed beamforming [82], distributed nullforming [35], and/or distributed zero-forcing beamforming [148]. In this chapter, we focus on the receiver-coordinated explicit feedback scenario in which the receive cluster measures the channels and provides explicit feedback to the transmit cluster to facilitate coherent transmission. We consider a scenario in which the effective channels are tracked by one or more Kalman filters. Unlike the prior works focusing on tracking and correcting clock offsets between a single pair of nodes, we generalizes this idea to tracking a matrix of clock offsets corresponding to the collection of effective channels between all of the transmitters and receivers. A system with unified tracking achieves optimal performance by exploiting the correlations across all of the effective channels is studied in this chapter. As verified in the numerical results, unified tracking can significantly outperform approaches which separately track the phases of each oscillator.

Chapter 4 considers wireless power transfer (WPT) system called a "wireless powered communication network" (WPCN). A WPCN is a network in which wireless devices are powered *only* by WPT [54]. The WPCN model considered in this chapter is the same as in [54]. In [54], a block transmission model was considered where it was assumed that users harvest energy during a downlink transmission the first part of the block and then each user uses *all* of their harvested energy during an uplink transmission later in that block. This chapter is a generalization of the system considered in [54] where the users can save energy harvested in the current block for

wireless information transmission (WIT) in later blocks. We consider the problem of maximizing the sum throughput over a finite horizon with energy saving. The analysis assumes an "oracle" provides knowledge of the channel states for all blocks prior to the commencement of the first block. Hence, the results developed in this chapter can be considered an upper bound for finite-horizon energy saving schemes with causal channel knowledge.

Chapter 5 considers the performance of wireless power transfer (WPT) with distributed transmit beamforming (DTB) in a narrowband setting. One or more receive nodes, each equipped with energy harvesting and storage capabilities, provide periodic channel state feedback to a cluster of transmit nodes, each with an independent local oscillator, to facilitate beamforming and passband signal alignment for efficient WPT. Without channel state feedback, the transmit cluster can not align the passband signals at the receivers and the receivers can only harvest incoherent power. Since feedback improves the beamforming gain but requires the receivers to expend energy, there is a fundamental tradeoff between the feedback period and the energy harvesting efficiency. In this chapter, we develop a new model to combine WPT and DTB and explicitly account for independent oscillator dynamics and the cost of feedback energy from the receive nodes. We then formulate a "Normalized Weighted Mean Energy Harvesting Rate" (NWMEHR) maximization problem to select the feedback period to maximize the weighted averaged amount of net energy harvested by the receive nodes per unit of time as a function of the oscillator parameters. By maximizing the NWMEHR, the receive nodes maximize the *net* weighted harvested energy after feedback. Since the NWMEHR objective function is non-convex and implicit, we develop an explicit method to numerically calculate the globally optimal feedback period.

1.3 Dissertation Contributions

The main contributions of the dissertation are listed as follows:

Chapter 2:

- Analysis of the outage probability of distributed reception with hard decision exchanges in the case of a binary modulated forward link and independent and identically distributed Rayleigh fading forward link channels.
- Development of an approximated closed-form expression for the outage probability of distributed reception with hard decision exchanges.

Chapter 3:

- Analysis of the stability and steady-state behavior of a Kalman filter tracker for the effective channel states of an unsynchronized distributed MIMO communication system in the case where the magnitudes of the propagation channels are separately tracked and are slowly-varying.
- Analysis of the steady-state prediction covariance of the Kalman filter tracker
- Establishment of the existence and uniqueness of a particular positive semidefinite "strong" solution.
- Development of two methods to efficiently solve the resulting discrete-time algebraic Riccati equation (DARE) for this strong solution.
- Development of closed-form results for all of the elements in the asymptotic prediction covariance as a function of the carrier frequency, oscillator parameters, and channel measurement period.

Chapter 4:

- Generalization of the system considered in [54] where the users can save energy harvested in the current block for wireless information transmission (WIT) in later blocks. We consider the problem of maximizing the sum throughput over a finite horizon with energy saving.

- Development of an efficient numerical algorithm of solving the throughput maximization problem.

- An upper bound with low computational complexity is provided by relaxing the energy harvesting causality, which give us a water-filling typed solution.

Chapter 5:

- Development of a new model to combine WPT and DTB and explicitly account for independent oscillator dynamics and the cost of feedback energy from the receive nodes.

- Formulation of a "Normalized Weighted Mean Energy Harvesting Rate" (NWMEHR) maximization problem to select the feedback period to maximize the weighted averaged amount of net energy harvested by the receive nodes per unit of time as a function of the oscillator parameters. By maximizing the NWMEHR, the receive nodes maximize the *net* weighted harvested energy after feedback.

- Development of an explicit method to numerically calculate the globally optimal feedback period. Our method solves the problem in two steps: (i) bounding the search region into a closed interval and (ii) applying the DIRECT algorithm [52] on the bounded search region to find the globally optimal solution.

Chapter 2

Outage Probability Analysis of Distributed Reception with Hard Decision Exchanges

This chapter considers the problem of jointly decoding binary messages from a single distant transmitter to a cooperative receive cluster. The nodes in the receive cluster exchange information to decode messages from the transmitter. The outage probability of distributed reception with binary hard decision exchanges is compared with the outage probability of ideal receive beamforming with unquantized observation exchanges. Low-dimensional analysis and numerical results show, via two simple but surprisingly good approximations, that the outage probability performance of distributed reception with hard decision exchanges is well-predicted by the SNR of ideal receive beamforming after subtracting a hard decision penalty of slightly less than 2 dB. These results, developed in non-asymptotic regimes, are consistent with prior asymptotic results (for a large number of nodes and low per-node SNR) on hard decisions in binary communication systems.

2.1 Background

We consider the distributed reception scenario in Fig. 2.1 with a single distant transmitter and a cluster of k receive nodes. The goal is to communicate messages over the forward link from the distant transmitter to all of the receive nodes. The receive nodes form a fully-connected network and can reliably exchange information to jointly decode the messages from the distant transmitter, i.e., the receive cluster can perform *distributed reception*.

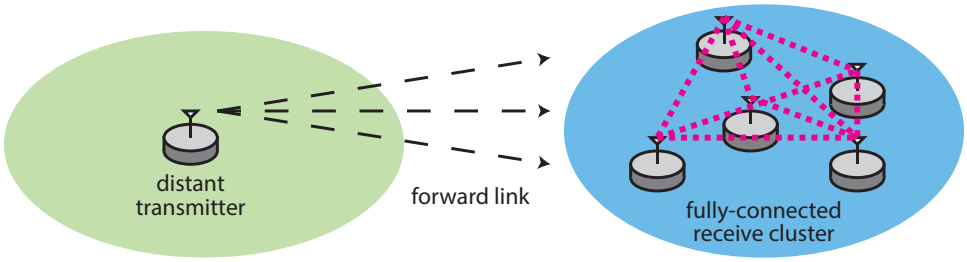

Figure 2.1: Distributed reception scenario.

Recent information theoretic studies [5, 62, 109, 135] have shown that distributed reception techniques have potential to increase diversity, improve capacity, and improve interference rejection, even with tight network throughput constraints. Several techniques have been proposed to achieve these gains including link-layer iterative cooperation [146, 147], distributed iterative receiver message-passing [26], and most-reliable/least-reliable bit exchange iterative decoding [9, 69, 70, 94, 140, 141]. A limitation of all of these techniques is that they are based on iterative transmissions and decoding. As such, the backhaul requirements are variable and the decoding latency can be significant if the number of iterations is large.

A non-iterative distributed reception technique was recently considered in [21] for the case of a binary modulated forward link. Unlike the most-reliable/least-reliable bit exchange techniques in which information is transmitted over the network based on requests from other receivers, the approach in [21] is for some or all of the receive

nodes to quantize each demodulated bit (prior to decoding) and then broadcast *all* of these quantized values to the other receivers in the cluster. The locally unquantized information at each receive node is then combined with the quantized information from other receive nodes for subsequent decoding. Numerical results showed that the outage probability penalty of exchanging binary hard decisions rather than unquantized observations (ideal receive beamforming) was less than 1.5 dB in the cases considered.

In this chapter we analyze the outage probability of distributed reception with hard decision exchanges in the case of a binary modulated forward link and independent and identically distributed Rayleigh fading forward link channels. Unlike [21] where locally unquantized information at each receive node is combined with the quantized information from other receive nodes, we make the simplifying assumption that all observations are either quantized (distributed reception with hard decision exchanges) or unquantized (ideal receive beamforming). The performance of ideal receiver beamforming depends only on the norm of the vector channel from the transmitter to the receivers, with outage occurring when this norm falls below a threshold corresponding to the particular coded modulation strategy used. While a closed-form expression for the outage probability of distributed reception with hard decision exchanges appears intractable, low-dimensional analysis and numerical results lead to simple yet accurate approximations that depend only on the norm of the vector channel. Thus, the performance of distributed reception with hard decision exchanges tracks that of ideal receive beamforming, except for a hard decision penalty. This penalty is slightly less than 2 dB in the cases considered, consistent with prior results on the penalty of hard decisions in binary communication systems [12, 22, 127].

2.2 System Model

The forward link complex channel from the distant transmitter to receive node i is denoted as g_i for $i = 1, \ldots, k$ and the vector channel is denoted as $\boldsymbol{g} = [g_1, \ldots, g_k]^\top$. Given a real-valued channel input $\sqrt{\mathcal{E}_s}X$ with $\mathbb{E}[X] = 0$, $\mathrm{var}[X] = 1$ and $\mathcal{E}_s$ denoting the energy per forward link symbol, the phase-corrected signal at the i^{th} receive node can be written as

$$Y_i = h_i X + W_i \tag{2.1}$$

where $h_i := \sqrt{2|g_i|^2\mathcal{E}_s/N_0}$, $N_0/2$ is the additive white Gaussian noise power spectral density, and $W_i \sim \mathcal{N}(0, 1)$. The quantity h_i^2 corresponds to the signal-to-noise ratio (SNR) of the forward link symbols at receive node i. For notational convenience, we define the parameter $\alpha := \sqrt{2\mathcal{E}_s/N_0}$ and note that $h_i = \alpha|g_i|$. We also denote the scaled channel magnitude vector $\boldsymbol{h} = [h_1, \ldots, h_k]^\top$.

We assume:

(1) The noise realizations are spatially and temporally independent and identically distributed (i.i.d.)

(2) The forward link complex channel g_i is constant within a symbol duration and is spatially and temporally i.i.d.

(3) The magnitude of each complex channel $|g_i|$ follows the Rayleigh(σ) distribution with $\sigma^2 = 0.5$.

The receivers can reliably exchange information to jointly decode X. We assume that each receive node quantizes its observation by making a hard decision on the transmitted symbol and then broadcasts this hard decision over the local area network to the other receive nodes. Let $Z_i = \mathcal{Q}_i(Y_i)$ where $\mathcal{Q}_i(\cdot)$ represents the quantizer at receive node i and further denote the vector channel output $\boldsymbol{Z} = [Z_1, \ldots, Z_k]^\top$.

Since communication among the receive nodes is reliable, all receive nodes know $\boldsymbol{Z}$. We consider the outage probability

$$p_{\text{out}} = \text{Prob}(I_{\boldsymbol{h}}(X; \boldsymbol{Z}) < r_{\text{out}})$$

where r_{out} is the outage rate and $I_{\boldsymbol{h}}(X; \boldsymbol{Z})$ is the mutual information of the channel $X \to \boldsymbol{Z}$ given the scaled channel magnitudes $\boldsymbol{h}$. Our focus in this paper is on a setting with equiprobable binary channel inputs X and two different receive strategies: (i) ideal receive beamforming with $Z_i = Y_i$ for all $i = 1, \ldots, k$ and (ii) distributed reception with hard decision exchanges such that $Z_i = \text{sign}(Y_i)$ for all $i = 1, \ldots, k$. Since ideal receive beamforming is optimal, it is of interest to quantify the performance loss of distributed reception with hard decision exchanges with respect to ideal receive beamforming.

2.3 Outage Probability Analysis

In this section, we analyze the outage probability of ideal receive beamforming (distributed reception with unquantized observation exchanges) and distributed reception with binary hard decision exchanges.

2.3.1 Preliminaries

We first state a well-known result that is used in the following sections. For $|g_i|$ i.i.d. Rayleigh(σ) distributed with $\sigma^2 = 0.5$, $\|\boldsymbol{g}\|^2 \sim \Gamma(k, 1)$. Thus, $\|\boldsymbol{h}\|^2 \sim \Gamma(k, \alpha^2)$. If we define the k-dimensional quadrant

$$\mathcal{H}(c) := \left\{ \boldsymbol{h} \in \mathbb{R}^k \, : \, \|\boldsymbol{h}\|^2 < c^2 \text{ and } h_i \geq 0 \, \forall i \right\} \tag{2.2}$$

we can write the probability $p_k(\alpha, c) := \text{Prob}(\boldsymbol{h} \in \mathcal{H}(c))$ as

$$\begin{aligned} p_k(\alpha, c) &= \text{Prob}(\|\boldsymbol{h}\|^2 < c^2) \\ &= \int_0^{c^2} f_{\|\boldsymbol{h}\|^2}(u)du \\ &= F_{\|\boldsymbol{h}\|^2}(c^2) \\ &= 1 - \sum_{i=0}^{k-1} \frac{1}{i!} \left(\frac{c^2}{\alpha^2}\right)^i \exp\left[-\frac{c^2}{\alpha^2}\right] \end{aligned} \tag{2.3}$$

where $f_{\|\boldsymbol{h}\|^2}()$ and $F_{\|\boldsymbol{h}\|^2}()$ denote the probability density function (pdf) and cumulative distribution function (cdf) of the Gamma-distributed random variable $\|\boldsymbol{h}\|^2$, respectively. As observed in the following section, the outage probability of ideal receive beamforming can be exactly expressed as $p_k(\alpha, c)$ with an appropriately chosen quadrant radius c.

2.3.2 Ideal Receive Beamforming

Given an unquantized observation vector $\boldsymbol{Y} = [Y_1, \ldots, Y_k]^\top$ with Y_i defined in (2.1), the ideal receive beamformer computes the scalar channel output

$$Z = \begin{bmatrix} h_1 & \ldots & h_k \end{bmatrix} \boldsymbol{Y} = \|\boldsymbol{h}\|^2 X + \tilde{W}$$

where $\tilde{W} \sim \mathcal{N}(0, \|\boldsymbol{h}\|^2)$. When $X = \pm 1$ equiprobably, the mutual information of this channel is given as [45]

$$I_{\boldsymbol{h}}(X; Z) = \frac{1}{2} J(\|\boldsymbol{h}\|) + \frac{1}{2} J(-\|\boldsymbol{h}\|) \tag{2.4}$$

with

$$J(x) := \int_{-\infty}^{\infty} \frac{1}{\sqrt{2\pi}} e^{\frac{-(u-x)^2}{2}} \log_2\left(\frac{2}{1 + e^{-2ux}}\right) du.$$

Note that (2.4) is exact but must be evaluated numerically. For $0 \leq r_{\text{out}} < 1$,

$$B(r_{\text{out}}) = \{\|\boldsymbol{h}\| \,:\, I_{\boldsymbol{h}}(X;Z) = r_{\text{out}}\} \tag{2.5}$$

has a unique solution due to the strict monotonicity of $I_{\boldsymbol{h}}(X;Z)$ as a function of $\|\boldsymbol{h}\|$. The outage probability of the binary-input ideal receive beamforming channel then follows from (2.3) as

$$p_{\text{out}}^{\text{b}\to\text{bf}} = p_k(\alpha, B(r_{\text{out}})) \tag{2.6}$$

where $\alpha = \sqrt{2\mathcal{E}_s/N_0}$.

One difficulty with (2.6) is that $B(r_{\text{out}})$ must be computed implicitly in (2.5). An explicit upper bound on the mutual information (and hence a lower bound on the outage probability) can be derived by relaxing the binary assumption on X and allowing X to be a Gaussian random variable. The mutual information in this case is

$$I_{\boldsymbol{h}}(X;\boldsymbol{Z}) = 0.5\log_2\left(1 + \|\boldsymbol{h}\|^2\right).$$

Fixing the outage rate $r_{\text{out}} \geq 0$, the strict monotonicity of $I_{\boldsymbol{h}}(X;Z)$ implies that an outage occurs if and only if $\|\boldsymbol{h}\| < A(r_{\text{out}})$ with

$$A(r_{\text{out}}) = \sqrt{2^{2r_{\text{out}}} - 1}. \tag{2.7}$$

From (2.3), the outage probability of the Gaussian-input ideal receive beamforming channel then follows as

$$p_{\text{out}}^{\text{g}\to\text{bf}} = p_k(\alpha, A(r_{\text{out}})) \tag{2.8}$$

Note that $A(r_{\text{out}}) < B(r_{\text{out}})$, hence $p_{\text{out}}^{\text{g}\to\text{bf}} < p_{\text{out}}^{\text{b}\to\text{bf}}$. As shown in Section 3.6, however,

$p_{\text{out}}^{\text{g}\to\text{bf}} \approx p_{\text{out}}^{\text{b}\to\text{bf}}$ for values of r_{out} not too close to one. Hence, (2.8) can be considered a convenient approximation for (2.6) in this regime.

2.3.3 Distributed Reception with Hard Decision Exchanges

This section analyzes the outage probability of distributed reception with binary hard decision exchanges. Unlike ideal receive beamforming, the outage region $\mathcal{H}_k(r_{\text{out}})$ of k-receiver distributed reception with hard decision exchanges for $k \geq 2$ receive nodes is *not* a simple quadrant as defined in (2.2). Nevertheless, based on low-dimensional analysis and numerical results with normalized channels, we observe that the dominant impact on performance is from the channel norm $\|\boldsymbol{h}\|$. Thus, we propose two radii, $C(r_{\text{out}})$ and $D(r_{\text{out}})$, with $B(r_{\text{out}}) < C(r_{\text{out}}) < D(r_{\text{out}})$, such that the outage probability $p_{\text{out}}^{\text{b}\to\text{hd}} \approx p_k(\alpha, C(r_{\text{out}})) \approx p_k(\alpha, D(r_{\text{out}}))$ with $p_{\text{out}}^{\text{b}\to\text{hd}} = \text{Prob}(I_{\boldsymbol{h}}(X;\boldsymbol{Z}) < r_{\text{out}})$. We then use the results in Section 2.3.1 to compute approximations on the outage probability of distributed reception with hard decision exchanges.

Two Receive Nodes

In the case with two receive nodes and binary channel inputs, we can write the mutual information of the 2×4 discrete memoryless channel as

$$\begin{aligned} I_{\boldsymbol{h}}(X;\boldsymbol{Z}) = 1 - q_1q_2\log_2\left[\frac{p_1p_2}{q_1q_2}+1\right] - p_1q_2\log_2\left[\frac{q_1p_2}{p_1q_2}+1\right] \\ - q_1p_2\log_2\left[\frac{p_1q_2}{q_1p_2}+1\right] - p_1p_2\log_2\left[\frac{q_1q_2}{p_1p_2}+1\right] \end{aligned}$$

where $p_i = Q(h_i)$ and $q_i = 1 - p_i$ for $i = 1, 2$. Denoting $\boldsymbol{p} = [p_1, p_2]^\top$ and given an outage rate $0 < r_{\text{out}} < 1$, we have

$$\begin{aligned} I_{\boldsymbol{h}}(X; \boldsymbol{Z}) < r_{\text{out}} &\Leftrightarrow \boldsymbol{p} \in \mathcal{P}_2(r_{\text{out}}) \\ &\Leftrightarrow \boldsymbol{h} \in \mathcal{H}_2(r_{\text{out}}) \end{aligned}$$

where $\mathcal{P}_2(r_{\text{out}}) \subset [0, 0.5]^2$ is the set of channel transition probabilities that result in outage and $\mathcal{H}_2(r_{\text{out}}) \subset [0, \infty)^2$ is the set of scaled channel magnitudes that result in outage. The boundary of $\mathcal{H}_2(r_{\text{out}})$ is plotted in Fig. 2.2 for the case $r_{\text{out}} = 0.5$. Note that $\mathcal{H}_2(r_{\text{out}})$ is not a simple quadrant as defined in (2.2). The boundaries of two quadrants $\mathcal{H}(C(r_{\text{out}}))$ and $\mathcal{H}(D(r_{\text{out}}))$ are also plotted in Fig. 2.2. The radii of the inner and outer quadrants were selected to match the boundary of $\mathcal{H}_2(r_{\text{out}})$ at the points $\boldsymbol{h} = [0, C(r_{\text{out}})]^\top$ and $\boldsymbol{h} = \frac{D(r_{\text{out}})}{\sqrt{2}}[1, 1]^\top$, respectively. To compute $C(r_{\text{out}})$, one can perform the following steps:

1. Set $p_2 = 0.5$ or, equivalently, $h_2 = 0$.
2. Solve $I_{\boldsymbol{h}}(X; \boldsymbol{Z}) = r_{\text{out}}$ to determine p_1 or $h_1 = Q^{-1}(p_1)$.
3. Compute $C(r_{\text{out}}) = Q^{-1}(p_1) = h_1$.

To compute $D(r_{\text{out}})$, one can perform the following steps:

1. Set $p_1 = p_2 = p$ or, equivalently, $h_1 = h_2 = h$.
2. Solve $I_{\boldsymbol{h}}(X; \boldsymbol{Z}) = r_{\text{out}}$ to determine p or $h = Q^{-1}(p)$.
3. Compute $D(r_{\text{out}}) = \sqrt{2}Q^{-1}(p) = \sqrt{2}h$.

From Fig. 2.2, it appears that $\mathcal{H}(C(r_{\text{out}})) \subseteq \mathcal{H}_2(r_{\text{out}}) \subseteq \mathcal{H}(D(r_{\text{out}}))$ in the two-receiver case, hence it is tempting to claim that $p_2(\alpha, C(r_{\text{out}}))$ and $p_2(\alpha, D(r_{\text{out}}))$

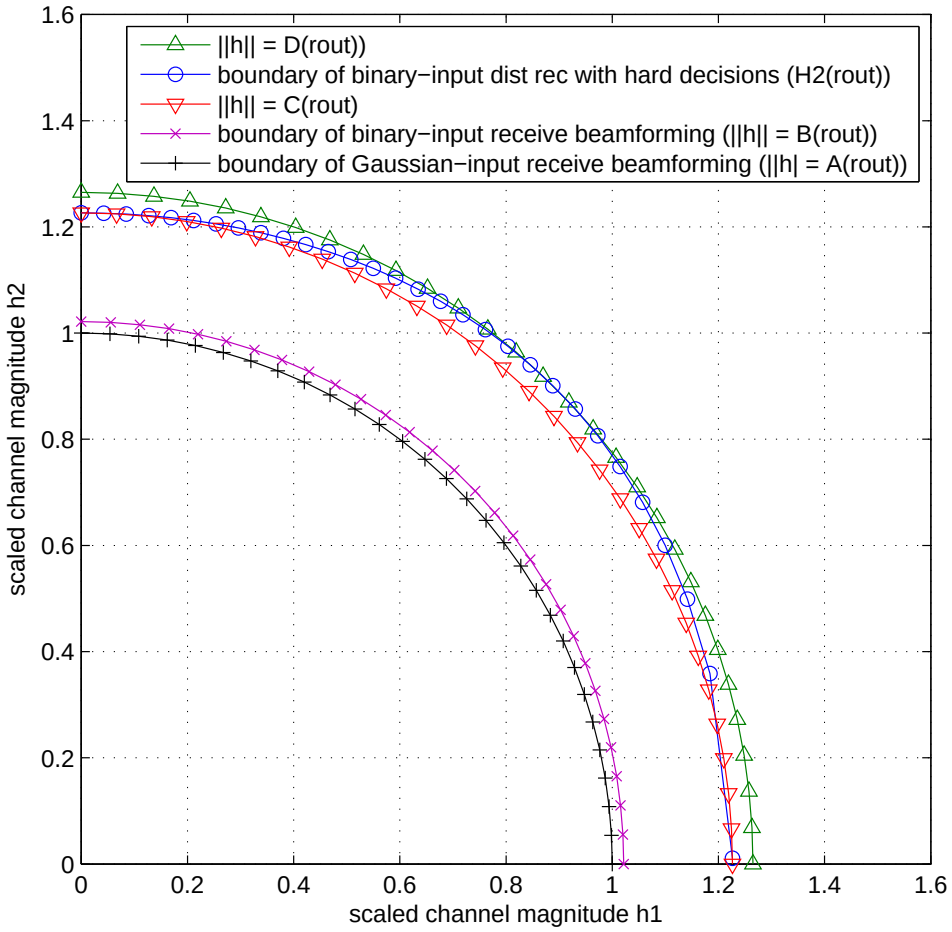

Figure 2.2: Outage regions and inner/outer quadrants for the two-receiver case with $r_{\text{out}} = 0.5$.

could serve as lower and upper bounds, respectively, for the actual outage probability $p_{\text{out}}^{\text{b}\to\text{hd}}$. A proof of this claim appears to be difficult, however, even for $k = 2$ receivers. Hence, we only claim

$$p_{\text{out}}^{\text{b}\to\text{hd}} \approx p_2(\alpha, C(r_{\text{out}})) \approx p_2(\alpha, D(r_{\text{out}})) \tag{2.9}$$

for $k = 2$ receivers with $p_{\text{out}}^{\text{b}\to\text{hd}} = \text{Prob}(I_{\boldsymbol{h}}(X; \boldsymbol{Z}) < r_{\text{out}})$ and $p_k(\alpha, c)$ defined in (2.3).

k Receive Nodes

These approximations extend immediately to the general setting of k receive nodes. We first specify two quadrants $\mathcal{H}(C(r_{\text{out}}))$ and $\mathcal{H}(D(r_{\text{out}}))$ with $C(r_{\text{out}})$ computed via the following steps:

1. Set $p_2 = \cdots = p_k = 0.5$ or, equivalently, $h_2 = \cdots = h_k = 0$.
2. Solve $I_{\boldsymbol{h}}(X; \boldsymbol{Z}) = r_{\text{out}}$ to determine p_1 or $h_1 = Q^{-1}(p_1)$.
3. Compute $C(r_{\text{out}}) = Q^{-1}(p_1) = h_1$.

Observe that this approximation (which concentrates the available channel power onto one receiver) is equivalent to ideal receive beamforming followed by a single hard decision.

Similarly, $D(r_{\text{out}})$ can be computed via the following steps:

1. Set $p_1 = \cdots = p_k = p$ or, equivalently, $h_1 = \cdots h_k = h$.
2. Solve $I_{\boldsymbol{h}}(X; \boldsymbol{Z}) = r_{\text{out}}$ to determine p or $h = Q^{-1}(p)$.
3. Compute $D(r_{\text{out}}) = \sqrt{k}Q^{-1}(p) = \sqrt{k}h$.

This approximation amounts to setting the channel gains for all receivers to be equal (and applying hard decisions at each receiver prior to information combining). Intuitively, given a channel strength budget $\|\boldsymbol{h}\|$ for distributed reception with hard decision exchanges, concentrating all of the channel strength onto one receiver should provide better performance than dispersing it across all receivers evenly.

Based on the two-receiver results, we have

$$p_{\text{out}}^{\text{b}\to\text{hd}} \approx p_k(\alpha, C(r_{\text{out}})) \approx p_k(\alpha, D(r_{\text{out}})) \tag{2.10}$$

for k receivers with $p_{\text{out}}^{\text{b}\to\text{hd}} = \text{Prob}(I_{\boldsymbol{h}}(X;\boldsymbol{Z}) < r_{\text{out}})$ and $p_k(\alpha, c)$ defined in (2.3).

To provide numerical evidence in support of the approximations, Fig. 2.3 shows the empirical distributions of the mutual information for distributed reception with hard decision exchanges for the case with i.i.d. Rayleigh channels normalized to $\|\boldsymbol{h}\| = C(r_{\text{out}})$ and $\|\boldsymbol{h}\| = D(r_{\text{out}})$ and $r_{\text{out}} = 0.5$. For each $k \in \{2, 5, 10, 20\}$, 5000 independent channel realizations were generated and the mutual information of each normalized channel realization was computed. These results show that the distribution of the mutual information of distributed reception with hard decision exchanges with channels on the outer radius $D(r_{\text{out}})$ tends to be quite close to the actual outage rate $r_{\text{out}} = 0.5$. Hence, at least in these examples, $p_k(\alpha, D(r_{\text{out}}))$ is likely to be a better approximation than $p_k(\alpha, C(r_{\text{out}}))$. This is also corroborated by the results in Section 3.6.

2.4 Numerical Results

This section provides numerical results to illustrate the effect of r_{out} and k on the radii of the outage regions and the outage probability of distributed reception. Fig. 2.4 shows the four $\|\boldsymbol{h}\|$ radii developed in Section 2.3 as a function of r_{out}

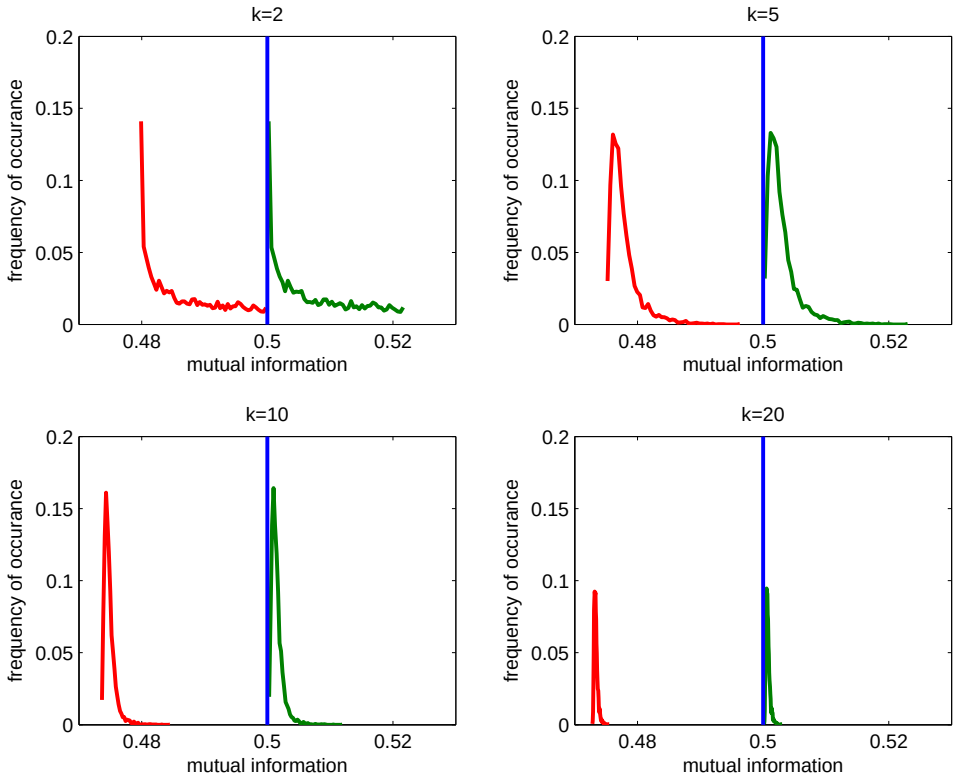

Figure 2.3: Empirical distributions of $I_{\boldsymbol{h}}(X;\boldsymbol{Z})$ for distributed reception with hard decision exchanges with normalized channels and outage rate $r_{\text{out}} = 0.5$. The red and green curves show $I_{\boldsymbol{h}}(X;\boldsymbol{Z})$ on the radii $\|\boldsymbol{h}\| = C(r_{\text{out}})$ and $\|\boldsymbol{h}\| = D(r_{\text{out}})$, respectively. The blue line is the outage rate.

for a $k = 5$ receiver system. The radius $A(r_{\text{out}})$ was computed explicitly from (2.7) and the remaining radii were computed using implicit function solvers via the procedures outlined in Section 2.3. These results show that the inner and outer radii on the outage region of distributed reception with hard decision exchanges tend to be close unless $r_{\text{out}} \to 1$. These results also show that the outage regions for ideal beamforming with binary and Gaussian inputs tend to be close unless $r_{\text{out}} \to 1$.

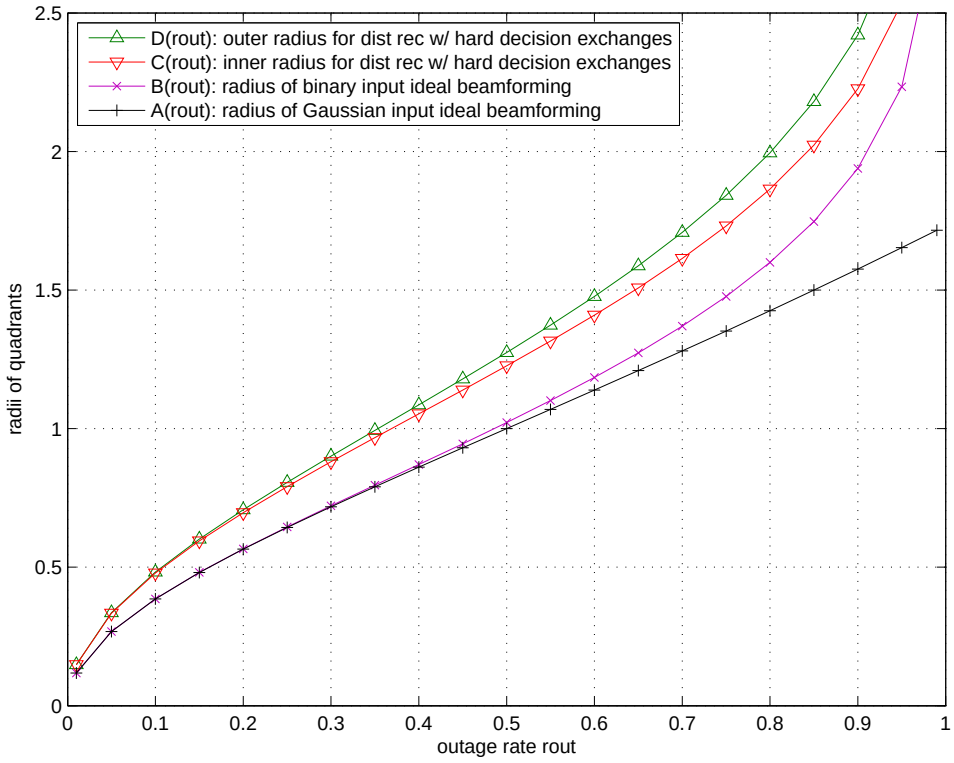

Figure 2.4: Radii of outage quadrants as a function of r_{out} for a $k = 5$ receiver distributed reception system.

Note that an approximation for the performance gap in dB between ideal receive beamforming and distributed reception with hard decision exchanges can be computed by calculating $\beta(r_{\text{out}}) = 20 \log_{10}(D(r_{\text{out}})/B(r_{\text{out}}))$ Fig. 2.5 plots this gap for $k = 2, \ldots, 20$ and $r_{\text{out}} \in \{0.1, 0.25, 0.5, 0.75, 0.9\}$. These results show that the performance gap is always slightly less than 2 dB and appears to converge as $k \to \infty$ to a

value close to the classic hard decision penalty of $10\log_{10}(\pi/2) \approx 1.96$ dB [12,22,127] for the r_{out} values tested.

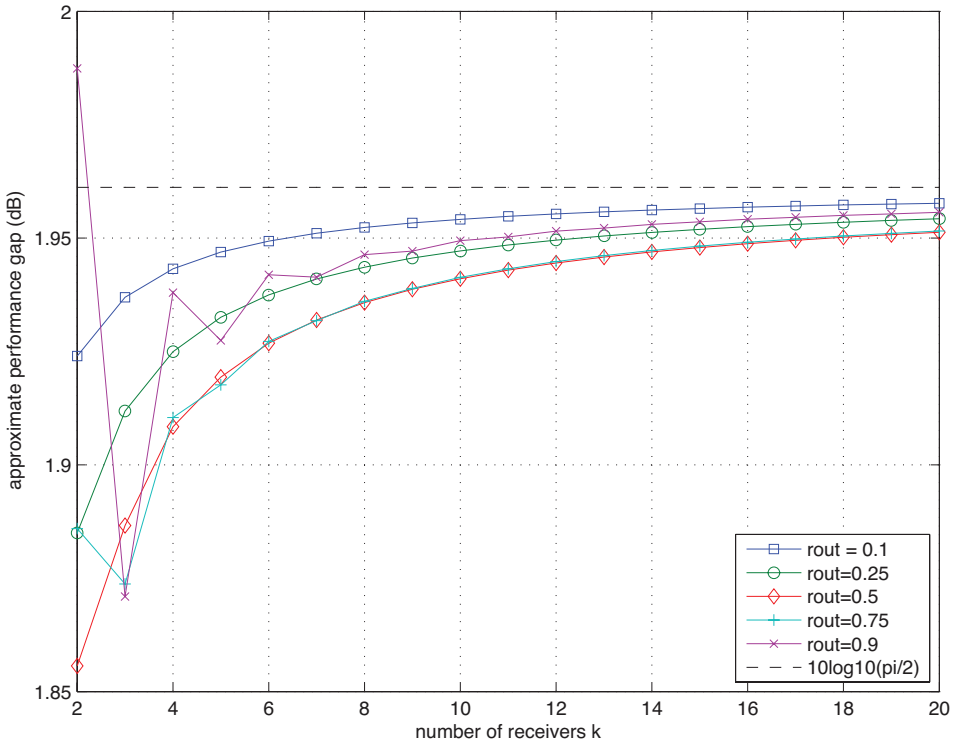

Figure 2.5: Approximate performance gap in dB between ideal receive beamforming and distributed reception with hard decision exchanges versus k and r_{out}.

Fig. 2.6 shows an outage probability simulation with outage probability plotted versus $\mathcal{E}_s/N_0$ for $k = 1, 2, 5, 10$ for a fixed outage rate $r_{\text{out}} = 0.5$. The outage probabilities were computed over 10^5 independent channel realizations with $g_i \overset{\text{i.i.d.}}{\sim} \mathcal{CN}(0, 1)$. These results show that the outage probability of distributed reception with hard decision exchanges is well-approximated by the analysis in Section2.3 and that the actual outage probability tends to be quite close to $p_k(\alpha, D(r_{\text{out}}))$ corresponding to the outer integration region. The approximation resulting from the inner integration region $p_k(\alpha, C(r_{\text{out}}))$ tends to be somewhat loose, especially for larger values of k. The gap between ideal receive beamforming and distributed reception with hard decision exchanges is consistent with Fig. 2.5. Note that the

results reported in [21] tend to be somewhat better than those shown in Fig. 2.6, especially at smaller values of k, due to the fact that the distributed reception technique in [21] combines locally unquantized information with the hard decisions from other receive nodes.

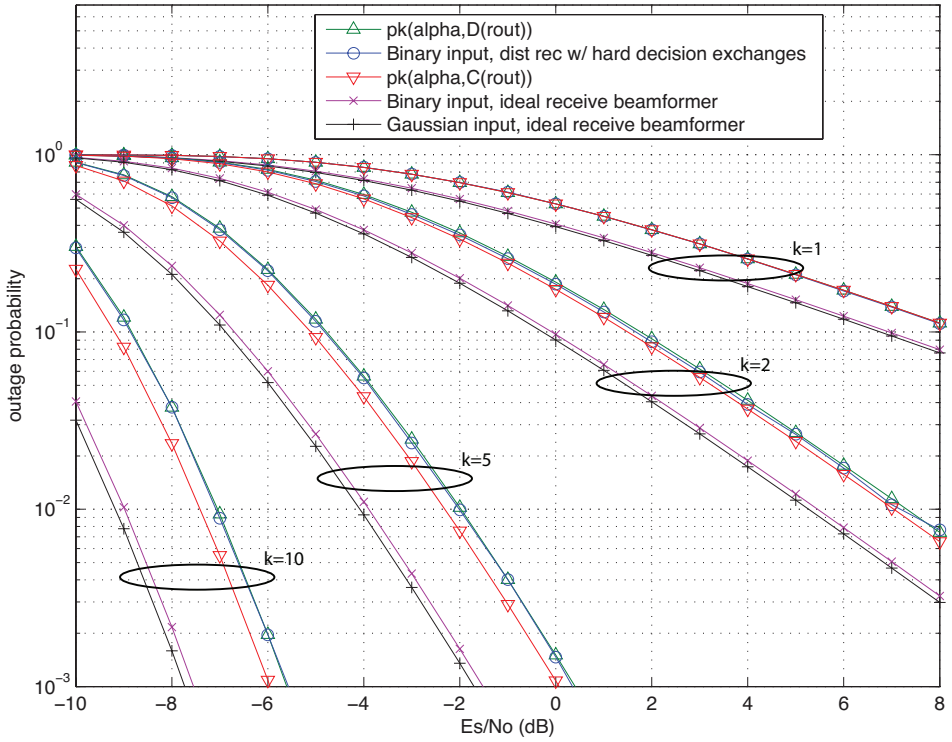

Figure 2.6: Outage probability versus $\mathcal{E}_s/N_0$ and k for ideal receive beamforming and distributed reception with hard decision exchanges with outage rate $r_{\text{out}} = 0.5$.

While hard decisions exchanges add a severe nonlinearity to the receiver processing, these numerical results show that the performance of distributed reception with hard decision exchanges is still mainly determined by the channel norm $\|\boldsymbol{h}\|$. In fact, in Fig. 2.6, the actual outage probability of distributed reception with hard decision exchanges is almost indistinguishable from the approximation $p_k(\alpha, D(r_{\text{out}}))$.

2.5 Conclusions

The numerical results in this chapter indicate that the performance of distributed reception with binary hard decision exchanges is mainly governed by the SNR obtained by ideal receive beamforming (which is proportional to the square of the norm of the vector channel to the receivers), except for a performance loss of a little less than 2 dB. For a given vector channel norm $\|\boldsymbol{h}\|$, concentrating the channel strength on one receiver gives an optimistic approximation for performance, while distributing the channel strength equally tends to give a slightly pessimistic approximation which is often close to the actual outage probability performance.

Chapter 3

Channel State Tracking for Large-Scale Distributed MIMO Communication Systems

This chapter considers the problem of estimating and tracking channels in a distributed transmission system with N_t transmit nodes and N_r receive nodes. Since each node in the distributed transmission system has an independent local oscillator, the effective channel between each transmit node and each receive node has time-varying phase and frequency offsets which much be tracked and predicted to facilitate coherent transmission. A linear time-invariant state-space model is developed and is shown to be observable but nonstabilizable. To quantify the steady-state performance of a Kalman filter channel tracker, two methods are developed to efficiently compute the steady-state prediction covariance. The first method requires the solution of a $2(N_t+N_r-1)$-dimensional discrete-time algebraic Riccati equation, but allows for nonhomogenous oscillator parameters. The second method requires the solution of four two-dimensional discrete-time algebraic Riccati equations but

requires homogenous oscillator parameters for all nodes in the system. An asymptotic analysis is also presented for the homogenous oscillator case for systems with a large number of transmit and receive nodes with closed-from results for all of the elements in the asymptotic prediction covariance as a function of the carrier frequency, oscillator parameters, and channel measurement period. Numeric results confirm the analysis and demonstrate the effect of the oscillator parameters on the ability of the distributed transmission system to achieve coherent transmission.

3.1 Background

We consider the distributed multi-input multi-output (MIMO) communication scenario in Fig. 3.1 where a transmit cluster with N_t transmit nodes communicates with a receive cluster with N_r receive nodes. The transmit cluster is assumed to use coherent transmission techniques, e.g., distributed beamforming [82], distributed nullforming [35], and/or distributed zero-forcing beamforming [148]. It is well known that coherent transmission techniques require channel state information at the transmitters (CSIT). Several techniques have been proposed to address this issue for distributed MIMO systems, with the goal of providing CSIT either implicitly or explicitly. These include receiver-coordinated explicit feedback [17,18,32,33,35,50,129], receiver-coordinated summarized feedback [86–88], master-slave synchronization with retrodirective transmission [82], round-trip retrodirective transmission [19,34,98], and two-way synchronization with retrodirective transmission [102,103]. Each of these techniques has advantages and disadvantages in particular applications, as discussed in the survey article [85].

In this chapter, we focus on the receiver-coordinated explicit feedback scenario in which the receive cluster measures the channels and provides explicit feedback to

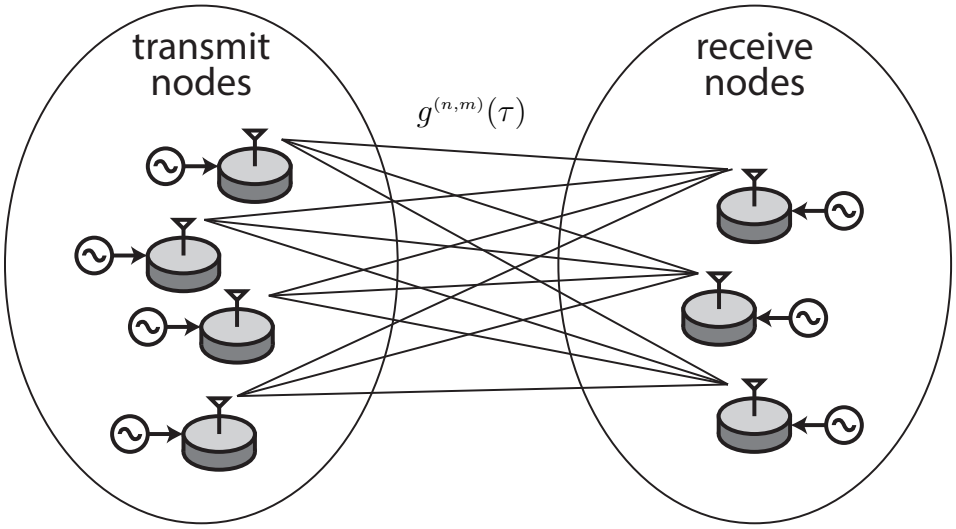

Figure 3.1: Distributed MIMO system model with N_t transmit nodes and N_r receive nodes. Each node possesses a single antenna and an independent oscillator.

the transmit cluster to facilitate coherent transmission. This approach can be used in time-division-duplex (TDD) and frequency-division-duplex (FDD) systems. We assume no external source of synchronization in the system, hence the time-varying phase and frequency offsets in each effective channel (which includes propagation as well as oscillator offsets) must be tracked and predicted to facilitate coherent transmission. We consider a scenario in which the effective channels are tracked by one or more Kalman filters.

Kalman filters have been used extensively in clock tracking and synchronization, e.g., [8, 14, 42, 58] including global positioning systems (GPS) [23], the network time protocol (NTP) [77], and the precision time protocol (PTP) [4]. The focus of this prior work, however, is on tracking and correcting clock offsets between a single pair of nodes (typically a master node such as a satellite and a slave node such as a GPS receiver). The distributed MIMO setting of Fig. 3.1 generalizes this idea to tracking a matrix of clock offsets corresponding to the collection of effective channels between all of the transmitters and receivers. Since the dynamics of these channels

are correlated, tracking channels individually is suboptimum.

A few recent papers have analyzed the performance of distributed beamforming and distributed nullforming in the distributed MIMO setting [17, 18, 32, 33] and have shown that the performance of these coherent transmission techniques can be expressed as simple functions of the channel phase prediction variance [63]. The early papers in this area made the simplifying assumption that each channel was tracked individually or each receiver tracked only its own N_t channels. While the latter approach is an improvement on tracking channels individually, it does not exploit correlations across receivers. More recently, the idea of "unified" tracking has been studied in which all of $N_t N_r$ channels in the system are jointly tracked [33]. A system with unified tracking achieves optimal performance by exploiting the correlations across all of the effective channels. As verified in the numerical results of Section 3.6 and elaborated upon in Section 3.3.3, unified tracking can significantly outperform approaches which separately track the phases of each oscillator.

This chapter is a formal analysis of the stability and steady-state behavior of a Kalman filter tracker for the effective channel states of an unsynchronized distributed MIMO communication system in the case where the magnitudes of the propagation channels $|g^{(n,m)}(\tau)|$ are separately tracked and are slowly-varying. In particular, although the state-space model for the effective channel states developed in Section 3.2 is completely observable but not stabilizable, we show that the Kalman filter is asymptotically stable subject to a properly chosen initial prediction covariance. We then analyze the steady-state prediction covariance of the Kalman filter tracker, establishing existence and uniqueness of a particular positive semidefinite "strong" solution, and develop two methods to efficiently solve the resulting discrete-time algebraic Riccati equation (DARE) for this strong solution. The first method uses a similarity transformation to cast the system in a controllable staircase form

and reduces the original $2N_tN_r$-dimensional DARE to a $2(N_t + N_r - 1)$-dimensional DARE. This method is also general in that it allows for nonhomogeneous oscillator and measurement noise parameters. The second method exploits the particular structure of the state-space model and uses a similarity transform to cast the system in a block diagonal form. When the oscillator parameters and measurement noise variance are homogenous across all nodes in the system, this method reduces to simply solving four 2-dimensional DAREs. This second method is particularly useful for large-scale systems, e.g., distributed massive MIMO systems [47,67], since the dimension of the DAREs is not a function of the transmit or receive cluster sizes. To fully characterize the behavior of the prediction covariance for large systems, we present an asymptotic analysis for the case when $N_t \to \infty$ and $N_r = \eta N_t$, and develop closed-from results for all of the elements in the asymptotic prediction covariance as a function of the carrier frequency, oscillator parameters, and channel measurement period. Numeric results confirm the analysis and demonstrate the effect of the oscillator parameters on the ability of the distributed transmission system to achieve coherent transmission.

3.2 System Model

Each node in the system shown in Fig. 3.1 is assumed to possess a single antenna. The nodes in the system are not assumed to be synchronized. The nominal transmit frequency in the forward link from the distributed transmit cluster to the receivers is at ω_c. All forward link channels are modeled as narrowband and linear. We denote the channel from transmit node n to receive node m at carrier frequency ω_c as $g^{(n,m)}(\tau) \in \mathbb{C}$ for transmit node $n = 1, \ldots, N_t$ and receive node $m = 1, \ldots, N_r$. These propagation channels, in contrast to the time-varying "effective" channels

described below, do not include the effect of carrier phase and/or frequency offsets between transmit node n and receive node m.

Fig. 3.2 shows the *effective* narrowband channel model from transmit node n to receive node m including the effects of propagation and carrier offset. Transmissions $n \to m$ are conveyed on a carrier nominally at ω_c generated at transmit node n, incur a phase shift of $\psi^{(n,m)}(\tau) = \angle g^{(n,m)}(\tau)$ over the wireless channel, and are then downmixed by receive node m using its local carrier nominally at ω_c. At time τ, the effective narrowband channel from transmit node n to receive node m is modeled as

$$\begin{aligned} h^{(n,m)}(\tau) &= g^{(n,m)}(\tau) e^{j\left(\phi_t^{(n)}(\tau) - \phi_r^{(m)}(\tau)\right)} \\ &= |g^{(n,m)}(\tau)| e^{j\phi^{(n,m)}(\tau)} \end{aligned} \tag{3.1}$$

where $\phi_t^{(n)}(\tau)$ and $\phi_r^{(m)}(\tau)$ are the local carrier phase offsets at transmit node n and receive node m, respectively, at time τ with respect to an ideal carrier reference, and

$$\phi^{(n,m)}(\tau) := \phi_t^{(n)}(\tau) + \psi^{(n,m)}(\tau) - \phi_r^{(m)}(\tau)$$

is the pairwise phase offset after propagation between transmit node n and receive node m at time τ.

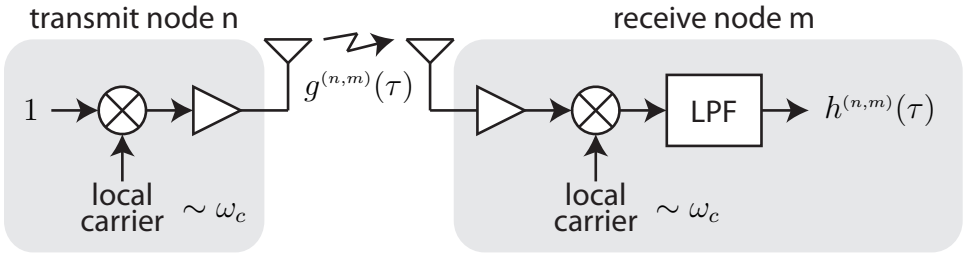

Figure 3.2: Effective narrowband channel model including the effects of propagation, transmit and receive gains, and carrier offset.

We consider an approach in which the effective channels are measured at the

receive nodes and feedback is provided by the receive nodes to the transmit nodes to facilitate coherent transmission. Note that there are two sources of independent dynamics in each effective channel: (i) propagation dynamics and (ii) oscillator dynamics. Since the oscillator dynamics do not affect the channel magnitudes, we assume that the channel magnitudes $|g^{(n,m)}(\tau)|$ are tracked separately using methods as in [60] and are slowly-varying such that they are known perfectly. The problem of estimating and tracking the effective channels $h^{(n,m)}(\tau)$ then reduces to estimating and tracking the pairwise phase offsets $\phi^{(n,m)}(\tau)$. The following sections provide an overview of basic oscillator dynamics and then develop a unified dynamic model for the phase and frequency offsets of the effective channels.

3.2.1 Oscillator Dynamics

Each local oscillator in the system has inherent frequency and phase offsets with respect to some nominal reference and also behaves stochastically, causing phase offset variations in each effective channel from transmit node n to receive node m even when the propagation channels $g^{(n,m)}$ are otherwise time invariant. This section describes a discrete-time dynamic model for the local oscillator dynamics at each transmit and receive node.

Based on the two-state oscillator models in [40, 41], we define the discrete-time state of the n^{th} transmit node's carrier as

$$\boldsymbol{x}_t^{(n)}[k] := \begin{bmatrix} \phi_t^{(n)}[k] \\ \dot{\phi}_t^{(n)}[k] \end{bmatrix}$$

where $\phi_t^{(n)}[k] = \phi_t^{(n)}(kT_0)$ corresponds to the carrier phase offset in radians at transmit node n with respect to an ideal carrier phase reference and where $T_0 > 0$ is the

state update period. The state update of the n^{th} transmit node's carrier follows

$$\boldsymbol{x}_t^{(n)}[k+1] = \boldsymbol{f}\boldsymbol{x}_t^{(n)}[k] + \boldsymbol{u}_t^{(n)}[k] \tag{3.2}$$

with

$$\boldsymbol{f} := \begin{bmatrix} 1 & T_0 \\ 0 & 1 \end{bmatrix}. \tag{3.3}$$

The local process noise vector $\boldsymbol{u}_t^{(n)}[k] \overset{\text{i.i.d.}}{\sim} \mathcal{N}\left(0, \boldsymbol{Q}_t^{(n)}\right)$ causes the carrier derived from the local oscillator at transmit node n to deviate from an ideal affine phase trajectory. The covariance of the discrete-time process noise is derived from a continuous-time model in [40] and can be written as

$$\boldsymbol{Q}_t^{(n)} = \omega_c^2 T_0 \begin{bmatrix} \alpha_t^{(n)} + \beta_t^{(n)} \frac{T_0^2}{3} & \beta_t^{(n)} \frac{T_0}{2} \\ \beta_t^{(n)} \frac{T_0}{2} & \beta_t^{(n)} \end{bmatrix} \tag{3.4}$$

where ω_c is the nominal common carrier frequency in radians per second and $\alpha_t^{(n)}$ (units of seconds) and $\beta_t^{(n)}$ (units of Hertz) are the process noise parameters corresponding to white frequency noise and random walk frequency noise, respectively. The process noise parameters $\alpha_t^{(n)}$ and $\beta_t^{(n)}$ can be estimated by fitting the theoretical Allan variance $\sigma_y^2(\tau) = \frac{\alpha_t^{(n)}}{\tau} + \frac{\beta_t^{(n)}\tau}{3}$ to experimental measurements of the Allan variance over a range of τ values. For example, a least squares fit to the Allan variance specifications for a Rakon RPFO45 oven-controlled oscillator [105] yields $\alpha_t^{(n)} = 2.31 \times 10^{-21}$ and $\beta_t^{(n)} = 6.80 \times 10^{-23}$. Typical Allan variance values for various types of oscillators are tabulated in [59].

The receive nodes in the system also have independent local oscillators used to generate carriers for downmixing that are governed by the same dynamics as (3.2) with state $\boldsymbol{x}_r^{(m)}[k]$, process noise $\boldsymbol{u}_r^{(m)}[k] \overset{\text{i.i.d.}}{\sim} \mathcal{N}(0, \boldsymbol{Q}_r^{(m)})$, and process noise parameters

$\alpha_r^{(m)}$ and $\beta_r^{(m)}$ as in (3.4) for $m = 1, \ldots, N_r$.

3.2.2 Pairwise Offset States and Observations

To facilitate coherent transmission, the receivers in the system periodically measure the effective channels from the transmit cluster and feed back their measurements to facilitate channel tracking at the transmitters as in [17, 18, 32, 33, 35]. Since the receive nodes can only observe the relative phase and frequency of the transmit nodes after propagation, we define the *pairwise offset* after propagation as

$$\boldsymbol{\delta}^{(n,m)}[k] := \begin{bmatrix} \phi^{(n,m)}[k] \\ \dot{\phi}^{(n,m)}[k] \end{bmatrix} = \boldsymbol{x}_t^{(n)}[k] + \begin{bmatrix} \psi^{(n,m)} \\ 0 \end{bmatrix} - \boldsymbol{x}_r^{(m)}[k]$$

where $\psi^{(n,m)}$ is the propagation phase[1]. Note that $\boldsymbol{\delta}^{(n,m)}[k]$ is governed by the state update

$$\boldsymbol{\delta}^{(n,m)}[k+1] = \boldsymbol{f}\boldsymbol{\delta}^{(n,m)}[k] + \boldsymbol{u}_t^{(n)}[k] - \boldsymbol{u}_r^{(m)}[k]. \tag{3.5}$$

We assume that observations are so short as to only provide useful phase estimates. An observation of the $n \to m$ channel at receive node m is then modeled as

$$y^{(n,m)}[k] = \boldsymbol{h}\boldsymbol{\delta}^{(n,m)}[k] + v^{(n,m)}[k]$$

where

$$\boldsymbol{h} := \begin{bmatrix} 1 & 0 \end{bmatrix} \tag{3.6}$$

and $v^{(n,m)}[k] \overset{\text{i.i.d.}}{\sim} \mathcal{N}(0, r)$ is scalar measurement noise with variance r assumed to be spatially and temporally i.i.d., and independent of the process noise. The measure-

[1]For clarity of exposition and consistent with previous assumptions, the propagation phase is assumed here to be slowly-varying with respect to the oscillator dynamics. If the propagation phase $\psi^{(n,m)}[k]$ is not slowly varying, its dynamics can also be incorporated in the pairwise offset state $\boldsymbol{\delta}^{(n,m)}[k]$.

ment noise variance r depends on the several factors including the signal-to-noise ratio of the channel and the duration of the measurement signal. Bounds on the measurement noise variance for maximum likelihood phase estimators are given in [106].

The use of a pairwise offset state is important in our tracking scenario since it provides states which are physically meaningful as well as observable. It is straightforward to confirm the observability of $[\boldsymbol{f}, \boldsymbol{h}]$ as defined in (3.3) and (3.6) for any $T_0 > 0$. The following section develops a unified dynamic model comprising all of the pairwise offset states in the system. We prove that this unified model is also completely observable in Section 3.2.4.

3.2.3 Unified Dynamic Model

While it is possible to track each of the pairwise offset states $\boldsymbol{\delta}^{(n,m)}[k]$ in (3.5) individually, it is straightforward to see that the pairwise offset states do not have independent dynamics. For example, $\boldsymbol{\delta}^{(1,2)}[k]$ and $\boldsymbol{\delta}^{(1,3)}[k]$ are correlated since they share a common process noise term $\boldsymbol{u}_t^{(1)}[k]$. This section develops a *unified* dynamic model for all of the pairwise offsets in the system to facilitate optimal unified tracking. As shown in [33] in a zero-forcing distributed beamforming scenario, unified tracking can provide significant gains in the depth of the nulls with respect to individual channel tracking.

We define the vector of unified pairwise offsets as

$$\boldsymbol{\delta}[k] := \begin{bmatrix} \boldsymbol{\delta}^{(1)}[k] \\ \vdots \\ \boldsymbol{\delta}^{(N_r)}[k] \end{bmatrix} \in \mathbb{R}^{2N_tN_r}$$

with

$$\boldsymbol{\delta}^{(m)}[k] := \begin{bmatrix} \boldsymbol{\delta}^{(1,m)}[k] \\ \vdots \\ \boldsymbol{\delta}^{(N_t,m)}[k] \end{bmatrix} \in \mathbb{R}^{2N_t}$$

From (3.5), the unified state dynamics follow as

$$\begin{aligned} \boldsymbol{\delta}[k+1] &= \begin{bmatrix} \boldsymbol{f} & & \\ & \ddots & \\ & & \boldsymbol{f} \end{bmatrix} \boldsymbol{\delta}[k] + \begin{bmatrix} \boldsymbol{u}_t^{(1)}[k] - \boldsymbol{u}_r^{(1)}[k] \\ \vdots \\ \boldsymbol{u}_t^{(N_t)}[k] - \boldsymbol{u}_r^{(N_r)}[k] \end{bmatrix} \\ &= \boldsymbol{F}\boldsymbol{\delta}[k] + \boldsymbol{G}\boldsymbol{u}[k] \end{aligned} \tag{3.7}$$

with $\boldsymbol{f}$ defined in (3.3), the process noise vector

$$\boldsymbol{u}[k] := \begin{bmatrix} \boldsymbol{u}_t^{(1)}[k] \\ \vdots \\ \boldsymbol{u}_t^{(N_t)}[k] \\ \boldsymbol{u}_r^{(1)}[k] \\ \vdots \\ \boldsymbol{u}_r^{(N_r)}[k] \end{bmatrix} \in \mathbb{R}^{2(N_t+N_r)}$$

with $\boldsymbol{u}[k] \overset{\text{i.i.d.}}{\sim} \mathcal{N}(0, \boldsymbol{U})$, covariance matrix

$$\boldsymbol{U} = \mathrm{E}[\boldsymbol{u}[k]\boldsymbol{u}^\top[k]] = \mathsf{blockdiag}(\boldsymbol{Q}_t^{(1)}, \ldots, \boldsymbol{Q}_t^{(N_t)}, \boldsymbol{Q}_r^{(1)}, \ldots, \boldsymbol{Q}_r^{(N_r)}) \tag{3.8}$$

, and

$$\boldsymbol{G} := \begin{bmatrix} \boldsymbol{I}_{2N_t} & \boldsymbol{J}_{2N_t} & & \\ \vdots & & \ddots & \\ \boldsymbol{I}_{2N_t} & & & \boldsymbol{J}_{2N_t} \end{bmatrix} \in \mathbb{R}^{2N_tN_r \times 2(N_t+N_r)} \tag{3.9}$$

where $\boldsymbol{J}_{2N_t} := -[\boldsymbol{I}_2, \ldots, \boldsymbol{I}_2]^\top \in \mathbb{R}^{2N_t \times 2}$. The N_tN_r-dimensional vector observation is then

$$\begin{aligned} \boldsymbol{y}[k] &= \begin{bmatrix} \boldsymbol{h} & & \\ & \ddots & \\ & & \boldsymbol{h} \end{bmatrix} \boldsymbol{\delta}[k] + \boldsymbol{v}[k] \\ &= \boldsymbol{H}\boldsymbol{\delta}[k] + \boldsymbol{v}[k] \end{aligned} \tag{3.10}$$

with $\boldsymbol{h}$ defined in (3.6), $\boldsymbol{H} \in \mathbb{R}^{N_tN_r \times 2N_tN_r}$, and

$$\boldsymbol{v}[k] := \begin{bmatrix} v^{(1,1)}[k] \\ \vdots \\ v^{(N_t,N_r)}[k] \end{bmatrix} \in \mathbb{R}^{N_tN_r}$$

denoting the i.i.d. measurement noise with $\boldsymbol{v}[k] \overset{\text{i.i.d.}}{\sim} \mathcal{N}(0, \boldsymbol{R})$ and $\boldsymbol{R} = r\boldsymbol{I}_{N_tN_r}$.

3.2.4 Model Properties

This section analyzes qualitative properties of the state variable realization (SVR) specified in (3.7) and (3.10) as these properties are critical to the behavior and performance of state tracking as well as the existence and uniqueness of steady-state prediction covariances as analyzed in Section 3.4.

Two key properties in analyzing the behavior of the steady state Kalman Fil-

ter are controllability and stabilizability. We first define the notion of complete controllability below.

Definition 1. *A discrete-time system is completely controllable if, given an arbitrary destination point in the state space, there is an input sequence that will bring the system from any initial state to this point in a finite number of steps [10].*

The concept of stabilizability is closely related to controllability. Recall that an unstable mode of a linear time-invariant discrete-time system is an eigenvector associated with an eigenvalue of the state transition matrix $\boldsymbol{F}$ with magnitude greater than or equal to one. Stabilizability is defined below.

Definition 2. *A system is stabilizable if all its unstable modes are controllable [7].*

Since all modes of the SVR specified in (3.7) and (3.10) are unstable, such an SVR is stabilizable if and only if it is completely controllable.

Denote $\boldsymbol{U} = \mathrm{E}[\boldsymbol{u}[k]\boldsymbol{u}^\top[k]]$ and the Cholesky factorization of $\boldsymbol{U}$ as $\boldsymbol{U}^{1/2}$ such that $\boldsymbol{U}^{1/2}(\boldsymbol{U}^{1/2})^\top = \boldsymbol{U}$. A common test for complete controllability [10] is to compute the rank of the "controllability matrix" of the pair $[\boldsymbol{F}, \boldsymbol{G}\boldsymbol{U}^{1/2}]$, i.e.,

$$\mathcal{C} = \begin{bmatrix} \boldsymbol{G}\boldsymbol{U}^{1/2} & \boldsymbol{F}\boldsymbol{G}\boldsymbol{U}^{1/2} & \cdots & \boldsymbol{F}^{2N_tN_r-1}\boldsymbol{G}\boldsymbol{U}^{1/2} \end{bmatrix} \tag{3.11}$$

where $\mathcal{C} \in \mathbb{R}^{2N_tN_r \times (2N_tN_r(2(N_t+N_r))}$. The SVR specified in (3.7) and (3.10) is completely controllable if and only if $\mathrm{rank}(\mathcal{C}) = 2N_tN_r$.

It can be shown that the rank of $\boldsymbol{G}\boldsymbol{U}^{1/2}$ is $2(N_t + N_r - 1)$. Intuitively, this is a consequence of the fact that, while the number of states in the unified dynamic model grows according to the product N_tN_r, the number of independent oscillators grows according to the sum $N_t + N_r$. In fact $2(N_tN_r - N_t - N_r + 1)$ state elements can be determined from $2(N_t+N_r-1)$ state elements, to up to unknown, but deterministic,

bias terms, representing differences of the channel phases $\psi^{(n,m)}$. This causes the process noise $\boldsymbol{Gu}[k]$ to span only a subspace of the $2N_tN_r$-dimensional state space. Hence, $\text{rank}(\mathcal{C}) \leq 2(N_t + N_r - 1) \leq 2N_tN_r$ where the second inequality is strict if $N_t > 1$ and $N_r > 1$. In other words, the SVR specified in (3.7) and (3.10) is not stabilizable unless $N_t = 1$ or $N_r = 1$. As discussed in Section 3.3, this lack of stabilizability results in additional conditions that must be satisfied for a Kalman filter tracker to be asymptotically stable.

We now consider the observability of the SVR specified in (3.7) and (3.10).

Definition 3. *A system is completely observable if its initial state can be fully and uniquely recovered from a finite number of observations of its output (in the absence of noise) and knowledge of its input [10].*

A common test to check complete observability for linear time-invariant systems is to compute the rank of the "observability matrix" of the pair $[\boldsymbol{F}, \boldsymbol{H}]$, given as

$$\mathcal{O} = \begin{bmatrix} \boldsymbol{H} \\ \boldsymbol{HF} \\ \vdots \\ \boldsymbol{HF}^{2N_tN_r-1} \end{bmatrix} \tag{3.12}$$

where $\mathcal{O} \in \mathbb{R}^{(N_tN_r(2N_tN_r))\times 2N_tN_r}$. The system is completely observable if and only if $\text{rank}(\mathcal{O}) = 2N_tN_r$. The following lemma establishes that the SVR specified in (3.7) and (3.10) is completely observable, an important property that will be used in several later results.

Lemma 1. *Given $T_0 > 0$, $[\boldsymbol{H}, \boldsymbol{F}]$ as specified in (3.7) and (3.10) is completely observable.*

Proof. Observe that $\boldsymbol{H} = \boldsymbol{I}_{N_r N_t} \otimes \boldsymbol{h}$ and $\boldsymbol{F}^k = \boldsymbol{I}_{N_r N_t} \otimes \boldsymbol{f}^k$ with

$$\boldsymbol{f}^k = \begin{bmatrix} 1 & kT_0 \\ 0 & 1 \end{bmatrix}.$$

Since $\boldsymbol{h}\boldsymbol{f}^k = [1, kT_0]$, we can write

$$\boldsymbol{H}\boldsymbol{F}^k = \boldsymbol{I}_{N_r N_t} \otimes \boldsymbol{h}\boldsymbol{f}^k \in \mathbb{R}^{N_t N_r \times 2N_t N_r}.$$

It is straightforward to see that the observability matrix in (3.12) has row rank $2N_t N_r$ for any $T_0 > 0$ since the square matrix

$$\mathcal{O}' = \begin{bmatrix} \boldsymbol{H} \\ \boldsymbol{H}\boldsymbol{F} \end{bmatrix} \in \mathbb{R}^{2N_t N_r \times 2N_t N_r}$$

is full rank when $T_0 > 0$. Hence $[\boldsymbol{H}, \boldsymbol{F}]$ as specified in (3.7) and (3.10) is completely observable. □

A condition necessary for the Kalman Filter to converge to a well-defined steady-state solution is that the SVR in (3.7) and (3.10) is detectable. We conclude this section by defining detectability below.

Definition 4. *A system is detectable if all its unstable modes are observable [7].*

Since complete observability suffices for detectability, the SVR specified in (3.7) and (3.10) is indeed detectable.

3.3 Optimal Channel Estimation and Tracking

It is straightforward to see that the dynamic model and observations specified in (3.7) and (3.10) comprise a standard linear time-invariant (LTI) Gauss-Markov

model with zero-mean temporally i.i.d. Gaussian mutually independent process and measurement noises with process noise covariance $\boldsymbol{Q}$ and measurement noise covariance $\boldsymbol{R}$. Further assuming an independent Gaussian initial state $\boldsymbol{\delta}[0]$, it follows that a standard Kalman filter [7] can be used to generate optimal (both minimum variance and maximum likelihood) estimates and one-step predictions of the unified pairwise offset state $\boldsymbol{\delta}[k]$.

3.3.1 Asymptotic Stability of the Kalman Filter

We denote $\hat{\boldsymbol{\delta}}[k \,|\, \ell]$ as the MMSE estimate of the state $\boldsymbol{\delta}[k]$ given observations $\{y[0], \ldots, y[\ell]\}$ and $\tilde{\boldsymbol{\delta}}[k \,|\, \ell] = \hat{\boldsymbol{\delta}}[k \,|\, \ell] - \boldsymbol{\delta}[k]$ as the estimation error. As part of the Kalman filter recursion, the (one-step) prediction covariance at time k, defined as

$$\boldsymbol{P}[k] := \mathrm{E}\left\{\tilde{\boldsymbol{\delta}}[k \,|\, k-1](\tilde{\boldsymbol{\delta}}[k \,|\, k-1])^\top\right\} \in \mathbb{R}^{2N_tN_r \times 2N_tN_r}$$

is updated via the Riccati difference equation

$$\boldsymbol{P}[k+1] \;=\; \boldsymbol{F}\boldsymbol{P}[k]F^\top - \boldsymbol{F}\boldsymbol{P}[k]\boldsymbol{H}^\top(\boldsymbol{H}\boldsymbol{P}[k]\boldsymbol{H}^\top + \boldsymbol{R})^{-1}\boldsymbol{H}\boldsymbol{P}[k]\boldsymbol{F}^\top + \boldsymbol{Q} \quad (3.13)$$

given an initial prediction covariance $\boldsymbol{P}[0]$.

Although the system specified in (3.7) and (3.10) is not stabilizable, the following theorem (adapted from [6, Theorem 4.1]) establishes conditions sufficient for the Kalman filter to be asymptotically stable.

Theorem 2. *If $\boldsymbol{F}$, $\boldsymbol{F}^{-1}$, $\boldsymbol{Q}$, and $\boldsymbol{R}^{-1}$ are all bounded, $[\boldsymbol{H}\boldsymbol{R}^{-1/2}, \boldsymbol{F}]$ is completely observable, and*

$$\boldsymbol{W}[k] = \boldsymbol{F}^k\boldsymbol{P}[0](\boldsymbol{F}^k)^\top + \sum_{\ell=1}^{k}\boldsymbol{F}^{k-\ell}\boldsymbol{Q}(\boldsymbol{F}^{k-\ell})^\top$$

is nonsingular for some k where $\boldsymbol{P}[0]$ is the initial prediction covariance, then the Kalman filter is asymptotically stable.

The boundedness conditions are satisfied for the system specified in (3.7) and (3.10) under the usual assumptions that $r > 0$, $T_0 < \infty$, and the oscillator parameters are finite. Lemma 1 establishes complete observability. The final condition, $\boldsymbol{W}[k]$ is non-singular for some k, can be thought of as an interaction between the initial prediction covariance $\boldsymbol{P}[0]$ and the controllability Gramian. The singularity of the summation in the expression for $\boldsymbol{W}[k]$ represents a lack of reachability of $[\boldsymbol{F}, \boldsymbol{Q}^{1/2}]$. Suppose $\boldsymbol{W}[k]$ is singular for all k and consider its nontrivial null space. Then this null space represents a linear combination of states that are perfectly known at $k = 0$, and are not affected by the process noise. Thus the Kalman filter does not update these modes. Should they be on or outside the unit circle, then the resulting filter cannot be stable. Observe that it is sufficient (but not necessary) to select $\boldsymbol{P}[0]$ to be any positive definite matrix to satisfy the condition given in the theorem for the system specified in (3.7) and (3.10).

The prediction covariance is particularly important for distributed coherent transmission systems since the achievable performance of distributed beamforming and nullforming is a direct function of the phase prediction variance [33, 63]. The phase prediction variances correspond to the $(i, i)^{\text{th}}$ elements of $\boldsymbol{P}[k]$ for odd values of i.

3.3.2 Unified Tracking Example

As an example of typical tracking behavior, we demonstrate a Kalman filter tracker for the unified model specified in (3.7) and (3.10) for a system with $N_t = 20$ transmitters and $N_r = 10$ receivers. The state update interval was set to $T_0 = 0.250$ seconds and the carrier frequency was set to $\omega_c = 2\pi \cdot 900 \cdot 10^6$ radians/sec. All oscillators were assumed to have the same process noise parameters with $\alpha_t^{(n)} = \alpha_r^{(m)} =$

2.31×10^{-21} seconds and $\beta_t^{(n)} = \beta_r^{(m)} = 6.80 \times 10^{-23}$ Hertz for all n and m according to the Rakon RPFO45 oven-controlled oscillator parameters as discussed in Section 3.2.1. The measurement noise variance was set to $r = (2\pi \cdot 10/360)^2$ rad^2.

Figure 3.3 plots the (1,1) and (2,2) elements of the prediction covariance matrix $\boldsymbol{P}[k]$, corresponding to the phase prediction variance and frequency prediction variance, respectively, versus the experimentally determined prediction variances obtained via Monte-Carlo simulation of the Kalman filter over 500 independent realizations of the initial states, process noises, and measurement noises. This example shows that the actual prediction variances of the Kalman filter agree with the corresponding elements of the prediction covariance matrix $\boldsymbol{P}[k]$ and that the prediction variances converge toward steady-state values. These values were obtained by solving a discrete-time algebraic Riccati equation. The following section formalizes the existence of the steady-state prediction covariance in the unified dynamic model and develops closed-form expressions for the asymptotic prediction covariance as $N_t \to \infty$ with $N_r = \eta N_t$.

3.3.3 Example Tracking and Feedback Implementation Strategies

In the context of coherent distributed MIMO communication systems, the purpose of channel tracking is to produce optimal channel predictions and to facilitate computation of precoding vectors for coherent distributed communication techniques, e.g., distributed beamforming and/or distributed nullforming. In the absence of channel reciprocity, some form of feedback from the receive nodes to the transmit nodes is required to facilitate coherent transmission. There are several ways in which the tracking system and feedback can be implemented. This section discusses two possible implementation strategies and their tradeoffs.

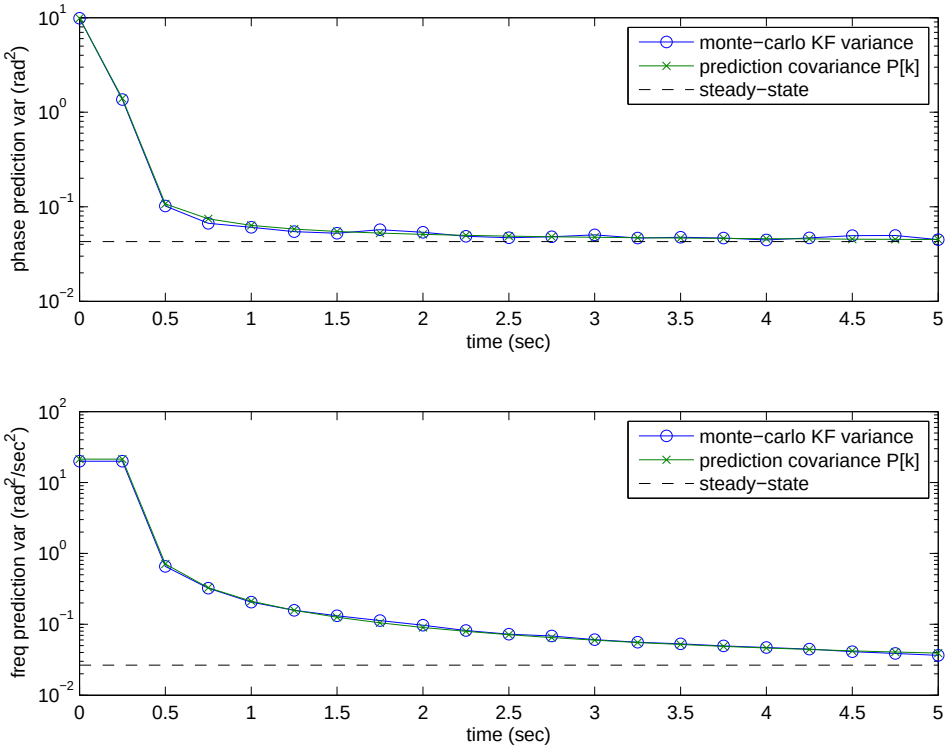

Figure 3.3: Phase and frequency prediction variances for a Kalman filter tracker of the unified state-space model with $N_t = 20$, $N_r = 10$, and $T_0 = 0.250$.

One possible implementation strategy is for the tracking and precoding vector calculations to be performed by a designated master receive node and for this receive node to feed back one or more precoding vectors to the transmit nodes. By exchanging messages among the receive nodes, the master receive node receives channel measurements from the other receive nodes, forms a complete copy of the observation vector $\boldsymbol{y}[k]$ containing all $N_t N_r$ noisy channel phase measurements, generates channel predictions, computes the desired precoding vectors, and provides these precoding vectors to the transmit nodes via the feedback channel.

A second possible implementation strategy is for the receivers to feed back their observations and for one or more transmitters to perform the tracking. Since the observations at the receivers are broadcast back to the transmitters, each transmitter in the system will receive a complete copy of the observation vector $\boldsymbol{y}[k]$ containing all $N_t N_r$ noisy channel phase measurements. Each transmitter can then track the unified state $\boldsymbol{\delta}[k]$, generate channel predictions, and compute precoding vectors individually without any additional information exchange between the transmitters. Alternatively, to avoid redundant computation, a master transmitter could be selected to perform the tracking and distribute precoding vector coefficients to the slave transmitters.

The first strategy has lower feedback requirements but requires centralized processing by a designated master receive node. The second strategy can be implemented without any messaging among the receive nodes or among the transmit nodes but has higher feedback requirements. While other implementation strategies are also possible, the particular choice of implementation strategy depends on the constraints and desired tradeoffs of the specific application. The analysis and numerical results in this paper do not depended on the particular tracking and feedback implementation strategy.

3.3.4 A Remark on Phase Unwrapping

While we have assumed the observations in (3.10) to be unwrapped phase measurements, it is usually the case in practical systems that only wrapped phase measurements are available. Additional considerations are often necessary in this case to avoid phase aliasing, incorrect phase unwrapping, and poor tracking performance.

The problem of tracking phases and frequencies in systems with wrapped phase measurements is well-known and results in an integer ambiguity in the noisy phase observations [10]. Several solutions have been proposed to work around this ambiguity, e.g., [55, 65, 118, 128]. In practice, the effect of wrapped phase measurements is negligible if the standard deviation of the Kalman filter phase prediction error is small with respect to π. Since this is typically not be the case during startup, one possible solution is to obtain accurate phase and frequency estimates [106] prior to tracking and to initialize the Kalman filter with predictions from these estimates. During steady-state operation, this also sets an upper limit on the observation interval T_0 since the steady-state phase prediction variance is an increasing function of T_0.

3.4 Steady-State Prediction Covariance Analysis

In this section, we analyze the steady-state behavior of a Kalman filter tracker for the unified state $\boldsymbol{\delta}[k]$. It is known that $[\boldsymbol{H}, \boldsymbol{F}]$ completely observable is sufficient for (3.13) to converge to a finite symmetric positive semidefinite steady-state covariance as $k \to \infty$ [10]. This steady-state covariance is not necessarily unique, however, and may depend on the initial covariance $\boldsymbol{P}[0]$. If, in addition, the system is such that $[\boldsymbol{F}, \boldsymbol{G}\boldsymbol{U}^{1/2}]$ is completely controllable, it is known that the steady-state prediction covariance is unique and positive definite. As discussed in Section 3.2.4, the sys-

tem specified in (3.7) and (3.10) does not satisfy this condition due to its lack of stabilizability.

In this section, we analyze the steady-state prediction covariance of the system specified in (3.7) and (3.10) assuming that the initial prediction covariance $\boldsymbol{P}[0]$ is selected such that (3.13) converges to a *strong solution*. From [24], a real symmetric positive semidefinite solution of the discrete-time algebraic Riccati equation (DARE)

$$\boldsymbol{P} = \boldsymbol{F}\boldsymbol{P}\boldsymbol{F}^\top - \boldsymbol{F}\boldsymbol{P}\boldsymbol{H}^\top(\boldsymbol{H}\boldsymbol{P}\boldsymbol{H}^\top + \boldsymbol{R})^{-1}\boldsymbol{H}\boldsymbol{P}\boldsymbol{F}^\top + \boldsymbol{Q}. \tag{3.14}$$

is said to be a *strong solution* if the corresponding filter state transition matrix

$$\boldsymbol{E} := \boldsymbol{F} - \boldsymbol{F}\boldsymbol{P}\boldsymbol{H}^\top(\boldsymbol{H}\boldsymbol{P}\boldsymbol{H} + \boldsymbol{R})^{-1}\boldsymbol{H} \tag{3.15}$$

has all of its eigenvalues inside or on the unit circle. Note that a strong solution is not necessarily a stabilizing solution since a stabilizing solution requires all of the eigenvalues of $\boldsymbol{E}$ to be strictly inside the unit circle. As shown in [24, Theorem 3.1], detectability is sufficient to establish the existence and uniqueness of a strong solution. The following theorem [24, Theorem 4.3] further establishes that observability along with an appropriately chosen initial prediction covariance $\boldsymbol{P}[0]$ is sufficient to ensure that (3.13) converges to the unique strong solution of (3.14).

Theorem 3. *Subject to* $[\boldsymbol{H}, \boldsymbol{F}]$ *observable and* $(\boldsymbol{P}[0] - \boldsymbol{P}) > 0$ *or* $\boldsymbol{P}[0] = \boldsymbol{P}$*, then*

$$\lim_{k\to\infty} \boldsymbol{P}[k] = \boldsymbol{P}$$

where $\boldsymbol{P}[k]$ *follows (3.13) with initial condition* $\boldsymbol{P}[0]$ *and where* $\boldsymbol{P}$ *is the unique positive semidefinite strong solution of (3.14).*

From a practical standpoint, we are interested characterizing the unique strong

solution to (3.14) since any other solution to (3.14) will result in a filter state transition matrix with poles outside of the unit circle. Hence, we will assume hereafter that the initial prediction covariance is selected so that the conditions of Theorem 3 are satisfied. One difficulty in calculating the strong solution is that the strong solution $\boldsymbol{P}$ is not positive definite since the system specified in (3.7) and (3.10) has one or more uncontrollable modes on the unit circle. This precludes direct calculation with standard numerical solvers such as MATLAB's `dare` function. To overcome this difficulty, the following section describes a procedure for computing the strong solution to (3.14) for the system specified in (3.7) and (3.10) that has the additional benefit of reducing the dimension of the associated discrete-time algebraic Riccati equation.

3.4.1 Computing the Unique Strong Solution

Since $[\boldsymbol{F}, \boldsymbol{G}\boldsymbol{U}^{1/2}]$ is not stabilizable, there exists $\boldsymbol{T}$ such that

$$\boldsymbol{A} = \boldsymbol{T}\boldsymbol{F}\boldsymbol{T}^{-1},\ \boldsymbol{B} = \boldsymbol{T}\boldsymbol{G}\boldsymbol{U}^{1/2},\ \boldsymbol{C} = \boldsymbol{H}\boldsymbol{T}^{-1} \tag{3.16}$$

with

$$\boldsymbol{A} = \begin{bmatrix} \boldsymbol{A}_1 & \boldsymbol{A}_2 \\ \boldsymbol{0} & \boldsymbol{A}_3 \end{bmatrix}, \boldsymbol{B} = \begin{bmatrix} \boldsymbol{B}_1 \\ \boldsymbol{0} \end{bmatrix}, \boldsymbol{C} = \begin{bmatrix} \boldsymbol{C}_1 & \boldsymbol{C}_2 \end{bmatrix} \tag{3.17}$$

such that $[\boldsymbol{A}_1, \boldsymbol{B}_1]$ is completely controllable. Such a decomposition is known as a Kalman decomposition [25, pp.159-163] and can also be used to separate observable and unobservable states. For the system specified by (3.7) and (3.10), we have $\boldsymbol{A}_1 \in \mathbb{R}^{2(N_t+N_r-1)\times 2(N_t+N_r-1)}$. The following theorem establishes that the unique strong solution to (3.14) can be found through solving a reduced dimensional DARE for $\{\boldsymbol{A}_1, \boldsymbol{B}_1, \boldsymbol{C}_1, \boldsymbol{R}\}$.

Theorem 4. *The unique strong solution to (3.14) is*

$$\boldsymbol{P} = \boldsymbol{T}^{-1}\bar{\boldsymbol{\Pi}}\boldsymbol{T}^{-\top}$$

with T defined in (3.16) and with positive semidefinite $\bar{\boldsymbol{\Pi}} \in \mathbb{R}^{2N_tN_r \times 2N_tN_r}$ defined as

$$\bar{\boldsymbol{\Pi}} := \begin{bmatrix} \boldsymbol{\Pi} & \mathbf{0} \\ \mathbf{0} & \mathbf{0} \end{bmatrix} \tag{3.18}$$

with $\boldsymbol{\Pi} \in \mathbb{R}^{2(N_t+N_r-1)\times 2(N_t+N_r-1)}$ the unique positive definite solution to

$$\boldsymbol{\Pi} = \boldsymbol{A}_1\Big(\boldsymbol{\Pi} - \boldsymbol{\Pi}\boldsymbol{C}_1^\top\left(\boldsymbol{C}_1\boldsymbol{\Pi}\boldsymbol{C}_1^\top + \boldsymbol{R}\right)^{-1}\boldsymbol{C}_1\boldsymbol{\Pi}\Big)\boldsymbol{A}_1^\top + \boldsymbol{B}_1\boldsymbol{B}_1^\top. \tag{3.19}$$

A proof of this theorem is provided in Appendix A.1. While this result was developed here in the context of the unified dynamic model as specified in (3.7) and (3.10), it is worth pointing out this result is general in that it only requires $[\boldsymbol{H}, \boldsymbol{F}]$ completely observable and the eigenvalues of $\boldsymbol{F}$ to be on or inside the unit circle. One consequence of this result is that the resulting discrete-time algebraic Riccati equation for $\boldsymbol{\Pi}$ is of dimension $2(N_t + N_r - 1) \times 2(N_t + N_r - 1)$, which is considerably smaller than the dimensions of $\boldsymbol{P} \in \mathbb{R}^{2N_tN_r \times 2N_tN_r}$ when N_t and/or N_r is large. Nevertheless, it can still be computationally difficult to solve (3.14) for large N_t and/or large N_r since the dimensions of the similarity transform in (3.16) become large and the dimensions of the resulting reduced-dimensional DARE in (3.19) still grow without bound as $N_t \to \infty$ and/or $N_r \to \infty$. In the particular case when the oscillator parameters are identical for all of the nodes in the system, the repetitive structure of the system matrices allows for an even more efficient solution of (3.14), as discussed in the following section.

3.4.2 Strong Solution with i.i.d. Process and Measurement Noise

In this section we assume that the transmit and receive nodes have identical and independent process noise statistics with $\boldsymbol{Q}_t^{(n)} = \boldsymbol{Q}_r^{(m)} = \boldsymbol{q} \in \mathbb{R}^{2\times 2}$. In this case, we have $\mathrm{E}\left[\boldsymbol{u}[k]\boldsymbol{u}^\top[k]\right] = \boldsymbol{U} = \boldsymbol{I}_{N_t+N_r} \otimes \boldsymbol{q}$ and process noise covariance can be written as

$$
\begin{aligned}
\boldsymbol{Q} &= \boldsymbol{G}\mathrm{E}\left[\boldsymbol{u}[k]\boldsymbol{u}^\top[k]\right]\boldsymbol{G}^\top \\
&= \left[\begin{array}{ccc|ccc|c}
2\boldsymbol{q} & \boldsymbol{q} & \cdots & \boldsymbol{q} & \boldsymbol{0} & & \\
\boldsymbol{q} & 2\boldsymbol{q} & \cdots & \boldsymbol{0} & \boldsymbol{q} & & \cdots \\
\vdots & \vdots & \ddots & & & \ddots & \\
\hline
\boldsymbol{q} & \boldsymbol{0} & & 2\boldsymbol{q} & \boldsymbol{q} & \cdots & \\
\boldsymbol{0} & \boldsymbol{q} & & \boldsymbol{q} & 2\boldsymbol{q} & \cdots & \cdots \\
& & \ddots & \vdots & \vdots & \ddots & \\
\hline
& \vdots & & & \vdots & & \ddots \\
& & & & & &
\end{array}\right] \\
&= \boldsymbol{I}_{N_r} \otimes \boldsymbol{Q}_0 + \boldsymbol{1}_{N_r}\boldsymbol{1}_{N_r}^\top \otimes \boldsymbol{Q}_1 \\
&= \boldsymbol{\Gamma}_{N_r}(\boldsymbol{Q}_0, \boldsymbol{Q}_1)
\end{aligned}
\tag{3.20}
$$

with $\boldsymbol{Q}_0 = \mathbf{1}_{N_t}\mathbf{1}_{N_t}^\top \otimes \boldsymbol{q}$ and $\boldsymbol{Q}_1 = \boldsymbol{I}_{N_t} \otimes \boldsymbol{q}$ and where the final equality uses the $\boldsymbol{\Gamma}$-notation established as follows

$$\begin{aligned}\boldsymbol{\Gamma}_n(\boldsymbol{A},\boldsymbol{B}) &:= \boldsymbol{I}_n \otimes \boldsymbol{A} + \mathbf{1}_n\mathbf{1}_n^\top \otimes \boldsymbol{B} \\ &= \begin{bmatrix} \boldsymbol{A}+\boldsymbol{B} & \boldsymbol{B} & \cdots & \boldsymbol{B} \\ \boldsymbol{B} & \boldsymbol{A}+\boldsymbol{B} & & \\ \vdots & & \ddots & \\ \boldsymbol{B} & & & \boldsymbol{A}+\boldsymbol{B} \end{bmatrix}. \end{aligned} \tag{3.21}$$

If the measurement noise covariance also satisfies $\boldsymbol{R} = r\boldsymbol{I}_{N_tN_r}$, it is straightforward to see that every matrix $\{\boldsymbol{F},\boldsymbol{H},\boldsymbol{R},\boldsymbol{Q}\}$ in the system as specified in (3.7) and (3.10) can be written in this $\boldsymbol{\Gamma}$-notation. The following Theorem establishes that, when $\{\boldsymbol{F},\boldsymbol{H},\boldsymbol{R},\boldsymbol{Q}\}$ can be expressed in this form (subject to observability), (3.14) can be efficiently solved by solving only two smaller DAREs.

Theorem 5. *Given* $[\boldsymbol{H},\boldsymbol{F}]$ *is completely observable and*

$$\begin{aligned}\boldsymbol{F} &= \boldsymbol{\Gamma}_n(\boldsymbol{F}_0,\boldsymbol{F}_1) \text{ with } \boldsymbol{F}_0 \in \mathbb{R}^{s\times s} \text{ and } \boldsymbol{F}_1 \in \mathbb{R}^{s\times s}, \\ \boldsymbol{H} &= \boldsymbol{\Gamma}_n(\boldsymbol{H}_0,\boldsymbol{H}_1) \text{ with } \boldsymbol{H}_0 \in \mathbb{R}^{t\times s} \text{ and } \boldsymbol{H}_1 \in \mathbb{R}^{t\times s}, \\ \boldsymbol{R} &= \boldsymbol{\Gamma}_n(\boldsymbol{R}_0,\boldsymbol{R}_1) \text{ with } \boldsymbol{R}_0 \in \mathbb{R}^{t\times t} \text{ and } \boldsymbol{R}_1 \in \mathbb{R}^{t\times t}, \text{ and} \\ \boldsymbol{Q} &= \boldsymbol{\Gamma}_n(\boldsymbol{Q}_0,\boldsymbol{Q}_1) \text{ with } \boldsymbol{Q}_0 \in \mathbb{R}^{s\times s} \text{ and } \boldsymbol{Q}_1 \in \mathbb{R}^{s\times s}\end{aligned}$$

then the unique strong solution to (3.14) is given as $\boldsymbol{P} = \boldsymbol{\Gamma}_n(\boldsymbol{P}_0,\boldsymbol{P}_1)$ *with* $\boldsymbol{P}_0 \in \mathbb{R}^{s\times s}$ *the unique strong solution of*

$$\boldsymbol{P}_0 = \boldsymbol{F}_0\Big[\boldsymbol{P}_0 - \boldsymbol{P}_0\boldsymbol{H}_0^\top(\boldsymbol{H}_0\boldsymbol{P}_0\boldsymbol{H}_0^\top + \boldsymbol{R}_0)^{-1}\boldsymbol{H}_0\boldsymbol{P}_0\Big]\boldsymbol{F}_0^\top + \boldsymbol{Q}_0$$

and $\bar{\boldsymbol{P}} = \boldsymbol{P}_0 + n\boldsymbol{P}_1 \in \mathbb{R}^{s\times s}$ *the unique strong solution of*

$$\bar{\boldsymbol{P}} = \bar{\boldsymbol{F}}\left[\bar{\boldsymbol{P}} - \bar{\boldsymbol{P}}\bar{\boldsymbol{H}}^\top(\bar{\boldsymbol{H}}\bar{\boldsymbol{P}}\bar{\boldsymbol{H}}^\top + \bar{\boldsymbol{R}})^{-1}\bar{\boldsymbol{H}}\bar{\boldsymbol{P}}\right]\bar{\boldsymbol{F}}^\top + \bar{\boldsymbol{Q}} \tag{3.22}$$

with $\bar{\boldsymbol{F}} := \boldsymbol{F}_0 + n\boldsymbol{F}_1$, $\bar{\boldsymbol{H}} := \boldsymbol{H}_0 + n\boldsymbol{H}_1$, $\bar{\boldsymbol{R}} := \boldsymbol{R}_0 + n\boldsymbol{R}_1$, *and* $\bar{\boldsymbol{Q}} := \boldsymbol{Q}_0 + n\boldsymbol{Q}_1$.

A proof of Theorem 5 is provided in Appendix A.2. Observe that the system specified in (3.7) and (3.10) satisfies the requirements of Theorem 5 with $n = N_r$. The utility of this theorem is that the $2N_tN_r \times 2N_tN_r$ DARE in (3.14) can be solved by computing two smaller $2N_t \times 2N_t$ DAREs, each of which is of lower dimension than the method described in Section 3.4.1. While the dimension of these smaller DAREs also grows without bound as $N_t \to \infty$, it turns out that we can further simplify the solution of (3.14) by observing that the system specified in (3.7) and (3.10) has the additional structure

$$\begin{aligned}
\boldsymbol{F}_0 &= \boldsymbol{\Gamma}_{N_t}(\boldsymbol{f}, \boldsymbol{0}) \\
\boldsymbol{H}_0 &= \boldsymbol{\Gamma}_{N_t}(\boldsymbol{h}, \boldsymbol{0}) \\
\boldsymbol{R}_0 &= \boldsymbol{\Gamma}_{N_t}(\boldsymbol{r}, \boldsymbol{0}) \\
\boldsymbol{Q}_0 &= \boldsymbol{\Gamma}_{N_t}(\boldsymbol{0}, \boldsymbol{q}) \\
\boldsymbol{Q}_1 &= \boldsymbol{\Gamma}_{N_t}(\boldsymbol{q}, \boldsymbol{0})
\end{aligned}$$

with $\boldsymbol{f} \in \mathbb{R}^{2\times 2}$, $\boldsymbol{h} \in \mathbb{R}^{1\times 2}$, $r \in \mathbb{R}$, and $\boldsymbol{q} \in \mathbb{R}^{2\times 2}$ all defined in Section 3.2.3. Hence, Theorem 5 can be *recursively* applied in the context of the oscillator tracking problem to say that $\boldsymbol{P} = \boldsymbol{\Gamma}_{N_r}(\boldsymbol{P}_0, \boldsymbol{P}_1)$ with

$$\boldsymbol{P}_0 = \boldsymbol{\Gamma}_{N_t}(\boldsymbol{p}_{00}, \boldsymbol{p}_{01}) \tag{3.23}$$

$$\boldsymbol{P}_1 = \boldsymbol{\Gamma}_{N_t}(\boldsymbol{p}_{10}, \boldsymbol{p}_{11}) \tag{3.24}$$

where $\boldsymbol{p}_{00}$, $\boldsymbol{p}_{01}$, $\boldsymbol{p}_{10}$, and $\boldsymbol{p}_{11}$ are all 2×2 matrices. This result implies that, irrespective of the number of transmit and receive nodes, the $2N_tN_r \times 2N_tN_r$ prediction covariance in (3.14) can be efficiently computed for the unified oscillator tracking problem by solving four 2×2 DAREs.

We can show that one of these 2×2 DAREs is trivial to solve in our unified oscillator tracking scenario. Recursively applying Theorem 5, we can write

$$\boldsymbol{p}_{00} = \boldsymbol{f}\left[\boldsymbol{p}_{00} - \boldsymbol{p}_{00}h^{\top}\left(\boldsymbol{h}\boldsymbol{p}_{00}\boldsymbol{h}^{\top} + r\right)^{-1}\boldsymbol{h}\boldsymbol{p}_{00}\right]\boldsymbol{f}^{\top} + \mathbf{0}.$$

The unique solution to this DARE is $\boldsymbol{p}_{00} = \mathbf{0}$, which implies that $\boldsymbol{P}_0 = \boldsymbol{\Gamma}_{N_t}(\mathbf{0}, \boldsymbol{p}_{01}) = \mathbf{1}_{N_t}\mathbf{1}_{N_t}^{\top} \otimes \boldsymbol{p}_{01}$. The remaining 2×2 constituent matrices $\boldsymbol{p}_{10}$, $\boldsymbol{p}_{01}$, and $\boldsymbol{p}_{11}$ can be easily solved with numeric DARE solvers and then recombined to determine $\boldsymbol{P}_0$, $\boldsymbol{P}_1$, and $\boldsymbol{P}$.

3.5 Asymptotic Prediction Covariance Analysis

In this section, under the assumption that all nodes in the system have i.i.d. process and measurement noises, we develop closed-form expressions for the 2×2 constituent matrices $\boldsymbol{p}_{10}$, $\boldsymbol{p}_{01}$, and $\boldsymbol{p}_{11}$ defined in (3.23) and (3.24) in the asymptotic regime where $N_t \to \infty$ and $N_r = \eta N_t$. This analysis leads to simple expressions for the elements in the steady-state prediction covariance matrix $\boldsymbol{P}$ that, as shown in Section 3.6, can be good approximations of the actual steady-state prediction covariance even for modest values of N_t and N_r.

In the system defined in (3.7) and (3.10), we have $\boldsymbol{F}_1 = \mathbf{0}$, $\boldsymbol{H}_1 = \mathbf{0}$, and $\boldsymbol{R}_1 = \mathbf{0}$. We can define $\hat{\boldsymbol{P}} := N_r^{-1}\bar{\boldsymbol{P}}$ and $\hat{\boldsymbol{Q}} := N_r^{-1}\bar{\boldsymbol{Q}}$, and substitute $n = N_r$ to rewrite

(3.22) as

$$\hat{\boldsymbol{P}} = \boldsymbol{F}_0\Big[\hat{\boldsymbol{P}} - \hat{\boldsymbol{P}}\boldsymbol{H}_0^\top(\boldsymbol{H}_0\hat{\boldsymbol{P}}\boldsymbol{H}_0^\top + N_r^{-1}\boldsymbol{R}_0)^{-1}\boldsymbol{H}_0\hat{\boldsymbol{P}}\Big]\boldsymbol{F}_0^\top + \hat{\boldsymbol{Q}}. \tag{3.25}$$

As $N_r \to \infty$, we have $\hat{\boldsymbol{P}} \to \boldsymbol{P}_1$ and $\hat{\boldsymbol{Q}} \to \boldsymbol{Q}_1$. Hence, (3.25) becomes

$$\boldsymbol{P}_1 = \boldsymbol{F}_0\left[\boldsymbol{P}_1 - \boldsymbol{P}_1\boldsymbol{H}_0^\top\left(\boldsymbol{H}_0\boldsymbol{P}_1\boldsymbol{H}_0^\top\right)^{-1}\boldsymbol{H}_0\boldsymbol{P}_1\right]\boldsymbol{F}_0^\top + \boldsymbol{Q}_1.$$

Since $\boldsymbol{Q}_1 = \boldsymbol{I}_{N_t} \otimes \boldsymbol{q}$, $\boldsymbol{F}_0 = \boldsymbol{I}_{N_t} \otimes \boldsymbol{f}$, and $\boldsymbol{H}_0 = \boldsymbol{I}_{N_t} \otimes \boldsymbol{h}$ are all block diagonal matrices, it is straightforward to see that the asymptotic value of $\boldsymbol{P}_1$ is also block diagonal. In other words, $\boldsymbol{P}_1 \to \boldsymbol{I}_{N_t} \otimes \boldsymbol{p}_{10}$ and $\boldsymbol{p}_{11} \to \boldsymbol{0}$. Hence, to determine $\boldsymbol{P}_1$ for large N_r, it is only necessary to solve the 2×2 DARE

$$\boldsymbol{p}_{10} = \boldsymbol{f}\left[\boldsymbol{p}_{10} - \boldsymbol{p}_{10}\boldsymbol{h}^\top\left(\boldsymbol{h}\boldsymbol{p}_{10}\boldsymbol{h}^\top\right)^{-1}\boldsymbol{h}\boldsymbol{p}_{10}\right]\boldsymbol{f}^\top + \boldsymbol{q}. \tag{3.26}$$

Now consider $\boldsymbol{P}_0 = \boldsymbol{1}_{N_t}\boldsymbol{1}_{N_t}^\top \otimes \boldsymbol{p}_{01}$. Defining $\hat{\boldsymbol{p}}_{01} = N_t^{-1}\boldsymbol{p}_{00} + \boldsymbol{p}_{01}$, we have that $\hat{\boldsymbol{p}}_{01} = \boldsymbol{p}_{01}$ since, as shown previously, $\boldsymbol{p}_{00} = \boldsymbol{0}$ for any N_t and N_r. Theorem 5 implies that $\boldsymbol{p}_{01}$ satisfies

$$\boldsymbol{p}_{01} = \boldsymbol{f}\left[\boldsymbol{p}_{01} - \boldsymbol{p}_{01}\boldsymbol{h}^\top\left(\boldsymbol{h}\boldsymbol{p}_{01}\boldsymbol{h}^\top + N_r^{-1}r\right)^{-1}\boldsymbol{h}\boldsymbol{p}_{01}\right]\boldsymbol{f}^\top + \boldsymbol{q}$$

which, in the limit as $N_r \to \infty$, is identical in form to (3.26). Hence, in the asymptotic regime where $N_t \to \infty$ and $N_r = \eta N_t$, we have $\boldsymbol{p}_{01} = \boldsymbol{p}_{10} = \boldsymbol{p}$ with $\boldsymbol{p}$ satisfying the 2×2 DARE

$$\boldsymbol{p} = \boldsymbol{f}\left[\boldsymbol{p} - \boldsymbol{p}\boldsymbol{h}^\top\left(\boldsymbol{h}\boldsymbol{p}\boldsymbol{h}^\top\right)^{-1}\boldsymbol{h}\boldsymbol{p}\right]\boldsymbol{f}^\top + \boldsymbol{q}. \tag{3.27}$$

In other words, it is only necessary to solve a *single* 2×2 DARE to fully characterize

the $2N_tN_r \times 2N_tN_r$ asymptotic prediction covariance matrix $\boldsymbol{P}$.

Summarizing these results, we have $\boldsymbol{p}_{00} = \mathbf{0}$, $\boldsymbol{p}_{11} \to \mathbf{0}$, $\boldsymbol{p}_{01} \to \boldsymbol{p}$, and $\boldsymbol{p}_{10} \to \boldsymbol{p}$ as $N_t \to \infty$ with $N_r = \eta N_t$. Hence,

$$\boldsymbol{P}_0 \to \boldsymbol{\Gamma}_{N_t}(\mathbf{0}, \boldsymbol{p}) \tag{3.28}$$

$$\boldsymbol{P}_1 \to \boldsymbol{\Gamma}_{N_t}(\boldsymbol{p}, \mathbf{0}) \tag{3.29}$$

with $\boldsymbol{p}$ satisfying (3.27) and the asymptotic prediction covariance $\boldsymbol{P} = \boldsymbol{\Gamma}_n(\boldsymbol{P}_0, \boldsymbol{P}_1)$ taking the same form as (3.20) with $\boldsymbol{q}$ replaced by $\boldsymbol{p}$.

To compute closed-form expressions for the elements of p, we denote

$$\boldsymbol{p} = \begin{bmatrix} \boldsymbol{p}(1,1) & \boldsymbol{p}(1,2) \\ \boldsymbol{p}(2,1) & \boldsymbol{p}(2,2) \end{bmatrix}$$

and, from (3.4) under the assumption of identical process noise statistics at each receive node, set

$$\boldsymbol{q} = \omega_c^2 T_0 \begin{bmatrix} \alpha + \beta\frac{T_0^2}{3} & \beta\frac{T_0}{2} \\ \beta\frac{T_0}{2} & \beta \end{bmatrix}.$$

Some straightforward algebra on (3.27) yields

$$\boldsymbol{p}(1,2) = \boldsymbol{p}(2,1) = \omega_c^2 T_0^2 \beta \left(\gamma + \frac{1}{2}\right)$$

with $\gamma := \sqrt{\frac{1}{12} + \frac{\alpha}{T_0^2\beta}}$. The remaining elements of $\boldsymbol{p}$ follow as

$$\boldsymbol{p}(1,1) = \omega_c^2 T_0^3 \beta \left(\gamma + \frac{1}{2}\right)^2$$

$$\boldsymbol{p}(2,2) = \omega_c^2 T_0 \beta \left(\gamma + 1\right)$$

Note that the asymptotic prediction covariance is not a function of $\eta = \frac{N_r}{N_t}$ or the measurement noise variance r. The asymptotic prediction covariance is only a function of the i.i.d. process noise parameters α and β as well as the carrier frequency ω_c and the update period T_0. The parameter η only affects the rate at which the elements of the prediction covariance matrix approach their asymptotic values, as shown in Section 3.6.

3.6 Numerical Results

This section presents numerical results confirming the asymptotic analysis in Section 3.5 and also demonstrating the advantages of unified tracking in a scenario with simultaneous beamforming and nullforming. All of the results in this section assume a measurement noise standard deviation of 10 degrees, corresponding to $r = (2\pi \cdot 10/360)^2$ rad^2. Since there are only 12 unique elements in the prediction covariance matrix $\boldsymbol{P}$ irrespective of the number of transmit and receive nodes, Table 3.1 lists the 12 relevant elements of $\boldsymbol{P}$, their meanings, and their asymptotic values.

Fig. 3.4 plots elements of the prediction covariance matrix $\boldsymbol{P}$ versus the number of transmit nodes N_t with $N_r = \eta N_t$ and $\eta = 0.2$. The simulation parameters are otherwise identical to those in Section 3.3 ($T_0 = 0.250$ seconds, $\omega_c = 2\pi \cdot 900 \cdot 10^6$ radians/sec, $\alpha_t^{(n)} = \alpha_r^{(m)} = 2.31 \times 10^{-21}$ seconds, and $\beta_t^{(n)} = \beta_r^{(m)} = 6.80 \times 10^{-23}$ Hertz for all n and m). These results confirm the asymptotic analysis in Section 3.5 and show that asymptotic results can be accurate predictions of many of the elements of the prediction covariance matrix even for small values of N_t and N_r.

Fig. 3.5 repeats the results in Fig. 3.4 with $\eta = 1$. As predicted in Section 3.5,

Table 3.1: Unique elements of the prediction covariance matrix $\boldsymbol{P}$ with $n' \neq n$ and $m' \neq m$.

$\boldsymbol{P}(i,j)$	Meaning and asymptotic value
$\boldsymbol{P}(1,1)$	Phase var $\text{cov}(\phi^{(n,m)}, \phi^{(n,m)}) \to 2\boldsymbol{p}(1,1)$
$\boldsymbol{P}(1,2)$	Phase/freq cov $\text{cov}(\phi^{(n,m)}\dot{\phi}^{(n,m)}) \to 2\boldsymbol{p}(1,2)$
$\boldsymbol{P}(2,2)$	Frequency var $\text{cov}(\dot{\phi}^{(n,m)}, \dot{\phi}^{(n,m)}) \to 2\boldsymbol{p}(2,2)$
$\boldsymbol{P}(3,1)$	Phase cov $\text{cov}(\phi^{(n,m)}, \phi^{(n',m)}) \to \boldsymbol{p}(1,1)$
$\boldsymbol{P}(3,2)$	Phase/freq cov $\text{cov}(\phi^{(n,m)}\dot{\phi}^{(n',m)}) \to \boldsymbol{p}(1,2)$
$\boldsymbol{P}(4,2)$	Frequency var $\text{cov}(\dot{\phi}^{(n,m)}, \dot{\phi}^{(n',m)}) \to \boldsymbol{p}(2,2)$
$\boldsymbol{P}(2N_t+1,1)$	Phase cov $\text{cov}(\phi^{(n,m)}, \phi^{(n,m')}) \to \boldsymbol{p}(1,1)$
$\boldsymbol{P}(2N_t+1,2)$	Phase/freq cov $\text{cov}(\phi^{(n,m)}\dot{\phi}^{(n,m')}) \to \boldsymbol{p}(1,2)$
$\boldsymbol{P}(2N_t+2,2)$	Frequency var $\text{cov}(\dot{\phi}^{(n,m)}, \dot{\phi}^{(n,m')}) \to \boldsymbol{p}(2,2)$
$\boldsymbol{P}(2N_t+3,1)$	Phase cov $\text{cov}(\phi^{(n,m)}, \phi^{(n',m')}) \to 0$
$\boldsymbol{P}(2N_t+3,2)$	Phase/freq cov $\text{cov}(\phi^{(n,m)}\dot{\phi}^{(n',m')}) \to 0$
$\boldsymbol{P}(2N_t+4,2)$	Frequency var $\text{cov}(\dot{\phi}^{(n,m)}, \dot{\phi}^{(n',m')}) \to 0$

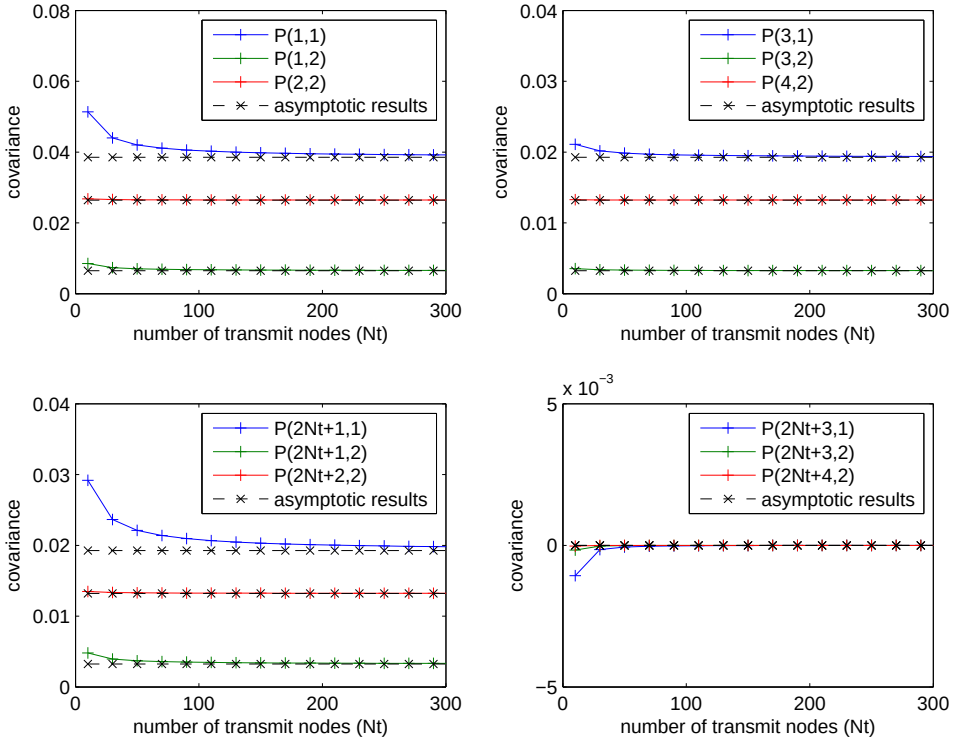

Figure 3.4: Relevant elements of the prediction covariance matrix versus the number of transmit nodes N_t with $N_r = \eta N_t$ and $\eta = 0.2$

the asymptotic results are unaffected by η. The main difference in these results with respect to those in Fig. 3.4 are that the elements of the prediction covariance matrix converge more quickly to their asymptotic values since N_r is larger for each value of N_t. Also note that the covariances $\boldsymbol{P}(2N_t+1,1)$, $\boldsymbol{P}(2N_t+1,2)$, and $\boldsymbol{P}(2N_t+2,2)$ converge at the same rate as $\boldsymbol{P}(3,1)$, $\boldsymbol{P}(3,2)$, and $\boldsymbol{P}(4,2)$ in this example. This is a consequence of the fact that $N_t = N_r$ in this system.

In both Fig. 3.4 and Fig. 3.5, observe that the steady-state phase prediction variance $P(1,1) \leq 0.06$ rad^2 in all of the cases considered. This corresponds to a phase prediction standard deviation of less than $0.08{\cdot}\pi$, implying that the probability of phase aliasing (cycle slips) from wrapped phase measurements during steady-state operation of the Kalman filter is small in these examples.

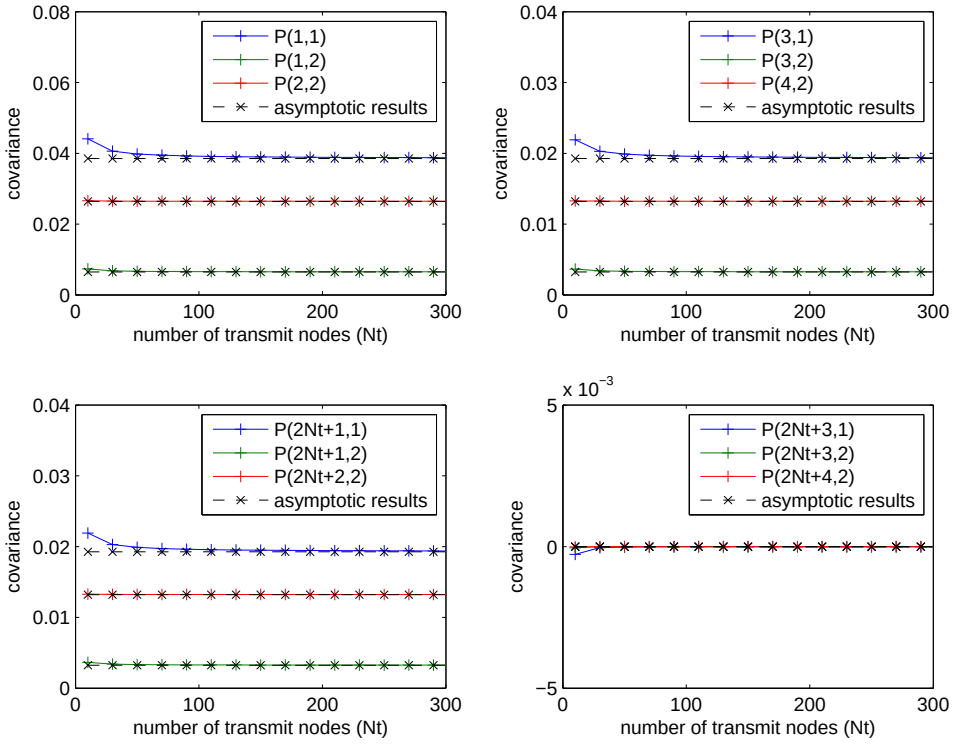

Figure 3.5: Relevant elements of the covariance matrix versus the number of transmit nodes N_t with $N_r = \eta N_t$ and $\eta = 1$

Fig. 3.6 plots the asymptotic phase standard deviation (in degrees) versus oscil-

lator parameters α and β for $T_0 = 0.250$ seconds and $\omega_c = 2\pi \cdot 900 \cdot 10^6$ radians/sec. Specifically, this plot shows $\frac{360}{2\pi} \cdot \sqrt{\boldsymbol{p}(1,1)}$ over a range of typical oscillator parameters with "good XO" and "poor XO" oscillator parameters fitted to a table of typical Allan variances from [59]. These results show that a system using the Rakon oven-controlled oscillators with $T_0 = 0.250$ seconds and $\omega_c = 2\pi \cdot 900 \cdot 10^6$ radians/sec will have an asymptotic phase prediction standard deviation of less than 10 degrees, which is more than adequate to achieve good coherent beamforming gains but may be insufficient to achieve deep nulls [33]. The "poor XO" has an asymptotic phase prediction standard deviation so large that coherent distributed transmission is impossible. To achieve coherent transmission with the "poor XO", the carrier frequency ω_c and/or the measurement interval T_0 must be reduced.

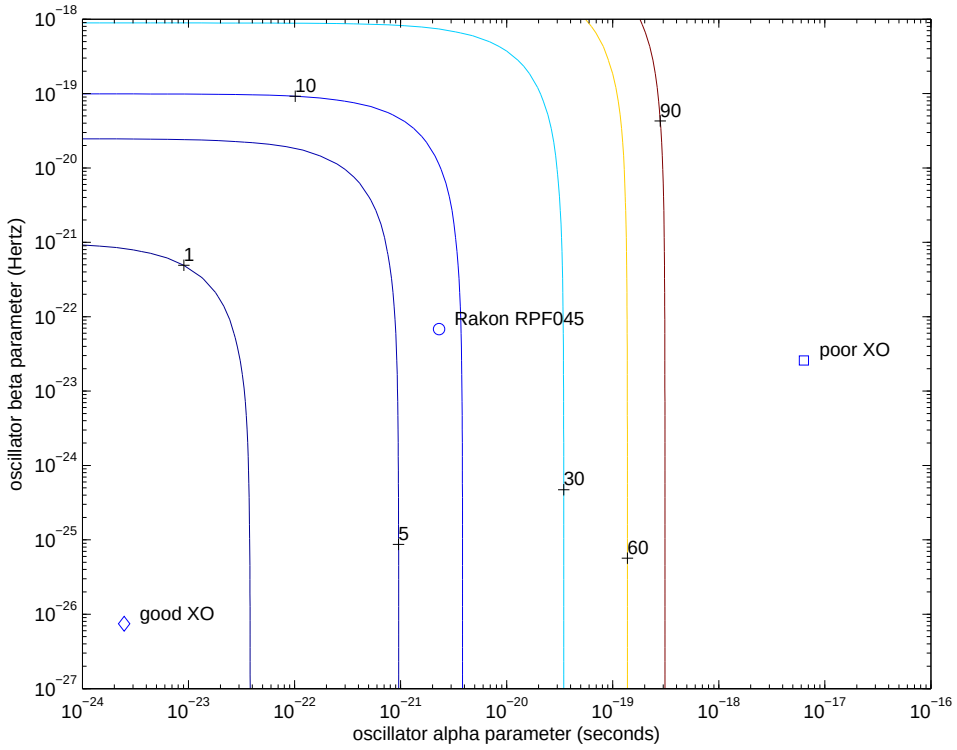

Figure 3.6: Asymptotic phase standard deviation (in degrees) versus oscillator parameters α and β for $T_0 = 0.250$ seconds and $\omega_c = 2\pi \cdot 900 \cdot 10^6$ radians/sec.

To demonstrate the performance of unified tracking in a communications set-

ting, we consider a scenario where the distributed transmit array forms forms nulls toward $N_r - 1$ "protected" receivers and uses the remaining degrees of freedom to form a beam and maximize the power at the remaining "intended" receiver. The phase predictions from the Kalman filter are used in conjunction with the known channel amplitudes to calculate a time-varying zero-forcing linear precoding vector as described in [33]. All channels are assumed to have unit magnitude and the transmit array is assumed to have a unit total power constraint.

Figure 3.7 shows the distributed beamforming and nullforming performance of a system with $N_t = 10$ transmitters, $N_r = 5$ receivers, and a measurement interval $T_0 = 250$ ms. Results are shown for "individual tracking" in which each pairwise channel is tracked in a separate two-state Kalman filter versus "unified tracking" as described in Section 3.2.3. The results were averaged over 2000 realizations of the random initial frequency offsets, clock process noises, and measurement noises. Measurements occur at $t = kT_0$ for $k = 0, 1, \ldots$.

Subfigure (a) of Fig. 3.7 shows the beamforming performance. Due to the relatively poor frequency estimates of the Kalman filters after the first measurement at $t = 0$, the beam is effectively incoherent on $0 < t < 0.25$. After the second measurement at $t = 0.25$, the Kalman filter state estimates and the resulting beam power improves and approaches the theoretical maximum $10 \log_{10} (N_t(1 - (N_r - 1)/N_t) \approx$ 7.8 dB. As t increases in the beamforming interval $0.25 < t < 0.50$, the channel predictions become increasingly stale and the resulting beamforming performance degrades slightly by the end of the beamforming interval. In this example, the beamforming performance approaches its steady-state behavior after only a few measurement intervals and the performance of individual and unified channel tracking is effectively identical.

Subfigures (b) and (c) of Fig. 3.7 show the nullforming performance with subfig-

ure (b) showing the transient behavior on $0 < t < 3$ and subfigure (c) showing the steady-state behavior on $9 < t < 12$. As with beamforming, the nulls are effectively incoherent after one measurement on the interval $0 < t < 0.25$. The null powers improve with subsequent measurements and the effect of stale channel predictions is more pronounced than with beamforming. Subfigure (c) shows that unified tracking can provide a potentially significant advantage in nullforming gain with nulls 3-4 dB deeper than with individual channel tracking in this example.

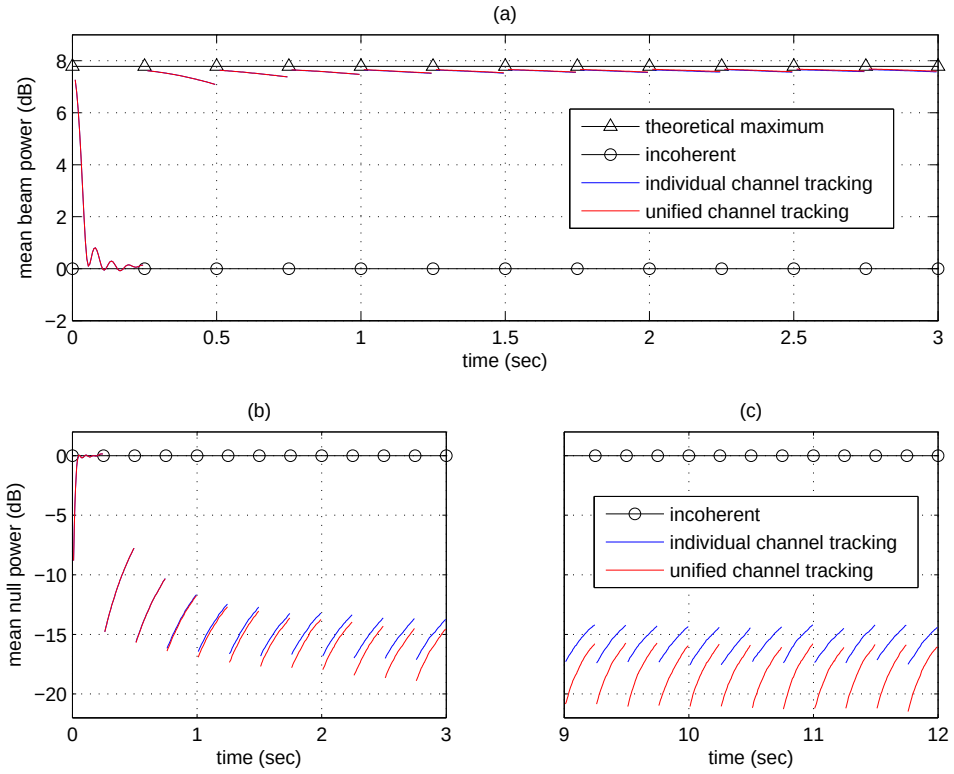

Figure 3.7: Beamforming (subfigure (a)) and nullforming (subfigures (b) and (c)) performance for a distributed MIMO system with $N_t = 10$ transmitters and $N_r = 5$ receivers. Nulls are steered toward four receivers and a beam is steered toward the fifth receiver.

3.7 Conclusions

This chapter presented a formal analysis of the stability and steady-state behavior of a Kalman filter tracker for the effective channel states in an unsynchronized distributed MIMO system. While the state-space system was shown to be nonstabilizable, the Kalman filter tracker was shown to be asymptotically stable subject to a properly chosen initial prediction covariance. A unique "strong" solution to the steady-state prediction covariance was also shown to exist and two methods were developed to efficiently solve for this unique strong solution. An asymptotic analysis was also presented for large networks with closed-from results for all of the elements in the asymptotic prediction covariance matrix. Numeric results confirmed the analysis and demonstrated the effect of the oscillator parameters on the ability of the system to achieve coherent transmission.

Chapter 4

Throughput Maximization in Wireless Powered Communication Networks with Energy Saving

This chapter considers a time division multiple access scenario where a wireless access point transmits to a group of users which harvest the energy and then use this energy to transmit back to the access point. Past approaches have found the optimal time allocation to maximize sum throughput under the assumption that the users must use all of their harvested power in each block of the "harvest-then-transmit" protocol. This chapter considers optimal time and energy allocation to maximize the sum throughput for the case when the nodes can save energy for later blocks. To maximize the sum throughput over a finite horizon, the initial optimization problem is separated into two sub-problems and finally can be formulated into a standard box-constrained optimization problem, which can be solved efficiently. A tight upper bound is derived by relaxing the energy harvesting causality. Simulation results are also provided to demonstrate the "harvest-then-transmit" protocol with

energy saving provides improved sum throughput increasing with the number of transmission blocks.

4.1 Background

Prolonging the lifetime of battery powered devices in wireless networks is an important problem [36]. Replacing or recharging batteries may be inconvenient (e.g., for a sensor network with massive distributed sensor nodes), dangerous (e.g., for devices positioned in toxic environments), or even impossible (e.g., for the medical sensors implanted inside human bodies). To overcome such situations, energy harvesting has become an attractive approach with the potential of extending the lifetime of these devices. Energy harvesting nodes have the ability to recharge their batteries from their surrounding environment by using solar, heat, vibration, or other energy sources [99, 121].

Recently, wireless power transfer (WPT) using radio frequency signals is attracting attention as a viable approach to the energy harvesting problem. One approach to WPT is to harvest energy from ambient radio signals, e.g., TV broadcast signals [73]. Another approach to WPT is to use a dedicated power transmitter such as in passive radio frequency identification (RFID) systems [38,119]. WPT systems can simultaneously convey energy and information on the wireless signals [72, 130, 151] and the inherent tradeoff between information rate and power transfer efficiency has been recently characterized [44, 149]. For the energy harvesting case, maximizing a time-average utility function over infinite time blocks (infinite horizon) is considered in [39]. In [76], the authors consider the problem of maximizing the throughput of a transmitter sending data over a time-varying channel within finite time blocks (finite horizon) under a total energy constraint. In [131], an explicit threshold policy is

derived for energy harvesting sensors to maximize the utility obtained over a finite horizon.

In this paper, we consider WPT system called a "wireless powered communication network" (WPCN). A WPCN is a network in which wireless devices are powered *only* by WPT [54]. The WPCN model considered in this paper is the same as in [54] and is shown in Fig. 4.1, where one hybrid access point (H-AP) with an effectively unlimited power supply coordinates the wireless energy/information transmissions to/from a set of distributed users. Each user is equipped with an energy storage device and thus can harvest and store the wireless energy broadcasted by the H-AP in the downlink. The users transmit their independent information using their individually harvested energy to the H-AP in the uplink. In [54], a block transmission model was considered where it was assumed that users harvest energy during a downlink transmission the first part of the block and then each user uses *all* of their harvested energy during an uplink transmission later in that block. In other words, users do not save energy for later blocks.

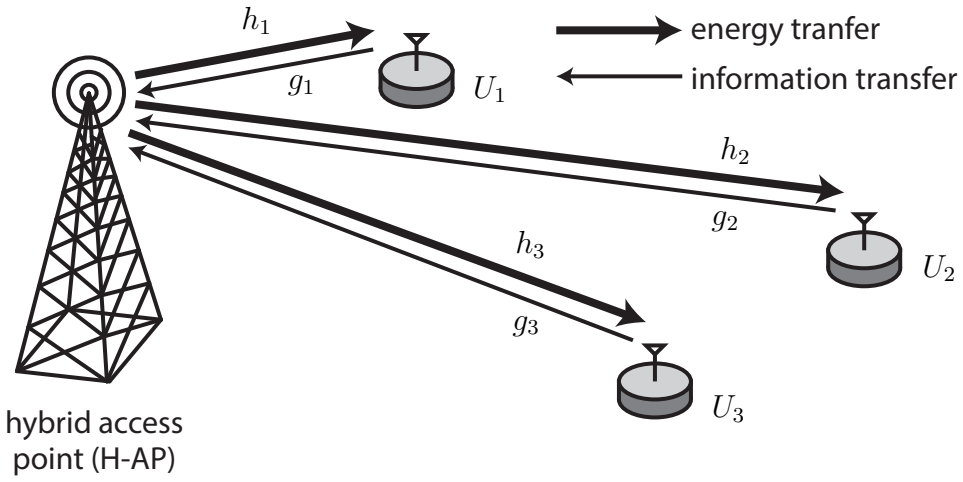

Figure 4.1: A wireless powered communication network (WPCN).

4.2 System Model

The network adopts a *harvest-then-transmit* protocol as shown in Fig.2. In each block, the first $\tau_0 T$ amount of time, with $\tau_0 \in [0, 1]$, is assigned to the downlink for the H-AP to broadcast wireless energy to all users, while the remaining time in the same block is assigned to the uplink for transmitting their independent information to the H-AP. We assume there are K users in total and the amount of time assigned to user U_i is denoted by $\tau_i T$, $\tau_i \in [0, 1], \forall i \in \mathcal{I}$, where $\mathcal{I} := \{1, \cdots, K\}$ is the set of the user indices. We have

$$\sum_{i=0}^{K} \tau_i \leq 1$$

since $\tau_i, \forall i \in \bar{\mathcal{I}} := \{0\} \cup \mathcal{I}$, represent the allocated time portions in each block. To simplify analysis, we assume normalized unit time $T = 1$.

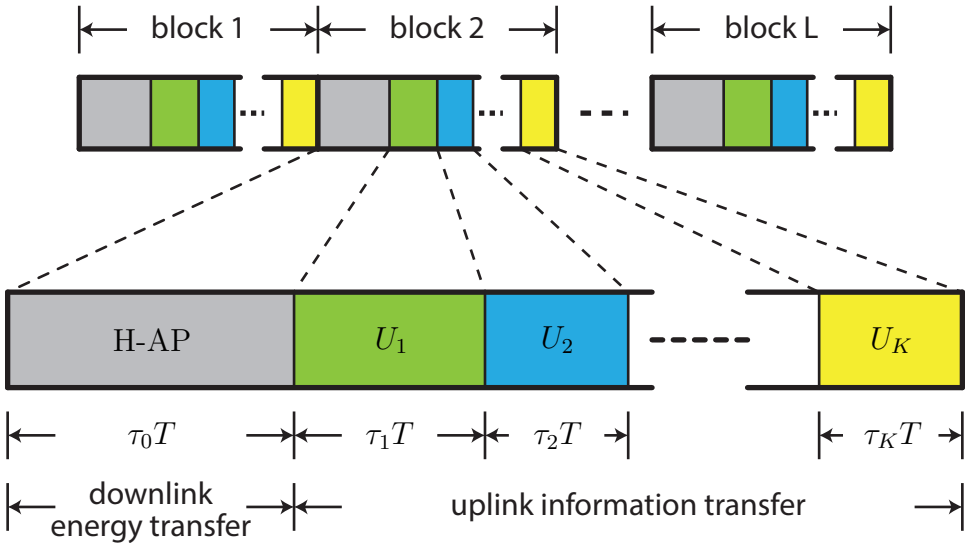

Figure 4.2: Harvest-then-transmit protocol and block structure.

If P_A denotes the transmit power at the H-AP, the amount of energy harvested by each user in the downlink can be expressed as $E_i = \zeta_i P_A h_i \tau_0, \forall i \in \mathcal{I}$, where

h_i denotes the channel power gain of the ith downlink channel and $\zeta_i \in (0,1)$ is the energy harvesting efficiency at ith receiver. For convenience, it is assumed that $\zeta_j = \zeta_k = \zeta, \forall j,k \in \mathcal{I}$ for the remainder of this paper.

After the users replenish their energy during the downlink phase, in the subsequent uplink phase they transmit independent information to the H-AP in their allocated time slots. Instead of using all the energy harvested from the H-AP during current block, we assume that each user can save their energy for future blocks. To distinguish each block, we use superscript (ℓ) to denote the ℓth transmission block. Thus, the energy harvested by user U_i in ℓth block can be written as

$$E_i^{(\ell)} = \zeta P_A h_i^{(\ell)} \tau_0^{(\ell)} = \beta_i^{(\ell)} \tau_0^{(\ell)}. \tag{4.1}$$

.

If we use $W_i^{(\ell)}$ and $F_i^{(\ell)}$ to denote the energy available and consumed by user U_i during the ℓth transmission block, respectively, and consider a finite horizon, say L transmission blocks in total, then the following relation holds

$$W_i^{(\ell)} = \sum_{j=1}^{\ell} E_i^{(j)} - \sum_{j=1}^{\ell-1} F_i^{(j)}, \forall i \in \mathcal{I}, \forall \ell \in \mathcal{J} \tag{4.2}$$

where $\mathcal{J} := \{1, \cdots L\}$ is the set of transmission block indices. Additionally, the amount of energy consumed in each block can not exceed the current energy stored for each user, i.e.,

$$F_i^{(\ell)} \leq W_i^{(\ell)}, \forall i \in \mathcal{I}, \forall \ell \in \mathcal{J}. \tag{4.3}$$

This corresponds to an energy causality constraint.

To simplify our analysis, we introduce parameters $\alpha_i^{(\ell)} \in [0,1], i \in \mathcal{I}, \ell \in \mathcal{J}$,

where $\alpha_i^{(\ell)}$ denotes the energy proportion consumed by ith user in ℓth block. Hence, we can rewrite the energy relations given in (4.3) as

$$F_i^{(\ell)} = \alpha_i^{(\ell)} W_i^{(\ell)}, \forall i \in \mathcal{I}, \forall \ell \in \mathcal{J} \tag{4.4}$$

The achievable uplink throughput of ith user in bits/Hz during ℓth block can be expressed as

$$\begin{aligned} R_i^{(\ell)} &= \tau_i^{(\ell)} \log_2 \left(1 + \frac{g_i^{(\ell)} F_i^{(\ell)}}{\Gamma \sigma^2 \tau_i^{(\ell)}}\right) \\ &= \tau_i^{(\ell)} \log_2 \left(1 + \gamma_i^{(\ell)} \frac{F_i^{(\ell)}}{\tau_i^{(\ell)}}\right) \end{aligned} \tag{4.5}$$

where σ^2 is the variance of the received noise at the H-AP, Γ is the signal-to-noise ratio gap from the additive white Gaussian noise channel capacity due to a practical modulation and coding scheme used and $g_i^{(\ell)}$ represents the channel power gain of the ith uplink channel during ℓth block. It is assumed that the channel reciprocity holds for the downlink WET and uplink WIT, i.e., $h_i^{(\ell)} = g_i^{(\ell)}, \forall i \in \mathcal{I}, \forall \ell \in \mathcal{J}$. Then, the sum throughput of K users over L transmission blocks can be written as

$$R = \sum_{\ell=1}^{L} \sum_{i=1}^{K} R_i^{(\ell)}. \tag{4.6}$$

To facilitate the analysis, we define the time allocation vector for downlink WET $\boldsymbol{\tau}_0$, the time allocation vector for uplink WIT $\boldsymbol{\tau}$ and the energy-consumed proportion

vector $\boldsymbol{\alpha}$, respectively, as

$$\begin{aligned}
\boldsymbol{\tau}_0 &:= \begin{bmatrix} \tau_0^{(1)} & \cdots & \tau_0^{(L)} \end{bmatrix}^{\mathrm{T}} \in \mathbb{R}^{L\times 1} \\
\boldsymbol{\tau} &:= \begin{bmatrix} (\boldsymbol{\tau}^{(1)})^{\mathrm{T}} & \cdots & (\boldsymbol{\tau}^{(L)})^{\mathrm{T}} \end{bmatrix}^{\mathrm{T}} \in \mathbb{R}^{KL\times 1} \\
\boldsymbol{\alpha} &:= \begin{bmatrix} (\boldsymbol{\alpha}^{(1)})^{\mathrm{T}} & \cdots & (\boldsymbol{\alpha}^{(L)})^{\mathrm{T}} \end{bmatrix}^{\mathrm{T}} \in \mathbb{R}^{KL\times 1}
\end{aligned}$$

with

$$\begin{aligned}
\boldsymbol{\tau}^{(\ell)} &:= \begin{bmatrix} \tau_1^{(\ell)} & \cdots & \tau_K^{(\ell)} \end{bmatrix}^{\mathrm{T}} \in \mathbb{R}^{K\times 1}, \forall \ell \in \mathcal{J} \\
\boldsymbol{\alpha}^{(\ell)} &:= \begin{bmatrix} \alpha_1^{(\ell)} & \cdots & \alpha_K^{(\ell)} \end{bmatrix}^{\mathrm{T}} \in \mathbb{R}^{K\times 1}, \forall \ell \in \mathcal{J}.
\end{aligned}$$

Then, the sum throughput over L transmission blocks in (4.6) can be expressed as a function with respect to $(\boldsymbol{\tau}_0, \boldsymbol{\tau}, \boldsymbol{\alpha})$ and is denoted as $R(\boldsymbol{\tau}_0, \boldsymbol{\tau}, \boldsymbol{\alpha})$. Our goal is to find the optimal time allocation vector of downlink WET $\boldsymbol{\tau}_0$, the optimal time allocation vector of uplink WIT $\boldsymbol{\tau}$ and the energy-consumed proportion vector $\boldsymbol{\alpha}$ simultaneously to maximize the sum throughput over L transmission blocks in (4.6). Mathematically, the sum throughput maximization problem is formulated as

Problem 1 (P1).

$$\begin{aligned}
\max_{(\boldsymbol{\tau}_0, \boldsymbol{\tau}, \boldsymbol{\alpha})} \quad & R(\boldsymbol{\tau}_0, \boldsymbol{\tau}, \boldsymbol{\alpha}) \\
s.t. \quad & \sum_{i=0}^{K} \tau_i^{(\ell)} \leq 1, \forall \ell \in \mathcal{J} \\
& \boldsymbol{\tau}_0 \succeq \mathbf{0} \\
& \boldsymbol{\tau} \succeq \mathbf{0} \\
& \mathbf{0} \preceq \boldsymbol{\alpha} \preceq \mathbf{1}.
\end{aligned}$$

We notice that **P1** is a non-convex optimization problem since it's objective function contains non-convex terms. In the following section, we provide an algorithm to solve **P1** by separating it to two sub-problems.

4.3 Optimal Solutions of P1

In this section, we provide the method of finding the optimal solution of **P1**. Instead of solving **P1** directly, we first change **P1** to an equivalent problem **P2**, then consider the problem **P3** to find the optimal time allocation vectors of both downlink WET and uplink WIT by fixing the energy-consumed proportion vector. After solving the equations obtained from the KKT conditions of **P3**, we find a uniform relation between the optimal time allocation of downlink WET and the time allocation of uplink WIT. Thus, **P2** can be transformed into a standard box-constrained optimization problem **P4** by using this relation, which can be efficiently solved by the trust-region-reflective algorithm [27, 28].

First of all, it is straightforward to obtain the following lemma.

Proposition 1. *The optimal time allocation* $(\boldsymbol{\tau}_0^\star, \boldsymbol{\tau}^\star)$ *of* ***P1*** *must satisfy*

$$\sum_{i=0}^{K} \tau_i^{(\ell)\star} = 1, \forall \ell \in \mathcal{J} \tag{4.7}$$

The proof of Proposition 1 can be found in Appendix B.1. From Proposition 1, we can obtain the equivalent optimization problem of **P1** with equality constraints shown in (4.7), which is denoted as **P2**. Since **P2** is also a non-convex problem, it is not easy to solve **P2** directly. To overcome this, we first consider the problem of finding the optimal time allocation vectors of downlink and uplink $(\boldsymbol{\tau}_0^\star, \boldsymbol{\tau}^\star)$ to maximize the sum throughput over L transmission blocks given a fixed energy-

consumed proportion vector $\boldsymbol{\alpha}$. Mathematically, the optimization problem can be formulated as

Problem 3 (P3).

$$\begin{aligned} \max_{(\boldsymbol{\tau}_0, \boldsymbol{\tau})} \quad & R(\boldsymbol{\tau}_0, \boldsymbol{\tau}, \boldsymbol{\alpha}) \\ s.t. \quad & \sum_{i=0}^{K} \tau_i^{(\ell)} = 1, \forall \ell \in \mathcal{J} \\ & \boldsymbol{\tau}_0 \succeq \mathbf{0} \\ & \boldsymbol{\tau} \succeq \mathbf{0} \end{aligned}$$

where the parameters $\boldsymbol{\alpha}$ in **P3** is fixed.

Proposition 2. ***P3*** *is a convex optimization problem.*

The proof of Proposition 2 can be found in Appendix B.2. We know that the necessary Karush-Kuhn-Tucker (KKT) conditions of **P3** are also sufficient and any local maximum solution of **P3** is also a global maximum solution [15]. According to the harvested energy expression in (4.1) and the energy relations given in (4.2) and (4.4), we can obtain the relation between the consumed energy vector $\boldsymbol{F}_i := \begin{bmatrix} F_i^{(1)} & \cdots & F_i^{(L)} \end{bmatrix}^{\mathrm{T}}, \forall i \in \mathcal{I}$ and the allocated time vector for downlink WET $\boldsymbol{\tau}_0$ in matrix form as $\boldsymbol{F}_i = \Psi_i \boldsymbol{\tau}_0, \forall i \in \mathcal{I}$, where the jth row and kth element of $\Psi_i \in \mathbb{R}^{L \times L}$ is

$$\Psi_i(\ell, j) = \begin{cases} p_{i,j}^{(\ell)} \beta_i^{(j)} & , 0 \leq j \leq \ell \\ 0 & , \ell < j \leq L \end{cases} \tag{4.8}$$

and

$$p_{i,j}^{(\ell)} = \alpha_i^{(\ell)} \prod_{k=j}^{\ell-1} (1 - \alpha_i^{(k)}), \forall i \in \mathcal{I}, \forall j \in \mathcal{Q}_\ell, \forall \ell \in \mathcal{J} \tag{4.9}$$

where $\mathcal{Q}_\ell := \{1, \cdots, \ell\}$ is the set of the transmission block indices smaller than index ℓ. If we define parameters $\phi_{i,j}^{(\ell)} := \gamma_i^{(\ell)} \beta_i^{(j)} p_{i,j}^{(\ell)}, \forall i \in \mathcal{I}, \forall j \in \mathcal{Q}_\ell, \forall \ell \in \mathcal{J}$, then we obtain the concrete expression of the throughput of user U_i during ℓth transmission block as

$$R_i^{(\ell)} = \tau_i^{(\ell)} \log_2 \left(1 + \sum_{j=1}^{\ell} \phi_{i,j}^{(\ell)} \frac{\tau_0^{(j)}}{\tau_i^{(\ell)}} \right), \forall i \in \mathcal{I}, \forall \ell \in \mathcal{J}. \tag{4.10}$$

If we plug (4.10) into the KKT conditions, then from the stationarity with respect to $\boldsymbol{\tau}_0$, we have

$$\sum_{\ell=j}^{L} \sum_{i=1}^{K} \left(\frac{\phi_{i,j}^{(\ell)}}{1 + C_i^{(\ell)\star}} \right) = - \left(\nu^{(j)\star} + \lambda_0^{(j)\star} \right) \ln 2. \tag{4.11}$$

Similarly, from the stationarity with respect to $\boldsymbol{\tau}$, it follows

$$f\left(C_i^{(\ell)\star} \right) = - \left(\nu^{(\ell)\star} + \lambda_i^{(\ell)\star} \right) \ln 2, \forall i \in \mathcal{I}, \forall \ell \in \mathcal{J} \tag{4.12}$$

where

$$C_i^{(\ell)\star} \tau_i^{(\ell)\star} = \sum_{j=1}^{\ell} \phi_{i,j}^{(\ell)} \tau_0^{(j)\star}, \forall i \in \mathcal{I}, \forall \ell \in \mathcal{J} \tag{4.13}$$

and

$$f(x) = \ln(1 + x) - \frac{x}{1 + x}.$$

From the equations obtained from the KKT conditions, the optimal time allocation vector of uplink WIT $\boldsymbol{\tau}^\star$ can be uniquely determined by the optimal time allocation vector of downlink WET $\boldsymbol{\tau}_0^\star$, which is summarized in Theorem 1:

Theorem 1. *The optimal time allocation vector of downlink WET $\boldsymbol{\tau}_0^\star$ and the optimal time allocation vector of uplink WIT $\boldsymbol{\tau}^\star$ of **P3** satisfy:*

$$\tau_i^{(\ell)\star} = \frac{\left(1-\tau_0^{(\ell)\star}\right)\sum_{j=1}^{\ell}\phi_{i,j}^{(\ell)}\tau_0^{(j)\star}}{\sum_{i=1}^{K}\sum_{j=1}^{\ell}\phi_{i,j}^{(\ell)}\tau_0^{(j)\star}}, \forall i \in \mathcal{I}, \forall \ell \in \mathcal{J}. \tag{4.14}$$

The relation in (4.14) mainly comes from (4.12) and (4.13) and also the unit time block constraint. The details of the proof can be found in Appendix B.3. Since for any energy-consumed proportion vector $\boldsymbol{\alpha}$, (4.14) always holds. This indicates that we can first obtain a function of $(\boldsymbol{\tau}_0, \boldsymbol{\alpha})$ by replacing $\boldsymbol{\tau}$ in the objective function $R(\boldsymbol{\tau}_0, \boldsymbol{\tau}, \boldsymbol{\alpha})$ of **P2** by using the relations in (4.14). The new objective function, which is denoted as $G(\boldsymbol{\tau}_0, \boldsymbol{\alpha})$, can be expressed as

$$\begin{aligned} &G(\boldsymbol{\tau}_0, \boldsymbol{\alpha}) \\ &= \sum_{\ell=1}^{L}\left(1-\tau_0^{(\ell)}\right)\log_2\left(1+\frac{\sum_{i=1}^{K}\sum_{j=1}^{\ell}\phi_{i,j}^{(\ell)}\tau_0^{(j)}}{1-\tau_0^{(\ell)}}\right). \end{aligned} \tag{4.15}$$

Mathematically, the optimization problem can be formulated in **P4**.

Problem 4 (P4).

$$\begin{aligned} \max_{(\boldsymbol{\tau}_0,\boldsymbol{\alpha})} \quad & G(\boldsymbol{\tau}_0, \boldsymbol{\alpha}) \\ s.t. \quad & \mathbf{0} \preceq \boldsymbol{\tau}_0 \preceq \mathbf{1} \\ & \mathbf{0} \preceq \boldsymbol{\alpha} \preceq \mathbf{1} \end{aligned}$$

If we concatenate the vector $\boldsymbol{\alpha}$ to the vector $\boldsymbol{\tau}_0$ to form a larger vector $\boldsymbol{\delta} \in$

$\mathbb{R}^{(K+1)\times L}$, i.e., $\boldsymbol{\delta} = \begin{bmatrix} \boldsymbol{\tau}_0^{\mathrm{T}} & \boldsymbol{\alpha}^{\mathrm{T}} \end{bmatrix}^{\mathrm{T}}$, then, **P4** is equivalent to the problem of finding the vector $\boldsymbol{\delta}$ to maximize $G(\boldsymbol{\delta})$ subject to $\mathbf{0} \preceq \boldsymbol{\delta} \preceq \mathbf{1}$. This problem is a standard box-constrained optimization problem, which can be solved using the trust-region-reflective algorithm [27, 28].

4.4 Upper Bound

Although the algorithm in Section 4.3 gives us the optimal solution of **P1**, the computational complexity is high when the number of users K or the number of transmission blocks L grows. In this section, we provide an upper bound of the optimal sum throughput in **P1** by relaxing the energy harvesting causality, which gives us a water-filling solution.

In **P1**, we assume that the energy causality condition holds, i.e., the amount of energy consumed in each block can not exceed the current energy stored at each user, which is shown in (4.3). Now we reconsider the optimization problem with the constraint that the total consumed energy does not exceed the total harvested energy at each user, i.e., $\sum_{j=1}^{L} F_i^{(j)} \leq \sum_{j=1}^{L} E_i^{(j)}, \forall i \in \mathcal{I}$. If we plug the relation $\gamma_i^{(\ell)} F_i^{(\ell)} = \sum_{j=1}^{\ell} \phi_{i,j}^{(\ell)} \tau_0^{(j)}, \forall i \in \mathcal{I}, \forall \ell \in \mathcal{J}$ into (4.15) and construct the consumed energy vector $\boldsymbol{F}$ by replacing the element $\alpha_i^{(\ell)}$ with $F_i^{(\ell)}$ in $\boldsymbol{\alpha}$, then, the new objective function can be expressed as

$$T(\boldsymbol{\tau}_0, \boldsymbol{F}) = \sum_{\ell=1}^{L} \left(1 - \tau_0^{(\ell)}\right) \log_2 \left(1 + \frac{\sum_{i=1}^{K} \gamma_i^{(\ell)} F_i^{(\ell)}}{1 - \tau_0^{(\ell)}}\right).$$

Thus, the corresponding optimization problem can be formulated as

Problem 5 (P5).

$$\begin{aligned} \max_{(\boldsymbol{\tau}_0, \boldsymbol{F})} \quad & T(\boldsymbol{\tau}_0, \boldsymbol{F}) \\ s.t. \quad & \mathbf{0} \preceq \boldsymbol{\tau}_0 \preceq \mathbf{1} \\ & \mathbf{0} \preceq \boldsymbol{F} \\ & \sum_{\ell=1}^{L} F_i^{(\ell)} \leq \sum_{\ell=1}^{L} E_i^{(\ell)}, \forall i \in \mathcal{I}. \end{aligned}$$

Observe that **P5** relaxes $(L-1)K$ conditions in **P1**. Thus the maximum sum throughput in **P5** gives us an upper bound of that in **P1**. To solve **P5**, we can first fix $\boldsymbol{\tau}_0$ and find the optimal solution of $\boldsymbol{F}$. If we define a new vector $\tilde{\boldsymbol{F}} := \begin{bmatrix} \tilde{F}^{(1)} & \dots & \tilde{F}^{(L)} \end{bmatrix}^{\mathrm{T}}$ with $\tilde{F}^{(\ell)} = \sum_{i=1}^{K} \gamma_i^{(\ell)} F_i^{(\ell)}, \forall i \in \mathcal{I}, \forall \ell \in \mathcal{J}$, we can obtain the optimal solution.

Theorem 2. *The optimal solution of $\tilde{\boldsymbol{F}}$ when fixing $\boldsymbol{\tau}_0$ is*

$$\tilde{F}^{(\ell)} = \left[\frac{1 - \tau_0^{(\ell)}}{\pi^\star} - (1 - \tau_0^{(\ell)}) \right]^+, \forall \ell \in \mathcal{J}$$

where $\pi^\star \in \mathbb{R}$ is selected to satisfy

$$\sum_{\ell=1}^{L} \tilde{F}^{(\ell)} = \sum_{\ell=1}^{L} \sum_{i=1}^{K} \gamma_i^{(\ell)} E_i^{(\ell)}.$$

The proof of Theorem 2 is mainly obtained by using KKT conditions. The details of the proof can be found in Appendix B.4.

After solving $\tilde{\boldsymbol{F}}$, we notice that the problem of finding optimal $\boldsymbol{\tau}_0$ is a standard box-constrained nonlinear programming problem like **P4**, which can be solved efficiently using the trust-region-reflective algorithm [27, 28].

4.5 Numerical Results

In this section, we compare the maximum sum throughput using energy saving with systems in which the users are assumed to use all their energy within current block. We continue to use the simulation parameters in [54]. The bandwidth is assumed to be 1MHz. Both the downlink and uplink channel power gains are modeled as $h_i^{(\ell)} = g_i^{(\ell)} = 10^{-3}\rho_i^{(\ell)2}D_i^{-\theta},\ i = 1, \cdots, K; \ell = 1, \cdots, L$, where $\theta = 2$ is the pathloss exponent and $\rho_i^{(\ell)}$ represents the channel short-term fading of the ith channel within the ℓth block. The short-term fading is assumed to be Rayleigh distributed, hence $\rho_i^{(\ell)2}$ is an exponentially distributed random variable with unit mean. The K users in the network are equally separated from the H-AP according to $D_i = \frac{D_K}{K} \times i,\ i = 1, \cdots, K$, where $D_K = 10$m. The AWGN at the H-AP receiver is assumed to have a white power spectral density of -160dBm/Hz. For each user, the energy harvesting efficiency for WET is assumed to be $\zeta = 0.5$. We assume that an uncoded quadrature amplitude modulation (QAM) is employed and thus $\Gamma = 9.8$dB.

Fig. 4.3 shows the normalized maximum sum throughput versus the number of transmission blocks for different number of users. As shown in Fig. 4.3, the normalized sum throughput increases when the number of transmission blocks grows. The numbers in the figure shows the possible maximum percentage gain by using energy saving, i.e., 15% for $K = 3$, 13% for $K = 4$ and 12% for $K = 5$. It is observed that when number of users grows, the possible maximum percentage gain will decrease. The black dashed curve shows the upper bound of the maximum sum throughput. It is observed that the upper bound of the maximum sum throughput will be close to the actual maximum sum throughput when K is large.

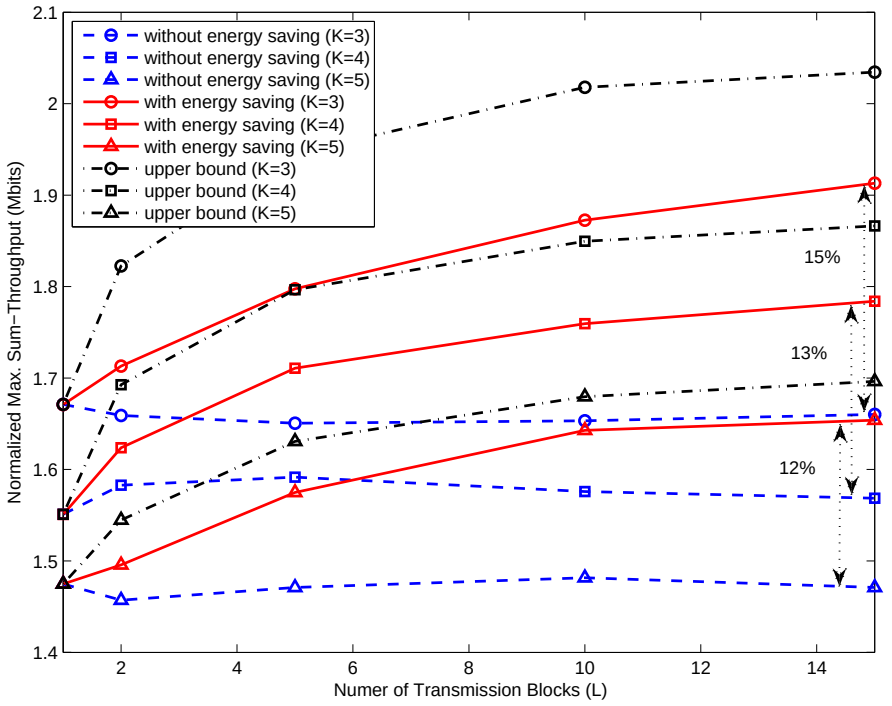

Figure 4.3: Normalized maximum sum throughput vs. number of transmission blocks (L).

4.6 Conclusions

In this chapter, we have studied the throughput maximization problem in WPCN with a finite-horizon energy saving scheme. To obtain the optimal solution, the initial optimization problem is separated into two sub-problems and finally is formulated into a standard box-constrained optimization problem, which can be solved efficiently by the trust-region-reflective algorithm. We have observed that the improvement of the sum throughput with long-term energy saving is not considerable if considering the "oracle" and the computational complexity. This indicates that the initial scheme without energy saving is a practical and favorable strategy in WPCN [54].

Chapter 5

Optimal Wireless Power Transfer with Distributed Transmit Beamforming

This chapter considers the performance of wireless power transfer (WPT) with distributed transmit beamforming (DTB) in a narrowband setting. One or more receive nodes, each equipped with energy harvesting and storage capabilities, provide periodic channel state feedback to a cluster of transmit nodes, each with an independent local oscillator, to facilitate beamforming and passband signal alignment for efficient WPT. Without channel state feedback, the transmit cluster can not align the passband signals at the receivers and the receivers can only harvest incoherent power. Since feedback improves the beamforming gain but requires the receivers to expend energy, there is a fundamental tradeoff between the feedback period and the energy harvesting efficiency. This paper analyzes the optimal feedback period to maximize the weighted mean energy harvesting rate as a function of the oscillator parameters. An optimization problem is formulated and an explicit method to

numerically calculate the globally optimal feedback period is developed. Numerical results are provided to confirm the analysis and demonstrate the sensitivity of the weighted mean energy harvesting rate with respect to the feedback period and the DTB system parameters.

5.1 Introduction

Since the invention of Tesla Coil in 1893 [125], there has been more than a century of research on methods for wirelessly transferring power using radio waves [20]. In recent years, the development of efficient radio frequency (RF) radiation wireless power transfer (WPT) systems has become an active research area, motivated in part by the widespread use of low-power devices that can be charged wirelessly [30]. An example of WPT using RF radiation is the Wireless Identification and Sensing Platform (WISP) [107]. Other recent examples of WPT using RF radiation include harvesting energy from terrestrial television signals [107], cellular base station signals [100], and signals from Wi-Fi routers [124].

Besides RF radiation, there are typically two other types of WPT techniques: inductive coupling (IC) in low-frequency bands and magnetic resonant coupling (MRC) in high-frequency bands [138]. In inductive coupling, the transmitter and receiver coils together form a transformer and power is transferred between the coils by a magnetic field [110]. Inductive coupling is the most mature wireless power technology and is essentially the only technology so far which is used in commercial products such as charging of mobile phones, electric vehicles, and biomedical prosthetic devices implanted in the human body [56, 68, 123, 126]. MRC is a form of inductive coupling in which power is transferred by magnetic fields between two resonant circuits, one in the transmitter and one in the receiver [49,64]. Recently, MRC-

based WPT (MRC-WPT) with multiple transmitters and/or multiple receivers has been studied in the literature [51,79,145]. The WiTricity system is an example of a standardized commercial MRC-WPT system.

A common feature of both IC-WPT and MRC-WPT is that they operate in the near-field. As such, the power strength is attenuated according to the cube of the reciprocal of the distance between the coils [1,90], i.e., power is attenuated at 60 dB per decade. As a result, IC-WPT is typically used for short-range applications in centimeters [57,91] and MRC-WPT is typically used for mid-range applications up to a couple of meters [49,64]. RF-WPT, on the other hand, operates in the far field. While the amount of energy transfer for RF-WPT is typically smaller[1] than in IC-WPT and MRC-WPT, there are several potential advantages of RF-WPT. First, the signal strength of far-field RF transmission over a free-space link is attenuated according to the reciprocal of the distance between transmitter and receiver [74], i.e., power is attenuated at 20 dB per decade. As such, RF-WPT can be be more efficient than IC-WPT and MRC-WPT over longer range links and can be suitable for powering a larger number of devices distributed in a wide area. Second, RF-WPT does not require a large coil like IC-WPT and MRC-WPT. In fact, RF-WPT can use antennas already present in a device for wireless communications. Such antennas can also be used for power transfer or simultaneous wireless information and power transfer (SWIPT) [30]. These characteristics can make RF-WPT appealing in low-cost communication devices [80].

A disadvantage of all WPT techniques over longer ranges is that path loss effects can significantly reduce the amount of power received by energy harvesting devices. To overcome this problem, recent investigations have considered the use of transmit beamforming with RF-WPT, e.g., [143,144]. To achieve coherency in a narrowband

[1]While RF-WPT is generally studied in the context of low-power applications, it has also been considered in scenarios with more substantial power requirements, e.g., [150].

setting, the transmit array must have estimates of the channel phases to each receive node. This channel state information at the transmitter (CSIT) is typically obtained via feedback from the receive nodes. Alternatively, in systems with channel reciprocity, e.g., time-division duplexed (TDD) channels, CSIT can be obtained by having the transmitter directly estimate the channel phases from periodic sounding signals transmitted by the receive nodes. Irrespective of the method in which the CSIT is obtained, the transmit array uses the CSIT to adjust the phases of the passband transmissions so that the signals constructively combine at the intended receiver and the efficiency of WPT is improved.

Recently, researchers have considered the use of *distributed* transmit beamforming (DTB) in wireless communication systems where two or more individual transmit nodes pool their antenna resources to emulate a virtual antenna array [83]. In principle, the distributed array works in the same way as the conventional (centralized) array: the individual transmit nodes use the CSIT obtained either by feedback ("feedback-based" DTB, e.g., [31, 46, 71, 89, 112, 137]) or through channel reciprocity ("reciprocity-based" DTB, e.g., [84, 103]) to form a beam by controlling the phase of their passband transmissions so that the signals constructively combine at an intended receive node. Unlike conventional transceivers, however, a distributed transmit beamformer naturally allows for low-cost deployment of robust large-aperture arrays suitable for efficient wireless communications and WPT.

Another distinction between conventional transmit beamforming and DTB is that each node in a distributed beamformer has an *independent local oscillator*. It is generally assumed in these settings that there is no exogenous source of synchronization of sufficient accuracy to facilitate DTB available to the transmit nodes. Hence, the transmit nodes' local oscillators experience stochastic dynamics and the passband signals from each transmit node experience phase and frequency drift

over time. The transmit nodes can correct for these effects using the CSIT obtained through feedback from the receive nodes (or by exploiting channel reciprocity). Nevertheless, even if the nodes obtain perfect CSIT, it is only a short matter of time until the independent oscillators drift apart and coherence is lost. Periodic feedback is required to maintain coherence.

In this chapter, we consider the use of DTB for WPT. While DTB has been studied extensively in the context of wireless communications (including reports of successful implementations, e.g., [13]), and also studied recently in the context of SWIPT [37, 96], to the best of our knowledge there has been no study of DTB for WPT accounting for (i) the cost of measuring and tracking CSIT and (ii) the effects of time-varying imperfect CSIT caused by tracking errors and oscillator dynamics. While [37, 96] both consider WPT in the context of DTB, these studies focus on SWIPT optimization problems like optimal power splitting under the assumption of perfect CSIT. In this paper, we study the *fundamental tradeoff* between the feedback period and the efficiency of the WPT system as shown notionally in Figure 5.1. We show that there exists optimal feedback period such that the receivers can maximize their *net* mean energy harvesting rate after the cost of feedback and accounting for losses due to errors in the channel state information. This paper is focused on the question of how to find a globally optimal feedback period to maximize the mean energy harvesting rate at the receivers. While the focus of this paper is on WPT, we note that the techniques developed in this paper naturally extend to SWIPT since DTB has been extensively studied in the wireless communications context.

The DTB WPT problem is different from the DTB communications problem due to the fundamental tradeoff between the feedback period and the efficiency of the WPT system as shown notionally in Figure 5.1. The main contributions of this chapter are summarized as follows:

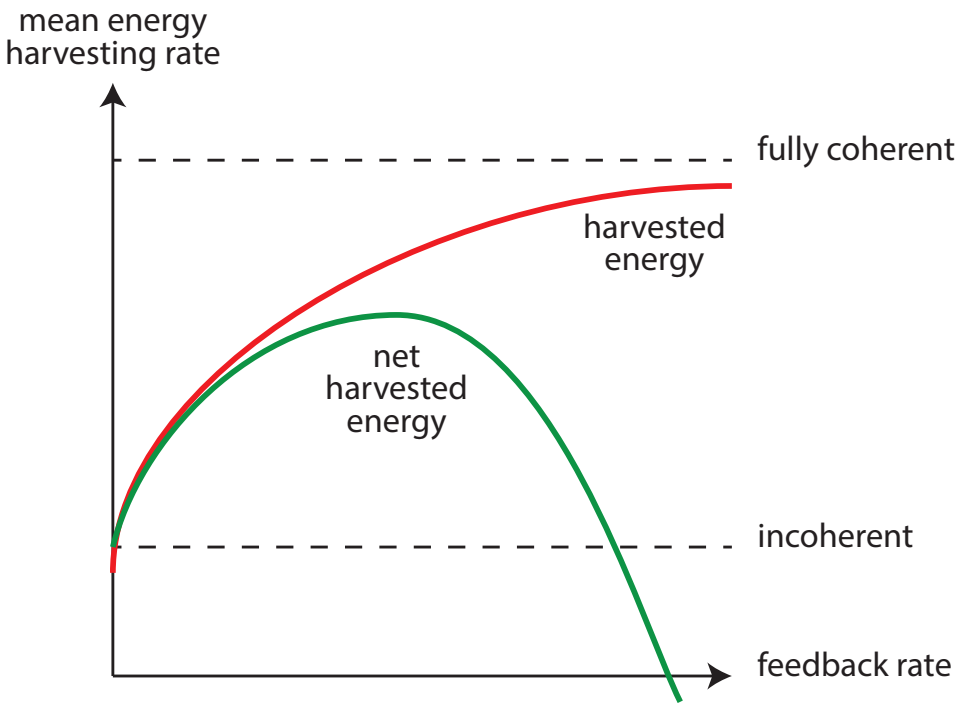

Figure 5.1: Fundamental tradeoff between the feedback rate and the mean energy harvesting rate of the WPT system. The net harvested energy accounts for the cost of feedback.

- We develop a new model for WPT with DTB, explicitly accounting for losses caused by imperfect channel state information and independent oscillator dynamics and also accounting for the cost of feedback energy from the receive nodes.

- We formulate a "Normalized Weighted Mean Energy Harvesting Rate" (NWMEHR) maximization problem to select the feedback period to maximize the weighted averaged amount of net energy harvested by the receive nodes per unit of time as a function of the oscillator parameters. By maximizing the NWMEHR, the receive nodes maximize the *net* weighted harvested energy after feedback.

- Since the NWMEHR objective function is non-convex and implicit (involving the solution of a discrete-time algebraic Riccati equation), we develop an explicit method to numerically calculate the globally optimal feedback period. Our method solves the problem in two steps: (i) bounding the search region into a closed interval and (ii) applying the DIRECT algorithm [52] on the bounded search region to find the globally optimal solution.

Our approach is distinguished from the prior work by the fact that we explicitly consider the effect of time-varying errors in the channel state information caused by tracking errors and independent local oscillators and also account for the cost of feedback energy in the WPT setting. This reveals the fundamental tradeoff shown in Fig. 5.1, the precise formulation of the NWMEHR optimization problem, and an explicit method to optimize the net harvested energy as a function of the oscillator parameters.

5.2 System Model And Problem Formulation

In this section, we first introduce in Section 5.2.1 the system model and notation for the relevant parameters in "feedback-based" DTB. We then formulate the mean energy harvesting rate maximization problem in Section 5.2.3.

For conciseness, our presentation focuses on "feedback-based" DTB. We point out, however, that the main concepts developed here also apply to "reciprocity-based" DTB since obtaining CSIT via reciprocity requires the receive nodes to periodically expend energy for reverse link channel sounding. While the details of the protocol and system parameters differ, both feedback-based DTB and reciprocity-based DTB possess the same fundamental tradeoff between the feedback rate (reverse link channel sounding rate) and WPT efficiency.

5.2.1 System Model

We assume a system with N_t transmit nodes and N_r receive nodes. All forward link channels are modeled as narrowband, linear, and time invariant (LTI). All nodes are assumed to possess a single isotropic antenna[2]. Adopting the convention that the transmit nodes are enumerated as $i = 1, \cdots, N_t$ and the receive nodes are enumerated as $j = 1, \cdots, N_r$, we denote the channel from transmit node i to receive node j as $g_{i,j} \in \mathbb{C}$. To facilitate beamforming toward the receive nodes in the forward link, we assume a "feedback-based" DTB protocol like [31,46,71,89,112, 137] where the transmit nodes obtain CSIT through periodic forward link channel measurements and channel state feedback from the receive nodes on the reverse link. This protocol and its relevant parameters are illustrated in Fig. 5.2.

[2]Our focus on single antennas is motivated by clarity of exposition. The techniques developed in this paper can be extended to the case where nodes have more than one antenna at the expense of some additional notational complexity.

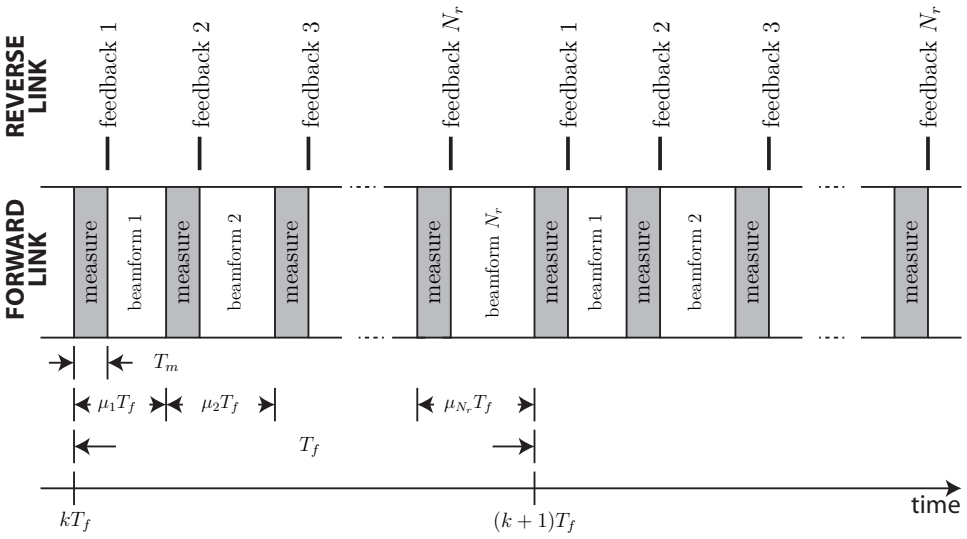

Figure 5.2: Distributed transmit beamforming periodic protocol with frame period T_f.

As shown in Fig. 5.2, each frame of the feedback-based DTB protocol has a duration of T_f and is composed of N_r slots. The j^{th} slot has a duration of $\mu_j T_f$, where the factors $\{\mu_j\}_{j=1}^{N_r}$ are all in the range $(0, 1)$ and their summation is normalized to one, i.e., $\sum_{j=1}^{N_r} \mu_j = 1$. Each slot contains a channel measurement interval followed immediately by a beamforming interval. During the channel measurement interval, each transmit node separately broadcasts a pilot of length T_0 (including any necessary guard times) to the receive nodes. The channel measurement interval length is then $T_m = N_t T_0$. All of the receive nodes use the pilots received during the channel measurement intervals to update their channel estimates. No beamforming or energy harvesting occurs during channel measurement intervals.

At the end of the channel measurement interval, a single receive node provides channel state feedback to the transmit cluster. The receive node is assumed to send L bits of information for each channel measurement and, hence, a receive node provides $N_t L$ total bits of feedback in its slot. We assume the time required to send this feedback is small so that the beamforming interval to the receive node providing the feedback begins immediately after the measurement interval. During

the beamforming interval of receive node j, receive node j harvests energy from the (approximately) coherent signals from the transmit cluster while all other receive nodes $\ell \in \{1, \ldots, N_r\} \backslash j$ harvest incoherent energy.

5.2.2 Harvested Energy Analysis

Receive nodes harvest approximately coherent energy during their beamforming interval and also harvest incoherent energy during the beamforming intervals of the other receive nodes. No energy is harvested during the channel measurement periods. We denote the beamforming power at the j^{th} receive node at time t as $J^{(j)}(t)$ and note that $J^{(j)}(t)$ is a stochastic process since the channel estimates are noisy and the independent clocks experience stochastic dynamics. We further denote the ensemble averaged beamforming power as $\overline{J}^{(j)}(t) = \mathbb{E}[J^{(j)}(t)]$. The total average energy harvested by the j^{th} receive node during the k^{th} frame period can be written as

$$E_b^{(j)}[k] = \eta \left[\int_{t \in \mathcal{T}_b^{(j)}[k]} \overline{J}^{(j)} \left(t - \sum_{s=1}^{j-1} \mu_s T_f \right) \, dt + P_{\text{inc}}^{(j)} \sum_{\substack{s=1 \\ s \neq j}}^{N_r} (\mu_s T_f - T_m) \right] \tag{5.1}$$

where $\eta \in (0, 1)$ is the harvesting efficiency, $\mathcal{T}_b^{(j)}[k]$ is the beamforming interval in the j^{th} slot of the k^{th} frame, and $P_{\text{inc}}^{(j)}$ is the incoherent beamforming power at the j^{th} receive node. Note that this latter term accounts for the fact that the j^{th} receive node harvests incoherent beamforming power in the non-j^{th} beamforming slots. We further define the *steady-state* average energy harvested by the j^{th} receive node as $\overline{E}_b^{(j)} = \lim_{k \to \infty} E_b^{(j)}[k]$.

During the beamforming interval in the j^{th} slot, the transmitters attempt to align their phases so that the signals arrive with a common phase and combine coherently at the j^{th} receive node. We denote the signal at the j^{th} receive node

from i^{th} transmit node as

$$r^{(i,j)}(t) = \sqrt{P_0}|g_{i,j}|e^{j\left(\phi+\tilde{\phi}^{(i,j)}(t)\right)} \tag{5.2}$$

where P_0 is the common per-node transmit power, ϕ is the nominal beamforming phase and $\tilde{\phi}^{(i,j)}(t)$ is the phase error of the transmission from the i^{th} transmit node to the j^{th} receive node at prediction time $t > 0$ after the end of the measurement interval. If perfect coherence is achieved, then $\tilde{\phi}^{(i,j)}(t) = 0$ and $\overline{J}^{(j)}(t) = \mathbb{E}\left\{\left|\sum_{i=1}^{N_t} r^{(i,j)}(t)\right|^2\right\} = P_0\left(\sum_{i=1}^{N_t}|g_{i,j}|\right)^2$. In practice, however, the phase errors will not be zero due to channel estimation errors and the effect of stochastic clock drifts (as discussed in Section 5.3). In fact, when the phase errors become large, the mean beamforming power is $\overline{J}^{(j)}(t) = P_0\sum_{i=1}^{N_t}|g_{i,j}|^2 = P_{\text{inc}}^{(j)}$, i.e., large phase errors result in incoherent average power.

To quantify the effect of nonzero phase errors on the steady-state beamforming power in the j^{th} slot, we assume $\tilde{\phi}^{(i,j)}(t)$ is a spatially independent and identically distributed (i.i.d.) zero mean Gaussian random process with variance $\sigma_\phi^2(\mu_j T_f, t)$ parameterized by the frame period T_f and the prediction interval t (this assumption will be justified in Section 5.3). With this assumption, the mean beamforming power at prediction time t for the j^{th} receive node can be calculated as

$$\begin{aligned}\overline{J}^{(j)}(T_f, t) &= \mathbb{E}\left\{\left|\sum_{i=1}^{N_t} r^{(i,j)}(t)\right|^2\right\} \\ &= P_{\text{inc}}^{(j)}\left[1 + (\rho_j - 1)e^{-\sigma_\phi^2(\mu_j T_f, t)}\right]\end{aligned} \tag{5.3}$$

where $\rho_j = \dfrac{\left(\sum_{i=1}^{N_t}\left|g_{i,j}\right|\right)^2}{\sum_{i=1}^{N_t}\left|g_{i,j}\right|^2}$. When $\sigma_\phi^2(\mu_j T_f, t)$ is small, note that the mean beamforming power $\overline{J}^{(j)}(T_f, t) \approx P_{\text{inc}}^{(j)}\rho_j = P_0\left(\sum_{i=1}^{N_t}|g_{i,j}|\right)^2$ and the distributed array achieves

approximately coherent power. Similarly, when $\sigma_\phi^2(\mu_j T_f, t)$ is large, $\overline{J}^{(j)}(T_f, t) \approx P_{\text{inc}}^{(j)}$ and the distributed array achieves approximately incoherent power. We can combine (5.3) with (5.1) to write

$$\overline{E}_b^{(j)} = \eta P_{\text{inc}}^{(j)} \left[(\rho_j - 1) \int_{T_m}^{\mu_j T_f} e^{-\sigma_\phi^2(\mu_j T_f, t)} \, dt + (T_f - N_r T_m) \right]. \tag{5.4}$$

where we use the fact that the steady-state beamforming power of each receive node is periodic with period T_f.

5.2.3 NWMEHR Maximization Problem

We are interested in maximizing the steady-state weighted sum rate of the net energy transferred to the receive nodes in the system. As a baseline, we can consider the scenario where the receive nodes simply harvest incoherent transmissions with no feedback. In this case, since the entire frame period is spent harvesting incoherent power, the weighted sum rate of the net energy transferred to the receive nodes in the system can be expressed as

$$\overline{C} = \eta \sum_{j=1}^{N_r} \gamma_j P_{\text{inc}}^{(j)} = \eta \sum_{j=1}^{N_r} \gamma_j P_0 \sum_{i=1}^{N_t} \left| g_{i,j} \right|^2 \tag{5.5}$$

where γ_j is the energy harvesting weighting factor for receiver j. If the receive nodes provide channel state feedback to improve coherence, the net amount of energy harvested by the receive nodes in one frame is the amount of energy received via beamforming (and incoherent harvesting) minus the amount of energy used by the receiver for channel state feedback in that frame. We define the normalized weighted

mean energy harvested rate (NWMEHR) as

$$\mathsf{NWMEHR} = \frac{1}{\overline{C}T_f} \sum_{j=1}^{N_r} \gamma_j \left(\overline{E}_b^{(j)} - E_r^{(j)} \right) \tag{5.6}$$

where $\overline{E}_b^{(j)}$ is from (5.1) and $E_r^{(j)}$ is the energy used by the j^{th} receive node for channel state feedback in one frame. Values of $\mathsf{NWMEHR} > 1$ correspond to scenarios where channel state feedback with DTB improves the efficiency of the WPT with respect to simple incoherent energy harvesting.

Using the results from the previous section, we can rewrite (5.6) as

$$\mathsf{NWMEHR} = 1 + \frac{1}{T_f} \left(\frac{\eta}{\overline{C}} \sum_{j=1}^{N_r} \gamma_j P_{\text{inc}}^{(j)} (\rho_j - 1) \int_{T_m}^{\mu_j T_f} e^{-\sigma_\phi^2 (\mu_j T_f, t)} \, dt - D \right) \tag{5.7}$$

with

$$D = N_r T_m + \frac{\sum_{j=1}^{N_r} \gamma_j E_r^{(j)}}{\overline{C}}. \tag{5.8}$$

where D corresponds to the total energy loss in one frame due to the measurement and the energy consumption for feedback.

The goal is to find the optimal frame period $T_f^\star$ (or, equivalently, optimal frame rate $1/T_f^\star$) to maximize the NWMEHR. Mathematically, we can formulate the problem as

Problem 6 (**NWMEHR maximization problem**)**.**

$$\begin{aligned} \underset{T_f}{\text{maximize}} \quad & \mathsf{NWMEHR} \\ \text{subject to} \quad & T_f \in \left[\frac{T_m}{\mu_{\min}}, \infty \right) \end{aligned}$$

where $\mu_{\min} = \min \{\mu_1, \cdots, \mu_{N_r}\}$.

In Section 5.4, we show that Problem 6 can sometimes be infeasible, i.e., there may be no solution in the feasible region $[T_m/\mu_{\min}, \infty)$ and, instead, the NWMEHR is maximized when the frame period $T_f = \infty$. This situation indicates that optimal strategy is for all the receive nodes to simply harvest incoherent power from the transmit nodes without any feedback.

5.3 Forward Link Channel Tracking and Prediction

The previous section established that the beamforming power (and resulting energy harvesting efficiency) is completely characterized by the variance $\sigma_\phi^2(T,t)$ of the phase error random process parameterized by the slot period T and the prediction interval t. In this section, we connect these statistics to the properties of the independent oscillators used by the transmit and receive nodes in the DTB system.

Figure 5.3 shows the *effective* narrowband channel model from transmit node i to receive node j which includes the effects of propagation and carrier offset. Transmission from transmit node i to receive node j are conveyed on a carrier with nominal frequency ω_F, incur a phase shift of $\psi^{(i,j)} = \angle g_{i,j}$ over the wireless channel, and are then downmixed by receive node j using its local carrier nominally at ω_F. At time t, the effective narrowband channel from transmit node i to receive node j is modeled as

$$h_{i,j}(t) = g_{i,j} e^{j\left(\phi_t^{(i)}(t) - \phi_r^{(j)}(t)\right)} = |g_{i,j}| e^{j\phi^{(i,j)}(t)} \tag{5.9}$$

where $\phi_t^{(i)}(t)$ and $\phi_r^{(j)}(t)$ are the local carrier phase offsets at transmit node i and receive node j, respectively, at time t with respect to an ideal carrier reference, and

$\phi^{(i,j)}(t) = \phi_t^{(i)}(t) - \phi_r^{(j)}(t) + \psi^{(i,j)}$ is the pairwise phase offset after propagation between transmit node i and receive node j at time t. In this paper, it is assumed that the channel magnitudes $|g_{i,j}|$ for $i = 1, \cdots, N_t$ and $j = 1, \cdots, N_r$ are fixed (or slowly varying) and perfectly known.

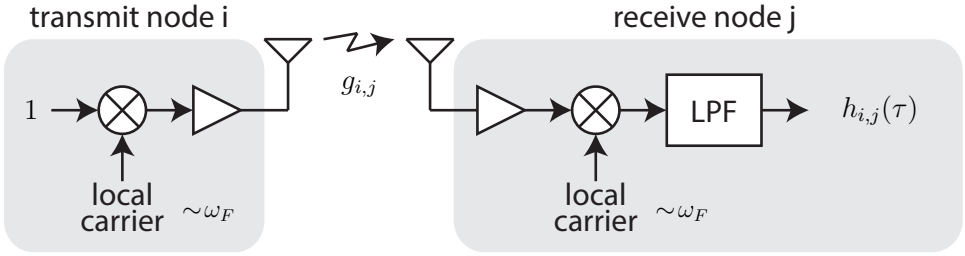

Figure 5.3: Effective narrowband channel model including the effect of propagation, transmit and receive gains, and carrier offset.

Each node in the system is assumed to have an independent local oscillator. These local oscillators behave stochastically, causing phase offset variations in each effective channel from each transmit node to the receive node. To characterize the oscillator dynamics of each node in the system, we consider a two-state model [33,43] and define the state of the i^{th} transmit node's carrier as $\boldsymbol{x}_t^{(i)}(t) := [\phi_t^{(i)}(t), \omega_t^{(i)}(t)]^{\mathrm{T}}$, where $\phi_t^{(i)}(t)$ and $\omega_t^{(i)}(t)$ correspond to the carrier phase and frequency offsets in radians and radians per second at transmit node $i \in \{1, \cdots, N_t\}$ with respect to some reference carrier[3]. From [43], the dynamics of the i^{th} transmit node's carrier can be expressed as

$$\frac{d}{dt}\boldsymbol{x}_t^{(i)} = \begin{bmatrix} 0 & 1 \\ 0 & 0 \end{bmatrix} \boldsymbol{x}_t^{(i)} + \boldsymbol{u}_t^{(i)}(t) \tag{5.10}$$

where $\boldsymbol{u}_t^{(i)}(t) \sim \mathcal{N}(0, \omega_F \cdot \mathrm{diag}(\alpha, \beta))$ is the white Gaussian process noise vector

[3]Although the focus here is on a two-state model, the approach described here can also be applied to higher order oscillator models, e.g., [117, 120], with some additional notational and computational complexity.

parameterized by the nominal forward link carrier frequency ω_F and the white frequency noise and random walk frequency noise oscillator stability parameters α (units of seconds) and β (units of Hertz), respectively. We assume the process noise parameters to be identical at all nodes in the system. The receive nodes in the system also have independent local oscillators used to generate carriers for downmixing that are governed by the same dynamics as (5.10) with state $\boldsymbol{x}_r^{(j)}(t)$, process noise $\boldsymbol{u}_r^{(j)}(t)$ for $j = 1, \cdots, N_r$. We further define the *pairwise offset* state between the i^{th} transmit node and the j^{th} receive node after propagation as

$$\boldsymbol{\delta}^{(i,j)}(t) = \boldsymbol{x}_t^{(i)}(t) + \begin{bmatrix} \psi^{(i,j)} \\ 0 \end{bmatrix} - \boldsymbol{x}_r^{(j)}(t). \tag{5.11}$$

For any sampling period T and sampling instances $t = nT$, standard methods can be used to write the discrete-time pairwise offset state update

$$\boldsymbol{\delta}^{(i,j)}[n+1] = \boldsymbol{F}(T)\boldsymbol{\delta}^{(i,j)}[n] + \boldsymbol{G}\boldsymbol{w}^{(i,j)}[n] \tag{5.12}$$

where

$$\boldsymbol{F}(T) = \begin{bmatrix} 1 & T \\ 0 & 1 \end{bmatrix}, \quad \boldsymbol{G} = \begin{bmatrix} 1 & 0 & -1 & 0 \\ 0 & 1 & 0 & -1 \end{bmatrix}, \text{ and } \boldsymbol{w}^{(i,j)}[n] = \begin{bmatrix} \boldsymbol{u}_t^{(i)}[n] \\ \boldsymbol{u}_r^{(j)}[n] \end{bmatrix}. \tag{5.13}$$

The discrete-time process noise vectors $\boldsymbol{u}_t^{(i)}[n] \overset{\text{i.i.d.}}{\sim} \mathcal{N}(0, \boldsymbol{C}(T))$ and $\boldsymbol{u}_r^{(j)}[n] \overset{\text{i.i.d.}}{\sim} \mathcal{N}(0, \boldsymbol{C}(T))$ with

$$\boldsymbol{C}(T) = \omega_F^2 \begin{bmatrix} \alpha T + \beta\frac{T^3}{3} & \beta\frac{T^2}{2} \\ \beta\frac{T^2}{2} & \beta T \end{bmatrix}. \tag{5.14}$$

Suppose the sampling period $T = T$ and that forward link channel measurements

occur at $t = nT$ for $n = 0, 1, \ldots$. During the measurement intervals, we assume the pilot signals from each transmit node are short such that they only provide a useful estimate of the pairwise phase offset. Specifically, for the i^{th} transmit node's pilot at the j^{th} receive node in slot s, we assume an observation of the form

$$y^{(i,j)}[n] = \boldsymbol{h}\boldsymbol{\delta}^{(i,j)}[n] + v^{(i)}[n] \tag{5.15}$$

where $\boldsymbol{h} = [1, 0]$ and $v^{(i)}[k] \overset{\text{i.i.d.}}{\sim} \mathcal{N}(0, R)$ is the measurement noise which is assumed to be spatially and temporally i.i.d. These observations facilitate tracking and prediction of the pairwise offset states at the receive nodes. We assume receive node j implements a bank of N_t separate two-state Kalman filters to track and predict the states $\boldsymbol{\delta}^{(i,j)}[n]$ for all $i = 1, \ldots, N_t$. When receive node j provides feedback to the transmit cluster after the n^{th} measurement, it transmits the most recent Kalman filter estimates $\hat{\boldsymbol{\delta}}^{(i,j)}[n \,|\, n]$ for all $i = 1, \ldots, N_t$. The transmit nodes use these estimates to generate predictions $\hat{\boldsymbol{\delta}}^{(i,j)}[n + t \,|\, n] = \boldsymbol{F}(t)\hat{\boldsymbol{\delta}}^{(i,j)}[n \,|\, n]$ for $t > 0$ in the subsequent beamforming interval to receive node j. Note that t is a continuous parameter and $\boldsymbol{F}(t)$ is defined for all $t > 0$.

It can be shown that the system described in (5.12) and (5.15) is completely observable and completely controllable, hence the Kalman filter steady-state prediction covariance

$$\boldsymbol{P}(T) = \begin{bmatrix} P_1(T) & P_2(T) \\ P_2(T) & P_3(T) \end{bmatrix} \in \mathbb{R}^{2\times 2} \tag{5.16}$$

is the unique positive definite solution of the discrete-time algebraic Riccati equation

(DARE) [11]

$$\boldsymbol{P}(T)=\boldsymbol{F}(T)\left[\boldsymbol{P}(T)-\frac{\boldsymbol{P}(T)\boldsymbol{h}^{\mathrm{T}}\boldsymbol{h}\boldsymbol{P}(T)}{\boldsymbol{h}\boldsymbol{P}(T)\boldsymbol{h}^{\mathrm{T}}+R}\right]\boldsymbol{F}^{\mathrm{T}}(T)+\boldsymbol{Q}(T) \tag{5.17}$$

where

$$\begin{aligned}\boldsymbol{Q}(t)=\boldsymbol{G}\mathrm{cov}\left\{\boldsymbol{w}^{(i,j)}[k]\right\}\boldsymbol{G}^{\mathrm{T}} &= \begin{bmatrix} At+\frac{B}{3}t^3 & \frac{B}{2}t^2 \\ \frac{B}{2}t^2 & Bt \end{bmatrix} \\ &= \begin{bmatrix} Q_1(t) & Q_2(t) \\ Q_2(t) & Q_3(t) \end{bmatrix}\end{aligned} \tag{5.18}$$

with $A=2\omega_F^2\alpha$ and $B=2\omega_F^2\beta$. Note that $\boldsymbol{P}(T)\succ\boldsymbol{0}$ corresponds to the covariance matrix of the steady-state Kalman filter predictions just prior to a measurement/observation. The Kalman filter steady-state *estimation* covariance immediately after receiving an observation can be expressed as

$$\boldsymbol{S}(T)=\begin{bmatrix} S_1(T) & S_2(T) \\ S_2(T) & S_3(T) \end{bmatrix}=\boldsymbol{P}(T)-\frac{\boldsymbol{P}(T)\boldsymbol{h}^{\mathrm{T}}\boldsymbol{h}\boldsymbol{P}(T)}{\boldsymbol{h}\boldsymbol{P}(T)\boldsymbol{h}^{\mathrm{T}}+R}. \tag{5.19}$$

We denote $\hat{\boldsymbol{S}}(T,t)=\boldsymbol{F}(t)\boldsymbol{S}(T)\boldsymbol{F}^{\mathrm{T}}(t)$ and note that the (1,1) element of this matrix can be written as

$$\hat{S}_1(T,t)=S_1(T)+2tS_2(T)+t^2S_3(T). \tag{5.20}$$

Moreover, since the steady-state prediction covariance at any prediction time $t>0$ after an observation, i.e., after the commencement of beamforming, can be written

as $\hat{\boldsymbol{P}}(T,t) = \hat{\boldsymbol{S}}(T,t) + \boldsymbol{Q}(t)$, we have

$$\begin{aligned}\hat{P}_1(T,t) &= \hat{S}_1(T,t) + Q_1(t) \\ &= S_1(T) + 2tS_2(T) + t^2 S_3(T) + \omega_F^2 t\left(\alpha + \beta\frac{t^2}{3}\right)\end{aligned} \tag{5.21}$$

Note that $\hat{P}_1(T,t)$ is the (1,1) element of the Kalman filter's prediction covariance at prediction time $t > 0$ after an observation. This quantity corresponds to the steady-state *phase prediction variance* of the Kalman filter. Since this quantity fully characterizes the steady-state expected beamforming gain of the transmit array, we denote $\sigma_\phi^2(T,t) = \hat{P}_1(T,t)$.

Recall that in Section 5.2, we obtain the expression of NWMEHR in terms of $\sigma_\phi^2(\mu_j T_f, t)$ for $j = 1, \cdots, N_r$. In this section, we have shown that $\sigma_\phi^2(\mu_j T_f, t)$ for any j is an implicit function with respect to T_f. Therefore, combining these two results, we finally obtain an implicit function of NWMEHR only in terms of the frame period T_f. In the next section, we develop a numerical method to find the optimal frame period to maximize the NWMEHR.

5.4 Analysis

This section analyzes Problem 1 and develops a method to numerically compute the globally optimal frame period T_f to maximize the NWMEHR. An overview of the modeling and optimization methodology is shown in Figure 5.4. We assume all of the process and measurement noise parameters are known by the receive nodes. If these parameters are unknown, covariance estimation techniques such as [75], can be used to estimate these parameters as part of the Kalman filtering process. We also assume the slot duration factors are given, perhaps determined by a separate

process aware of the charging state of each receiver. Given a frame period T_f, the NWMEHR can be calculated from (5.6). To find the globally optimum value of T_f, the main steps we will follow in this section are (i) bounding the feasible region and (ii) applying the direct algorithm on the bounded region.

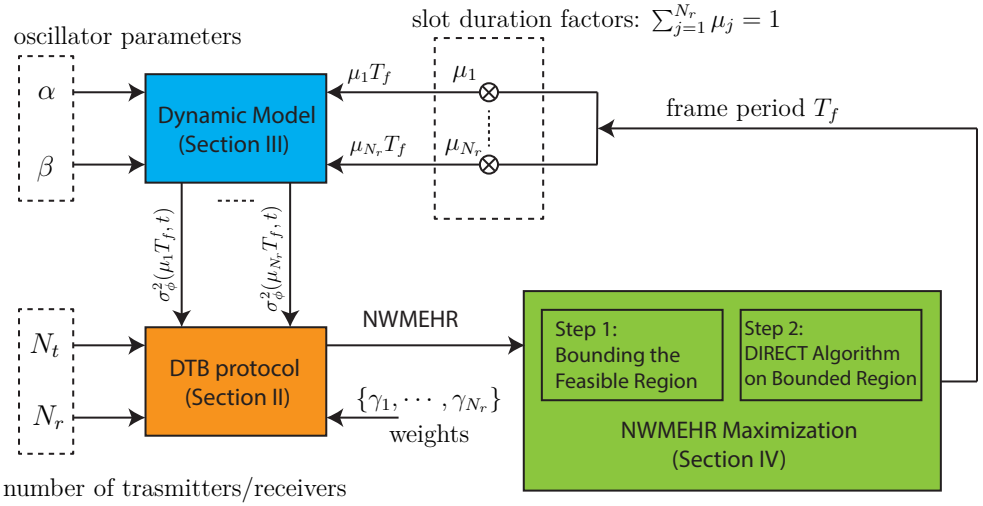

Figure 5.4: Overview of the NWMEHR maximization problem.

First, some basic properties of Problem 6 are summarized below:

(1) The objective function of Problem 6 is only a function of one variable: the frame period T_f.

(2) The objective function of Problem 6 is nonlinear and non-convex.

(3) The objective function of Problem 6 is implicit since it requires solving the DARE in (5.17), which, in general, has no closed-form explicit solution.

(4) Problem 6 has one simple linear inequality constraint and the feasible region of Problem 6 is unbounded.

We will first address the problem of the unbounded feasible region in the following section. In the process of bounding the feasible region, we can also check a necessary condition for the existence of a finite solution to Problem 6.

5.4.1 Bounding the Feasible Region

In this section, we develop an efficient method to bound the feasible region for Problem 6 into a *closed* interval. To facilitate the analysis, the following lemma describes some basic properties of the NWMEHR function defined in (5.7).

Lemma 1. *The NWMEHR defined in (5.7) has the following properties:*

$$\lim_{T_f \to \infty} \mathsf{NWMEHR} = 1 \text{ } \textit{from below, and}$$

$$\sup_{T_f \in \left[\frac{T_m}{\mu_{\min}}, \infty\right)} \mathsf{NWMEHR} \in \left[1, 1 + (\overline{\rho} - 1)\mu_{\max}\right),$$

where

$$\overline{\rho} = \frac{\sum_{j=1}^{N_r} \gamma_j P_{\text{inc}}^{(j)} \rho_j}{\sum_{j=1}^{N_r} \gamma_j P_{\text{inc}}^{(j)}}, \text{ } \textit{and} \tag{5.22}$$

$$\mu_{\max} = \max\{\mu_1, \cdots, \mu_{N_r}\}. \tag{5.23}$$

Proof. Please refer Appendix C.1. □

To illustrate these properties, Figure 5.5 shows examples of the NWMEHR and the NWMEHR with $E_r = 0$ for systems with two different oscillator parameters from Table 5.1 based on the "Rakon RPFO45" [2] and the "poor XO" [59], respectively. For this example, we assume $N_t = 15$ transmit nodes and $N_r = 2$ receive nodes and weights $\gamma = \{1, 1\}$ and slot duration factors $\mu = \{0.3, 0.7\}$. For both the poor XO and the Rakon RPFO45, the NWMEHR with $E_r = 0$ increases with the slot rate as expected. The NWMEHR after accounting for the cost of feedback, however, is monotonically decreasing for the system with the poor XO. In this case, since $\mathsf{NWMEHR} < 1$ for all $T_f \in [T_m/\mu_{\min}, \infty)$, the NWMEHR is maximized when the receive nodes provide no feedback ($1/T_f = 0$) and simply harvest incoherent power

from the transmit nodes. For Rakon RPFO45, we observe the NWMEHR deceases rapidly when $1/T_f$ is large and achieves its global maxima of $\mathsf{NWMEHR} \approx 3.0$ at $1/T_f \approx 0.14$ Hz. In this case, the receiver achieves the maximum energy harvesting rate by providing periodic feedback to the transmit nodes. The zoomed inset in Figure 5.5 also shows the NWMEHR converging to 1 from below as $T_f \to \infty$ for Rakon RPFO45.

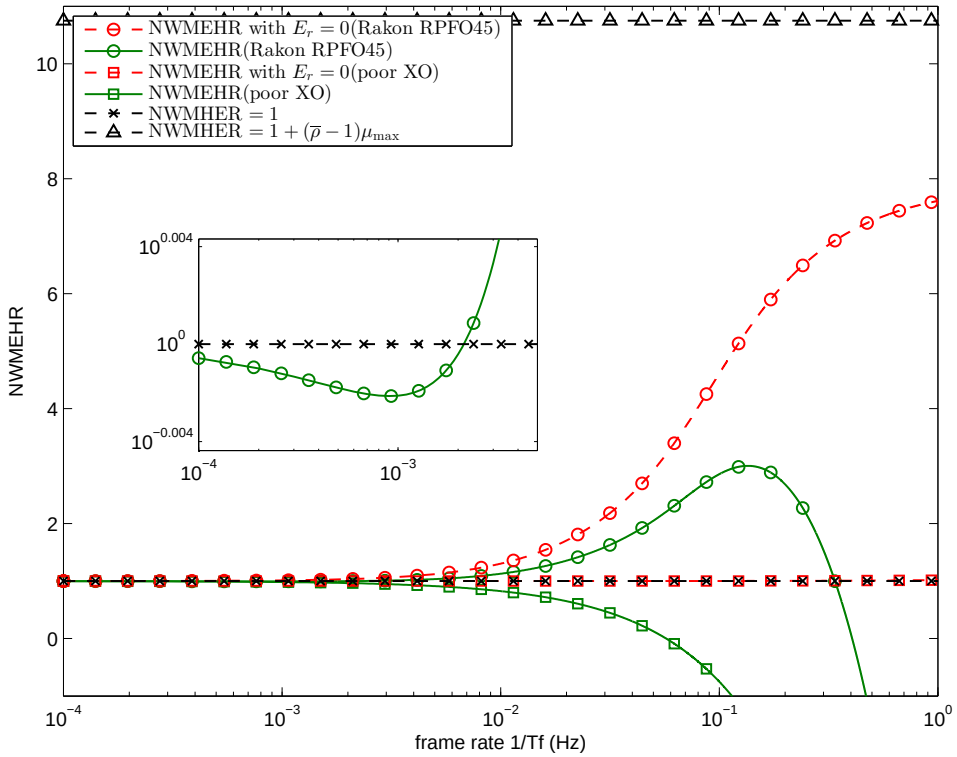

Figure 5.5: Two examples of the NWMEHR and the NWMEHR with $E_r = 0$ versus the frame rate $1/T_f$.

Since we are interested in slot periods that result in energy harvesting rates that exceed incoherent energy harvesting, we can define the set

$$\mathcal{X}_{\mathsf{NWMEHR}} = \left\{ T_f \geq \frac{T_m}{\mu_{\min}} : \mathsf{NWMEHR} \geq 1 \right\}. \tag{5.24}$$

An important consequence of Lemma 1 is that $\mathcal{X}_{\mathsf{NWMEHR}}$ must be bounded or empty.

Due to the implicit nature of the NWMEHR function, however, finding the exact bounds on this set can be difficult. To facilitate analysis, we propose a function $\Phi(T_f)$ which is an upper bound for the NWMEHR for all $T_f \geq T_m/\mu_{\min}$. Hence, the set $\mathcal{X}_\Phi = \{T_f \geq T_m/\mu_{\min} : \Phi(T_f) \geq 1\}$ is a superset of $\mathcal{X}_{\mathsf{NWMEHR}}$, i.e., $\mathcal{X}_{\mathsf{NWMEHR}} \subseteq \mathcal{X}_\Phi$. If $\mathcal{X}_{\mathsf{NWMEHR}}$ is nonempty, then it and $\mathcal{X}_\Phi$ must contain the value of T_f resulting in the globally optimal NWMEHR, which is the solution of Problem 6. Conversely, if $\mathcal{X}_\Phi$ is empty, then $\mathcal{X}_{\mathsf{NWMEHR}}$ is also empty and the optimal strategy is to set $T_f = \infty$ to simply harvest incoherent energy without feedback.

To develop the NWMEHR upper bound $\Phi(T_f)$, we first provide the following Lemma.

Lemma 2. *For all $T \geq T_m$ and all $t > 0$, the $(1,1)$ element of the matrix $\hat{\boldsymbol{S}}(T,t) = \boldsymbol{F}(t)\boldsymbol{S}(T)\boldsymbol{F}^{\mathrm{T}}(t)$ is lower bounded as*

$$\hat{S}_1(T,t) \geq \hat{S}_1^{(0)}(T,t) = t^2\sqrt{AB + \frac{B^2}{12}T^2} \tag{5.25}$$

where $A = 2\omega_F^2\alpha$ and $B = 2\omega_F^2\beta$.

Proof. Please refer to Appendix C.2. □

Recall that the mean beamforming power $\overline{J}(T,t)$ is related to $\hat{S}_1(T,t)$ through (5.21) and (5.3). By providing an explicit lower bound on $\hat{S}_1(T,t)$ (which does not require solving a DARE), we also have a lower bound on the phase variance $\sigma_\phi^2(T,t) = \hat{S}_1(T,t) + Q_1(t)$, and hence an upper bound on $\overline{J}(T,t)$. From this result, we can obtain a simple closed-form and explicit upper bound $\Phi(T_f)$ for the NWMEHR for all $T_f \geq T_m/\mu_{\min}$. The result is summarized in Proposition 3.

Proposition 3. *Define*

$$\theta = \sqrt{\int_0^\infty e^{-2Q_1(t)}\, dt} > 0 \tag{5.26}$$

where $Q_1(t)$ is the $(1,1)$ element of the process noise covariance matrix $\boldsymbol{Q}(t)$. For all $T_f \geq T_m/\mu_{\min}$, we have

$$\begin{aligned}\Phi(T_f) &= 1 + \frac{1}{T_f}\left(\frac{\theta\eta}{\overline{C}}\sum_{j=1}^{N_r}\gamma_j P_{\text{inc}}^{(j)}(\rho_j - 1)\Lambda(\mu_j T_f) - D\right) \\ &\geq \mathsf{NWMEHR}\end{aligned} \tag{5.27}$$

with

$$\Lambda(\mu_j T_f) = \frac{1}{\left(\frac{8}{\pi}\hat{S}_1^{(0)}(\mu_j T_f, 1)\right)^{\frac{1}{4}}} \tag{5.28}$$

where D are defined in (5.8), respectively.

Proof. Please refer to Appendix C.3. □

Note that $\Phi(T_f)$ shares the property with the NWMEHR that $\lim_{T_f\to\infty}\Phi(T_f) = 1$ from below. To see why this is the case in general, note that $\Lambda(\mu_j T_f)$ is a monotonically decreasing function with respect to T_f since $\hat{S}_1^{(0)}(\mu_j T_f, 1)$ is monotonically increasing and $\Phi(T_f)$ is a linear combination of $\Lambda(\mu_j T_f)$ for $j = 1, \cdots, N_r$. Since $\beta > 0$ and $D > 0$, it follows that, for all T_f larger than a threshold T_{ub},

$$\frac{\theta\eta}{\overline{C}}\sum_{j=1}^{N_r}\gamma_j P_{\text{inc}}^{(j)}(\rho_j - 1)\Lambda(\mu_j T_f) < D.$$

Hence, as $T_f \to \infty$, we have $\Phi(T_f) \to 1$ from below.

This result implies that $\mathcal{X}_\Phi$ is either an empty set or a closed bounded interval

$[T_m/\mu_{\min}, T_{ub}]$, where T_{ub} is the solution to

$$\sum_{j=1}^{N_r} \gamma_j P_{\text{inc}}^{(j)} (\rho_j - 1) \Lambda(\mu_j T_{ub}) = \frac{\overline{C} D}{\theta \eta}. \tag{5.29}$$

Note that (5.29) is a one-dimensional equation with respect to T_{ub}, which can be solved easily using any root-finding algorithm like the Brent's method [16]. If no value of $T_{ub} > T_m/\mu_{\min}$ is found, then the optimal strategy is to provide no feedback and to simply harvest incoherent energy. In the following section, we assume $T_{ub} > T_m/\mu_{\min}$ such that $\mathcal{X}_\Phi = [T_m/\mu_{\min}, T_{ub}] \neq \emptyset$ is a bounded interval and develop a method to search the maximum NWMEHR over $\mathcal{X}_\Phi$.

5.4.2 Maximizing the NWMEHR on the Bounded Search Region

Based on the analysis in the prior section, we assume in this section that we have a closed bounded nonempty interval $\mathcal{X}_\Phi = [T_m/\mu_{\min}, T_{ub}]$ for the feasible region of Problem 1. This section describes a method for finding the value of $T_f \in \mathcal{X}_\Phi$ that maximizes the NWMEHR. Since the NWMEHR is an implicit function of T and requires solving a DARE, we rely on numerical methods to efficiently find the optimal solutions.

As a technical detail, recall that $\mathcal{X}_{\mathsf{NWMEHR}} \subseteq \mathcal{X}_\Phi$. If both $\mathcal{X}_{\mathsf{NWMEHR}}$ and $\mathcal{X}_\Phi$ are non-empty, then the procedure described below will find the globally optimal value of T_f which maximizes the NWMEHR. It is possible, however, that $\mathcal{X}_{\mathsf{NWMEHR}}$ is empty even when $\mathcal{X}_\Phi$ is nonempty. When this occurs, the procedure described below will still return the value of $T_f \in \mathcal{X}_\Phi$ that maximizes the NWMEHR, but the resulting NWMEHR will be less than one. If this occurs, we set $T_f = \infty$, which corresponds to no feedback and only incoherent power is harvested, to maximize the

NWMEHR.

There are several potential numerical methods that can be used to solve one-dimensional optimization problems over closed bounded intervals. Most one-dimensional search algorithms, such as line search, golden section search, or parabolic interpolation (Brent's method) [101], can only guarantee convergence to locally optimal solutions. Hence, a prerequisite of applying those algorithms is to show that the NWMEHR can not have more than one local maximum in $\mathcal{X}_\Phi$. This is difficult to show, however, since the objective function of Problem 6 is governed by the DARE in (5.17), which, in general, has no closed-form and explicit expression.

Another approach to solving one-dimensional optimization problems like Problem 6 is to use the DIRECT algorithm [52]. The DIRECT optimization algorithm solves a class of *global* optimization problems over closed bounded intervals. The DIRECT algorithm is especially suitable for solving Problem 6 for the following reasons:

(1) The DIRECT algorithm does not require the knowledge of the gradient of the objective function. Since the objective function of Problem 6 is implicit (requiring a solution of the DARE in (5.17)) and has no closed-form, it is not straightforward to obtain the gradient of the objective function.

(2) Given a bounded domain, the DIRECT algorithm *globally* converges to the maximal value of the objective function, even in the presence of local maxima.

Application of the DIRECT algorithm requires (i) a bounded search region and (ii) the objective function is continuous or at least continuous in the neighborhood of a global optimum [52]. In Section 5.4.1, we bounded the search region of the optimal slot period by $\mathcal{X}_\Phi$. The following proposition establishes that the NWMEHR is a continuous function of T_f on the domain $[T_m/\mu_{\min}, \infty)$ and thus, on $\mathcal{X}_\Phi \subseteq$

$[T_m/\mu_{\min}, \infty)$.

Proposition 4. *The NWMEHR defined in (5.7) is a continuous function with respect to the frame period T_f on the domain $[T_m/\mu_{\min}, \infty)$.*

Proof. Please refer to Appendix C.4. □

In light of Proposition 4, we can apply the DIRECT algorithm straightforwardly on the closed bounded domain $\mathcal{X}_\Phi$. In each iteration, the DIRECT algorithm partitions the search interval into finer sub-intervals by identifying the potentially optimal intervals using a rate-of-change constant, which indicates how much emphasis to place on global versus local search. Once the global part of the algorithm finds the basin of convergence of the optimum, the local part of the algorithm quickly and automatically exploits it [52]. Note that the complexity of the whole procedure is dominated by step 2 since the time required to solve the one-dimensional equation in step 1 is insignificant compared to the time required to solve the iterative DIRECT algorithm in step 2. As mentioned in [52] with regards to the number of iterations for DIRECT, "When a Lipschitz constant is not known, the algorithm stops after a prespecified number of iterations". Hence, in step 2, we use a fixed number of iterations N_i to be the stopping criteria. In each iteration, the maximum number of function evaluations is N_f. For each function evaluation, we need to solve N_d 2×2 DAREs. In general, there would be $N_d = N_t N_r$ 2×2 DAREs to solve in our system. When the oscillator parameters are identical at all of the transmit nodes, it is actually only necessary to solve $N_d = N_r$ 2×2 DAREs due to the common parameters. Thus, in each function evaluation, we need to solve the DARE in (5.17) N_r times by setting $T = \mu_j T_f$ to obtain $\sigma_\phi^2(\mu_j T_f, t)$ for $j = 1, \cdots, N_r$. Each DARE has the same complexity. Therefore, the complexity of the whole procedure scales as $N_i N_f N_t N_r$ or $N_i N_f N_r$ times of the complexity of solving a single 2×2 DARE when

the transmit nodes have differing or identical oscillator parameters, respectively.

The following section presents numerical results based on the NWMEHR-maximizing search strategies developed in this section. The results show that the optimal slot period can be found successfully and efficiently using the proposed algorithms.

5.5 Numerical Results

This section provides numerical results to verify the optimization method described in the previous section and demonstrate the potential of DTB for WPT with practical system parameters. We assume a feedback-based system with frequency division duplexed (FDD) forward and reverse links on separate frequencies. Table 5.1 lists the parameters of the oscillators and other general parameters for both forward and reverse links, where OSS and OLS denote "oscillator short-term stability" and "oscillator long-term stability" parameters, respectively. The process noise parameters p and q in Table 5.1 are chosen based on typical inexpensive crystal oscillator parameters [59] and Rakon RFPO45 oven-controlled oscillator datasheet [2]. Table 5.2 and Table 5.3 list the particular parameters for forward and reverse links, respectively. To apply the DIRECT algorithm, we set the total number of iterations N_i to be 1000 and the maximum number of function evaluations N_f to be 1000 in all our simulations.

While our analysis is general with respect to the receive node energy consumption model, we assume the model from [29] in the numerical results presented in this section. Specifically, the feedback energy used by the j^{th} receive node in a frame is modeled as

$$E_r^{(j)} = \left[\frac{\zeta}{\mu} P_t^{(j)} + P_c\right] T_{on} + P_{tr} T_{tr} \tag{5.30}$$

where μ is the drain efficiency of the RF amplifier, ζ is the Peak to Average Ratio, $P_t^{(j)}$ is the power for feedback transmission, P_c and P_{tr} are the power consumptions of the transmitter circuitry on active and transient mode, respectively, and T_{on} and T_{tr} are the durations of the transmitter circuitry on active and transient mode, respectively. To ensure that the transmit nodes can correctly decode the feedback from receive node j, the transmit power $P_t^{(j)}$ for sending feedback is assumed to be fixed and larger than a minimum decoding threshold $P_{\text{dec}}^{(j)}$. Since the durations of the transmitter circuitry on active and transient mode are much smaller than that of measurement, i.e., $T_{on} \ll T_m$ and $T_{tr} \ll T_m$, we are assuming the feedback to be instantaneous. The power consumption of transmitter circuitry P_c is calculated according to [29], which includes the power consumptions of the mixer, the frequency synthesizer, the digital-to-analog converter and the filters. Figure 5.6 shows the geometry of the network. Both the transmit and receive nodes are equidistantly placed on lines with length 5 meters. Thus, the distance d_{ij} between the i^{th} transmit node and j^{th} receive node can be calculated as $d_{ij} = 10\sqrt{1 + (i/(N_t+1) - j/(N_r+1))^2}$ meters for $i = 1, \cdots, N_t$ and $j = 1, \cdots, N_r$. The weights are assumed to be unit for all receive nodes, i.e., $\gamma_j = 1$ for $j = 1, \cdots, N_r$.

Table 5.1: General parameters.

Case	Parameter	Value	Units	Meaning
good XO	α	2.48×10^{-24}	sec	OSS
	β	7.44×10^{-27}	Hertz	OLS
poor XO	α	6.34×10^{-18}	sec	OSS
	β	2.57×10^{-23}	Hertz	OLS
Rakon	α	2.31×10^{-21}	sec	OSS
RPFO45	β	6.80×10^{-23}	Hertz	OLS
	ϵ	3		path loss exponent
	η	0.70		energy harvesting efficiency

Table 5.2: Parameters for forward link.

Parameter	Value	Units	Meaning
ω_F	$2\pi \times 10^9$	rad/sec	carrier frequency
T_0	50×10^{-6}	sec	duration of measurement for single transmitter
P_0	1	Watts	transmit power per node
L	32		number of bits per channel measurement
G_t	6	dBi	transmitter's antenna gains
R	5×10^{-10}	rad^2	measurement noise

Table 5.3: Parameters for reverse link.

Parameter	Value	Units	Meaning
ω_R	$4.8\pi \times 10^9$	rad/sec	carrier frequency
B_R	10×10^6	Hertz	reverse link bandwidth
R_R	6	Mbps	reverse link data rate
G_r	0	dBi	receiver's antenna gains
P_c	0.1	Watts	circuitry power on active mode
P_{tr}	0.05	Watts	circuitry power on transient mode
T_{tr}	5×10^{-6}	sec	duration on transient mode
ζ	10	dB	Peak to Average Ratio
μ	0.35		drain efficiency of RF amplifier

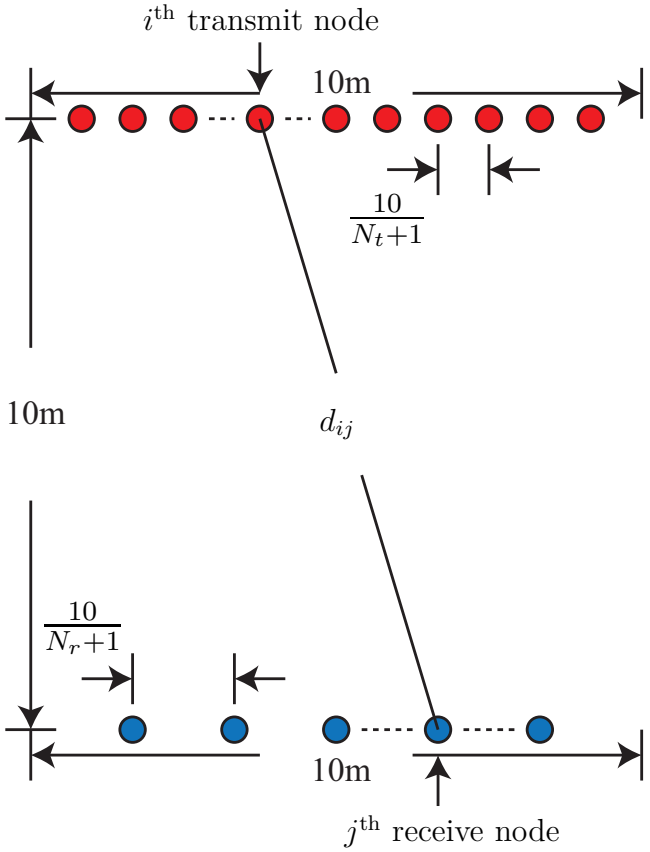

Figure 5.6: Geometry of the network.

Using a link-budget analysis as in [137], we first calculate the minimum decoding threshold. Assuming a thermal noise floor of -174 dBm, we can calculate the power of the additive white Gaussian noise at each transmit node as $-174 + 10\log_{10} B_R = -104$ dBm. We assume the transmitters require 3dB SNR to decode the feedback. Hence, the received signal power at each transmit node should be at least $-104 + 3 = -101$ dBm. The reverse link path loss from the j^{th} receive node to the i^{th} transmit node can be calculated as $10\log_{10}\left(\frac{4\pi d_{ij}\omega_R}{2\pi c}\right)^{\epsilon} = 60.07 + 30\log_{10}(d_{ij})$ dB, where $c = 3\times 10^8$ m/sec is the velocity of light. Thus, the minimum transmit power for the j^{th} receive node sending feedback to the i^{th} transmit node should be $-101 + 60.07 + 30\log_{10}(d_{ij}) - G_r = -40.93 + 30\log_{10}(d_{ij})$ dBm or $8.07\times 10^{-8}(d_{ij})^3$ Watts. Thus, the minimum transmit power for the j^{th} receive node sending feedback is then $P_{\text{dec}}^{(j)} = 8.07\times 10^{-8}(\max_i\{d_{ij}\})^3$ Watts. Since $d_{ij} \le 10\sqrt{2}$ for all i and j, we assume the transmit power for the j^{th} receive node sending feedback is $P_t^{(j)} = 8.07\times 10^{-8}\cdot(10\sqrt{2})^3 = 2.28\times 10^{-4}$ Watts. The time to send feedback to one transmit node is $\frac{L}{R_R} = 5.33\times 10^{-6}$ sec. Hence, the total time to send feedback to all transmit nodes, which is also the duration of the transmitter circuitry on active mode, is $T_{on} = N_t\cdot 5.33\times 10^{-6}$ sec. Based on (5.30), The total energy for feedback from the j^{th} receive node to N_t transmit nodes is

$$E_r^{(j)} = \left(\frac{\zeta}{\mu}P_t^{(j)} + P_c\right)T_{on} + P_{tr}T_{tr} = (N_t\cdot 5.68 + 2.50)\times 10^{-7} \text{ Joules.}$$

To obtain the forward link path loss from the receive nodes to the i^{th} transmit node, we use the forward link carrier frequency ω_F to calculate $|g_{i,j}|^2 = \left(\frac{4\pi d_{ij}\omega_F}{2\pi c}\right)^{-\epsilon}\cdot 10^{\frac{G_t}{10}} = 5.42\times 10^{-5}\,(d_{ij})^{-3}$ for $i = 1,\cdots,N_t$ and $j = 1,\cdots,N_r$.

Figure 5.7 and Figure 5.8 show the optimal frame rate (in Hertz) and the maximum NMEHR versus oscillator parameters α and β for small network ($N_t = 15$

and $N_r = 2$), respectively. Figure 5.9 and Figure 5.10 show the optimal frame rate (in Hertz) and the maximum NMEHR versus oscillator parameters α and β for large network ($N_t = 100$ and $N_r = 50$), respectively. The slot duration factor for each receive node is randomly selected from $(0, 1)$ and normalized to make the summation to be one. It is observed that the optimal frame rate increases when either oscillator parameter α or oscillator parameter β increases. Since in order to achieve the maximum NWMEHR, the system requires the channel information more frequently to compensate for the bad channel estimation caused by the poor oscillator parameters. In all four subplots, we also show dark blue regions in where no feedback is needed. In these areas, the system has low-quality oscillators and thus, the increment of the beamforming power by increasing the frame rate can not compensate for the increment of the energy used for feedback.

Figure 5.11 and Figure 5.12 show the optimal frame rate and the maximum WMEHR versus the numbers of transmit nodes N_t and receive nodes N_r for Rakon RPFO45, respectively. Figure 5.13 and Figure 5.14 show the optimal frame rate and the maximum WMEHR versus the numbers of transmit nodes N_t and receive nodes N_r for good OX, respectively. The WMEHR denotes the weighted mean energy harvested rate, i.e., $\mathsf{WMEHR} = \overline{C} \cdot \mathsf{NWMEHR}$. The slot duration factor for each receive node is equal to be $1/N_r$. It is observed that when N_r is fixed, the optimal frame rate increases when N_t increases. This is caused by the fact that the energy consumption for feedback increases linearly with respect to N_t and thus the receive nodes have to provide more frequent feedback. It is also observed that when N_t is fixed and small ($N_t < 50$), the optimal frame rate is insensitive to N_r and when N_t is large ($N_t > 100$), the optimal frame rate decreases when N_r increases.

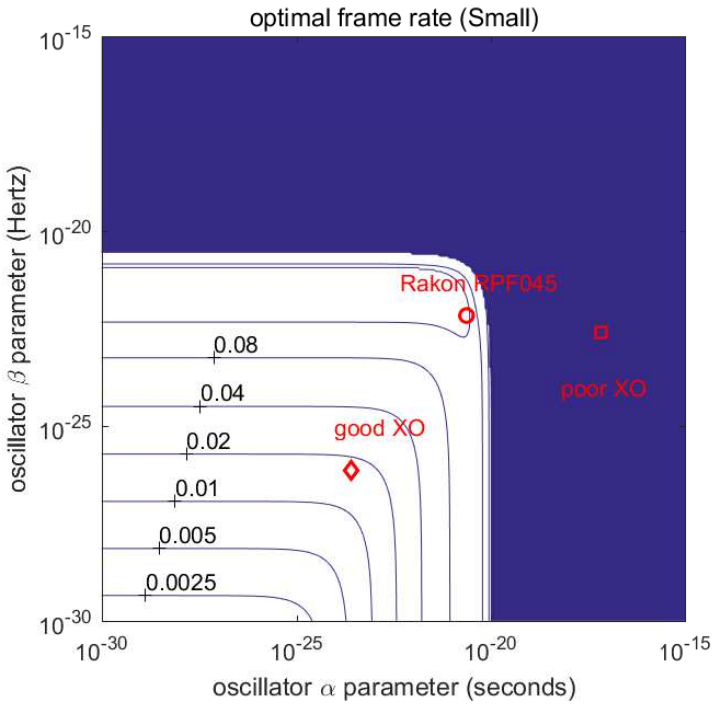

Figure 5.7: Optimal frame rate (in Hertz) versus oscillator parameters α and β for small network ($N_t = 15$ and $N_r = 2$). The shaded region corresponds to conditions under which the optimal strategy is to set the optimal slot rate to zero and harvest incoherent energy.

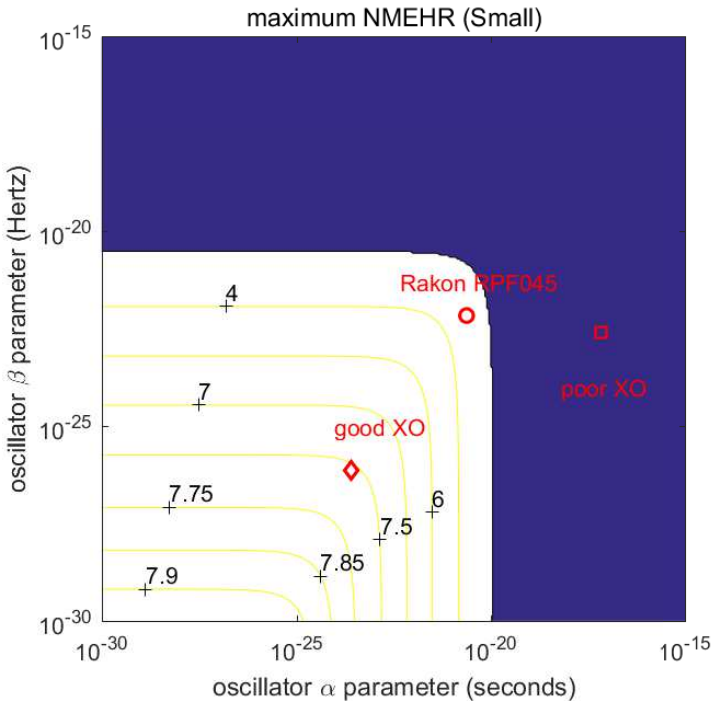

Figure 5.8: Maximum NWMEHR versus oscillator parameters α and β for small network ($N_t = 15$ and $N_r = 2$). The shaded region corresponds to conditions under which the optimal strategy is to set the optimal slot rate to zero and harvest incoherent energy.

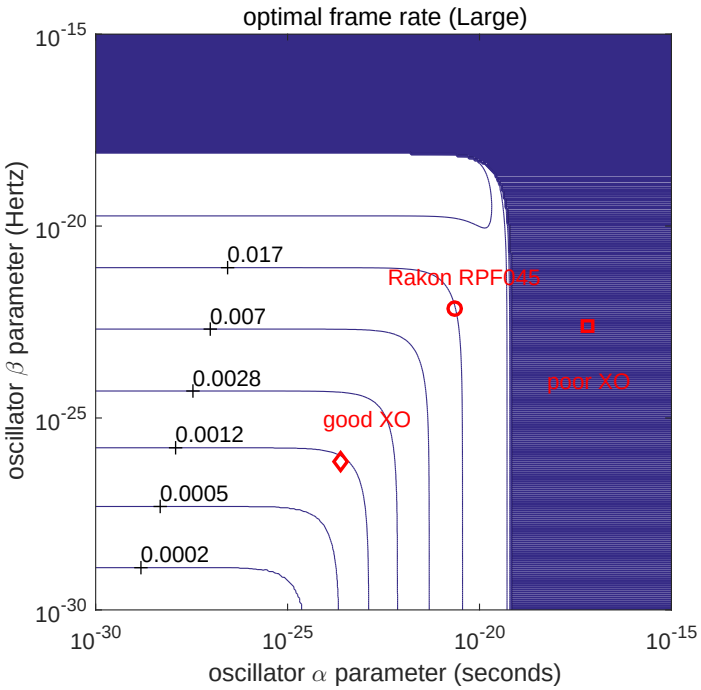

Figure 5.9: Optimal frame rate (in Hertz) versus oscillator parameters α and β for large network ($N_t = 100$ and $N_r = 50$). The shaded region corresponds to conditions under which the optimal strategy is to set the optimal slot rate to zero and harvest incoherent energy.

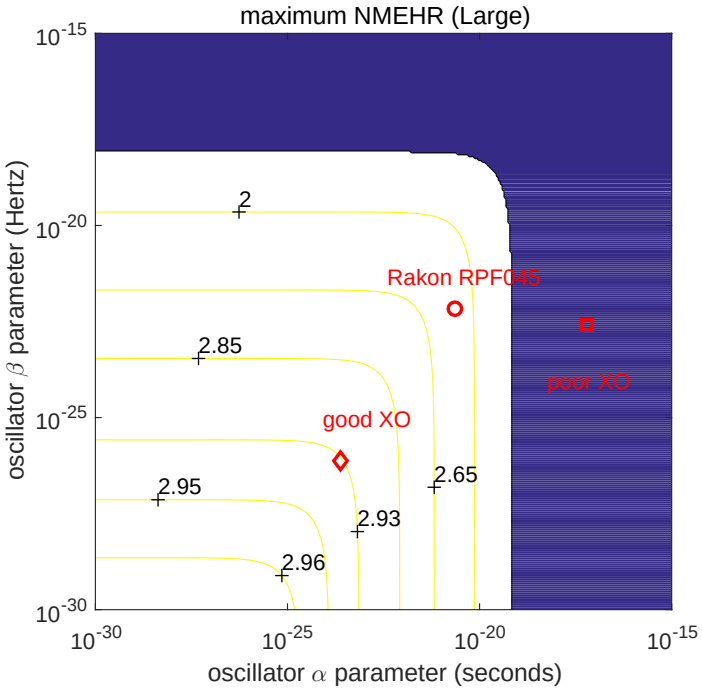

Figure 5.10: Maximum NWMEHR versus oscillator parameters α and β for large network ($N_t = 100$ and $N_r = 50$). The shaded region corresponds to conditions under which the optimal strategy is to set the optimal slot rate to zero and harvest incoherent energy.

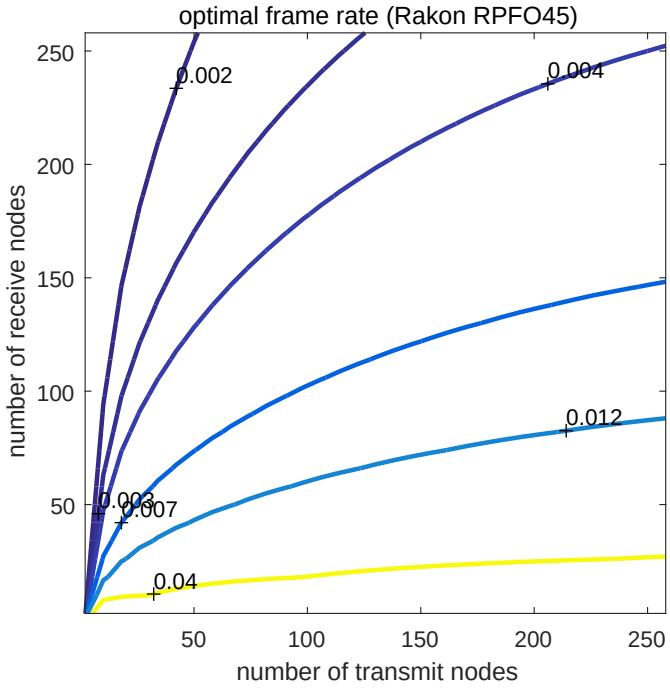

Figure 5.11: Optimal frame rate (in Hertz) versus numbers of transmit nodes N_t and receive nodes N_r for Rakon RPFO45.

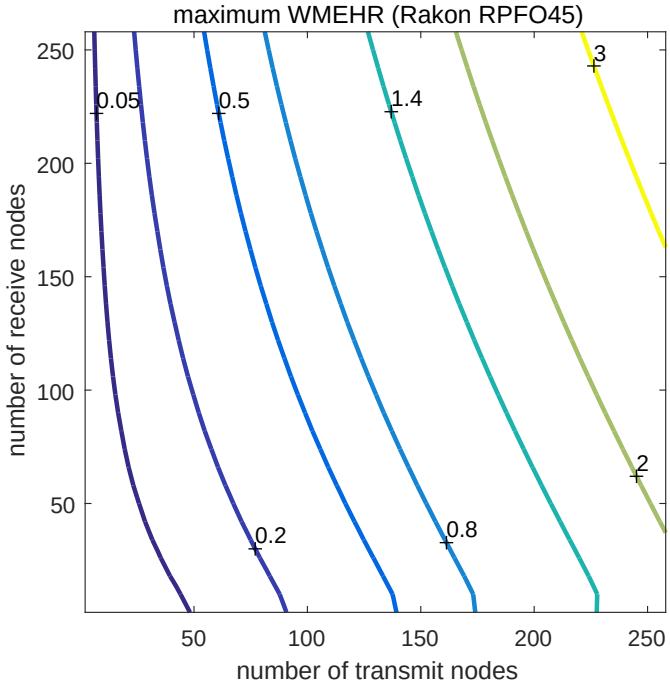

Figure 5.12: Maximum WMEHR (in milliWatts) versus numbers of transmit nodes N_t and receive nodes N_r for Rakon RPFO45.

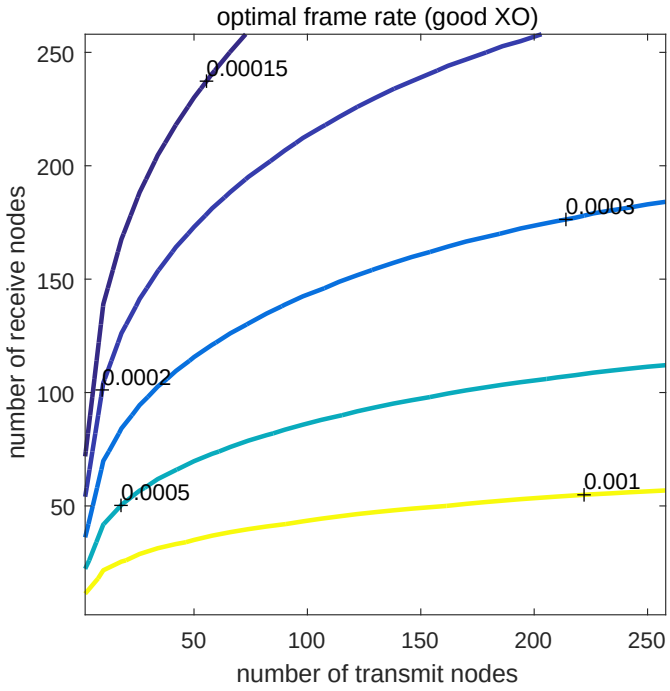

Figure 5.13: Optimal frame rate (in Hertz) versus numbers of transmit nodes N_t and receive nodes N_r for good XO.

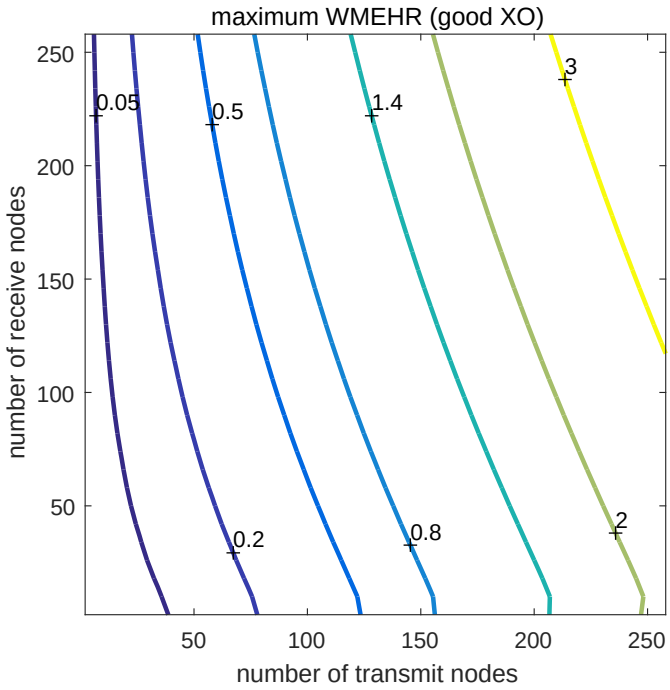

Figure 5.14: Maximum WMEHR (in milliWatts) versus numbers of transmit nodes N_t and receive nodes N_r for good XO.

5.6 Conclusions

This chapter considers the problem of improving the efficiency of wireless power transfer over distance through distributed transmit beamforming. By using a distributed array, the system can achieve good directivity without the use of a large, expensive conventional array. Our system model accounts for the energy of feedback for feedback-based beamforming systems. An optimization problem is formulated to find the optimal feedback period (or feedback rate) to maximize the net energy harvesting rate when local oscillators of the transmit nodes and receive node experience stochastic dynamics. We provide a numerical method to solve the problem by first bounding the search region according to an upper bound function of the NWMEHR and then applying the DIRECT algorithm on that region. Numerical results verify the analysis and demonstrate the potential for using distributed transmit beamforming in wireless power transfer systems.

Chapter 6

Summary and Future Work

In this final chapter the main ideas of this dissertation are summarized and future research directions are identified.

6.1 Summary

In this dissertation, we first discuss the distributed cooperative communication systems, especially the distributed reception and the DTB. In Chapter 2, a distributed reception system with a single distant transmitter and a cluster of multiple receive nodes is discussed. We analyze the outage probability of distributed reception with hard decision exchanges in the case of a binary modulated forward link and independent and identically distributed Rayleigh fading forward link channels. In Chapter 3, we consider the problem of estimating and tracking channels in a distributed MIMO system. To quantify the steady-state performance of a Kalman filter channel tracker, two methods are developed to efficiently compute the steady-state prediction covariance. We then discuss the application of the WPT due to the widely use of battery powered devices in daily life. In Chapter 4, we consider the optimal time and energy allocation to maximize the sum throughput for the case when the nodes

can save energy for later blocks in a time division multiple access scenario where a wireless access point transmits to a group of users which harvest the energy and then use this energy to transmit back to the access point. In Chapter 5, we analyze the optimal feedback period to maximize the weighted mean energy harvesting rate as a function of the oscillator parameters for DTB WPT. We summarize our results by chapter below.

Chapter 2 In this chapter, we considered the problem of jointly decoding binary messages from a single distant transmitter to a cooperative receive cluster, where the nodes in the receive cluster exchange information to decode messages from the transmitter. We compared the outage probability of distributed reception with binary hard decision exchanges with the outage probability of ideal receive beamforming with unquantized observation exchanges. Two simple but surprisingly good approximations show that the outage probability performance of distributed reception with hard decision exchanges is well-predicted by the SNR of ideal receive beamforming after subtracting a hard decision penalty of slightly less than 2 dB. These results, developed in non-asymptotic regimes, are consistent with prior asymptotic results (for a large number of nodes and low per-node SNR) on hard decisions in binary communication systems.

Chapter 3 This chapter considers the problem of estimating and tracking channels in a distributed transmission system with N_t transmit nodes and N_r receive nodes. A linear time-invariant state-space model is developed and is shown to be observable but nonstabilizable. To quantify the steady-state performance of a Kalman filter channel tracker, two methods are developed to efficiently compute the steady-state prediction covariance. The first method requires the solution of a $2(N_t + N_r - 1)$-dimensional discrete-time algebraic Riccati equation, but allows for nonhomogenous oscillator parameters. The second method requires the solution of

four two-dimensional discrete-time algebraic Riccati equations but requires homogenous oscillator parameters for all nodes in the system. An asymptotic analysis is also presented for the homogenous oscillator case for systems with a large number of transmit and receive nodes with closed-from results for all of the elements in the asymptotic prediction covariance as a function of the carrier frequency, oscillator parameters, and channel measurement period.

Chapter 4 In this chapter, we consider WPT system called a "wireless powered communication network" (WPCN), where one hybrid access point (H-AP) with an effectively unlimited power supply coordinates the wireless energy/information transmissions to/from a set of distributed users. Each user is equipped with an energy storage device and thus can harvest and store the wireless energy broadcasted by the H-AP in the downlink. The users transmit their independent information using their individually harvested energy to the H-AP in the uplink. The primary contribution in this chapter is a generalization of the system considered in [54] where the users can save energy harvested in the current block for wireless information transmission (WIT) in later blocks. We consider the problem of maximizing the sum throughput over a finite horizon with energy saving. To maximize the sum throughput over a finite horizon, the initial optimization problem is separated into two sub-problems and finally can be formulated into a standard box-constrained optimization problem, which can be solved efficiently. A tight upper bound is derived by relaxing the energy harvesting causality. Simulation results are also provided to demonstrate the "harvest-then-transmit" protocol with energy saving provides improved sum throughput increasing with the number of transmission blocks.

Chapter 5 This chapter considers the performance of wireless power transfer (WPT) with distributed transmit beamforming (DTB) in a narrowband setting.One or more receive nodes, each equipped with energy harvesting and storage capabil-

ities, provide periodic channel state feedback to a cluster of transmit nodes, each with an independent local oscillator, to facilitate beamforming and passband signal alignment for efficient WPT. Since feedback improves the beamforming gain but requires the receivers to expend energy, there is a fundamental tradeoff between the feedback period and the energy harvesting efficiency. This chapter analyzes the optimal feedback period to maximize the weighted mean energy harvesting rate as a function of the oscillator parameters. An optimization problem is formulated and an explicit method to numerically calculate the globally optimal feedback period is developed.Numerical results verify the analysis and demonstrate the potential for using distributed transmit beamforming in wireless power transfer systems.

6.2 Future Research Directions

Future investigations on distributed communication systems and wireless power transfer could take several directions. The following is a list of possible research topics that can be pursued as an extension of this dissertation:

- In Chapter 2, we conjecture that these approximations actually bound the performance with hard decision exchanges, but are unable to provide a proof. Finding a proof or counterexample is an important direction for future work. Another potentially interesting extension of this work is to extend the analysis to higher-order forward link constellations, e.g., QPSK, 8PSK and 16-QAM.

- In Chapter 5, our focus was on a time slotted DTB protocol where the transmit array steers a beam toward one intended receive node at a time. While the "unintended" receivers still harvest incoherent energy during this time, such an approach may be suboptimal with respect to a DTB protocol where the transmit phases are optimized for simultaneous semi-coherent beamforming to multiple

receivers over the full duration of each frame. We note that the NWMEHR framework developed in this paper can be extended to this scenario by jointly optimizing a $N_t + 1$ dimensional variable containing the transmit phases and feedback rate. Since each transmit phase is naturally bounded on any interval of length 2π, we can use a similar approach as in Section 5.4 to bound the feedback period and hence bound the $N_t + 1$ dimensional optimization variable. Since the new $N_t + 1$ variable is bounded and the objective function is continuous, we can then apply the DIRECT algorithm to find the optimal solution.

Appendix A

Proofs of Propositions in Chapter 3

A.1 Proof of Theorem 4

We first establish the existence and uniqueness of a positive definite $\boldsymbol{\Pi}$ satisfying (3.19) by showing that $[\boldsymbol{A}_1, \boldsymbol{B}_1]$ is completely controllable and $[\boldsymbol{C}_1, \boldsymbol{A}_1]$ is completely observable. The former result follows directly from the construction of the controllable staircase form. The latter result is shown below.

From Lemma 1, we know $[\boldsymbol{H}, \boldsymbol{F}]$ is completely observable. Moreover, since complete observability is invariant to a similarity transform, $[\boldsymbol{H}, \boldsymbol{F}]$ completely observable implies $[\boldsymbol{C}, \boldsymbol{A}]$ is also completely observable. The Popov-Belevitch-Hautus (PBH) test for observability [139] then implies that

$$\operatorname{rank}\left(\begin{bmatrix} \lambda \boldsymbol{I} - \boldsymbol{A} \\ \boldsymbol{C} \end{bmatrix}\right) = \operatorname{rank}(\boldsymbol{A}). \tag{A.1}$$

To establish a contradiction, suppose $[\boldsymbol{C}_1, \boldsymbol{A}_1]$ is not completely observable. The

PBH test then implies that there exists a scalar λ and a nonzero vector $\boldsymbol{z}$ such that

$$\begin{bmatrix} \lambda \boldsymbol{I} - \boldsymbol{A}_1 \\ \boldsymbol{C}_1 \end{bmatrix} \boldsymbol{z} = \boldsymbol{0}.$$

It follows that

$$\begin{bmatrix} \lambda \boldsymbol{I} - \boldsymbol{A}_1 & -\boldsymbol{A}_2 \\ \boldsymbol{0} & \lambda \boldsymbol{I} - \boldsymbol{A}_3 \\ \boldsymbol{C}_1 & \boldsymbol{C}_2 \end{bmatrix} \begin{bmatrix} \boldsymbol{z} \\ \boldsymbol{0} \end{bmatrix} = \boldsymbol{0}.$$

Thus

$$\operatorname{rank}\left(\begin{bmatrix} \lambda \boldsymbol{I} - \boldsymbol{A} \\ \boldsymbol{C} \end{bmatrix} \right) < \operatorname{rank}(\boldsymbol{A})$$

which contradicts (A.1). Hence, $[\boldsymbol{C}_1, \boldsymbol{A}_1]$ is completely observable and, in light of the complete controllability of $[\boldsymbol{A}_1, \boldsymbol{B}_1]$, there exists a unique positive definite $\boldsymbol{\Pi}$ satisfying (3.19). Moreover, this unique positive definite $\boldsymbol{\Pi}$ satisfying (3.19) is stabilizing for $\{\boldsymbol{A}_1, \boldsymbol{B}_1, \boldsymbol{C}_1, \boldsymbol{R}\}$ [24].

Observe that $\boldsymbol{\Pi}$ positive definite implies $\bar{\boldsymbol{\Pi}}$ as defined in (3.18) is positive semidefinite. We now show that $\bar{\boldsymbol{\Pi}}$ as defined in (3.18) satisfies the DARE for $\{\boldsymbol{A}, \boldsymbol{B}, \boldsymbol{C}, \boldsymbol{R}\}$.

This can be seen by writing

$$
\begin{aligned}
&\boldsymbol{A}\left(\bar{\boldsymbol{\Pi}}-\bar{\boldsymbol{\Pi}}\boldsymbol{C}^{\top}\left(\boldsymbol{C}\bar{\boldsymbol{\Pi}}\boldsymbol{C}^{\top}+\boldsymbol{R}\right)^{-1}\boldsymbol{C}\bar{\boldsymbol{\Pi}}\right)\boldsymbol{A}^{\top}+\boldsymbol{B}\boldsymbol{B}^{\top}\\
&=\boldsymbol{A}\left(\bar{\boldsymbol{\Pi}}-\begin{bmatrix}\boldsymbol{\Pi}\boldsymbol{C}_1^{\top}\\ \boldsymbol{0}\end{bmatrix}\left(\boldsymbol{C}_1\boldsymbol{\Pi}\boldsymbol{C}_1^{\top}+\boldsymbol{R}\right)^{-1}\begin{bmatrix}\boldsymbol{\Pi}\boldsymbol{C}_1 & \boldsymbol{0}\end{bmatrix}\right)\boldsymbol{A}^{\top}+\boldsymbol{B}\boldsymbol{B}^{\top}\\
&=\boldsymbol{A}\begin{bmatrix}\boldsymbol{\Pi}-\boldsymbol{\Pi}\boldsymbol{C}_1^{\top}\left(\boldsymbol{C}_1\boldsymbol{\Pi}\boldsymbol{C}_1^{\top}+\boldsymbol{R}\right)^{-1}\boldsymbol{C}_1\boldsymbol{\Pi} & \boldsymbol{0}\\ \boldsymbol{0} & \boldsymbol{0}\end{bmatrix}\boldsymbol{A}^{\top}+\begin{bmatrix}\boldsymbol{B}_1\boldsymbol{B}_1^{\top} & \boldsymbol{0}\\ \boldsymbol{0} & \boldsymbol{0}\end{bmatrix}\\
&=\begin{bmatrix}\boldsymbol{A}_1\left(\boldsymbol{\Pi}-\boldsymbol{\Pi}\boldsymbol{C}_1^{\top}\left(\boldsymbol{C}_1\boldsymbol{\Pi}\boldsymbol{C}_1^{\top}+\boldsymbol{R}\right)^{-1}\boldsymbol{C}_1\boldsymbol{\Pi}\right)\boldsymbol{A}_1^{\top}+\boldsymbol{B}_1\boldsymbol{B}_1^{\top} & \boldsymbol{0}\\ \boldsymbol{0} & \boldsymbol{0}\end{bmatrix}\\
&=\begin{bmatrix}\boldsymbol{\Pi} & \boldsymbol{0}\\ \boldsymbol{0} & \boldsymbol{0}\end{bmatrix}\\
&=\bar{\boldsymbol{\Pi}}.
\end{aligned}
$$

Thus, by construction, $\bar{\boldsymbol{\Pi}}$ is a symmetric positive semidefinite matrix that satisfies the DARE for $\{\boldsymbol{A},\boldsymbol{B},\boldsymbol{C},\boldsymbol{R}\}$. Consequently, $\boldsymbol{P}=\boldsymbol{T}^{-1}\bar{\boldsymbol{\Pi}}\boldsymbol{T}^{-\top}$ is a symmetric positive semidefinite matrix that satisfies (3.14).

Finally, we will show that $\boldsymbol{P}=\boldsymbol{T}^{-1}\bar{\boldsymbol{\Pi}}\boldsymbol{T}^{-\top}$ is a strong solution, and hence is the unique strong solution to (3.14). The eigenvalues of $\boldsymbol{E}$ in (3.15) are invariant to similarity transformation, hence we can write

$$
\begin{aligned}
\boldsymbol{T}\boldsymbol{E}\boldsymbol{T}^{-1}&=\boldsymbol{T}\boldsymbol{F}\boldsymbol{T}^{-1}-\boldsymbol{T}\boldsymbol{F}\boldsymbol{P}\boldsymbol{H}^{\top}(\boldsymbol{H}\boldsymbol{P}\boldsymbol{H}+\boldsymbol{R})^{-1}\boldsymbol{H}\boldsymbol{T}^{-1}\\
&=\boldsymbol{A}-\boldsymbol{A}\bar{\boldsymbol{\Pi}}\boldsymbol{C}^{\top}(\boldsymbol{C}\bar{\boldsymbol{\Pi}}\boldsymbol{C}^{\top}+\boldsymbol{R})^{-1}\boldsymbol{C}\\
&=\begin{bmatrix}\boldsymbol{A}_1-\boldsymbol{A}_1\boldsymbol{\Pi}\boldsymbol{C}_1^{\top}\left(\boldsymbol{C}_1\boldsymbol{\Pi}\boldsymbol{C}_1^{\top}+\boldsymbol{R}\right)^{-1}\boldsymbol{C}_1 & \boldsymbol{X}\\ \boldsymbol{0} & \boldsymbol{A}_3\end{bmatrix}
\end{aligned}
$$

where $\boldsymbol{X}$ is inconsequential to the eigenvalues of $\boldsymbol{E}$. Since $\boldsymbol{\Pi}$ is stabilizing for

$\{\boldsymbol{A}_1, \boldsymbol{B}_1, \boldsymbol{C}_1, \boldsymbol{R}\}$, the eigenvalues of $\boldsymbol{A}_1 - \boldsymbol{A}_1\boldsymbol{\Pi}\boldsymbol{C}_1^\top \left(\boldsymbol{C}_1\boldsymbol{\Pi}\boldsymbol{C}_1^\top + \boldsymbol{R}\right)^{-1}\boldsymbol{C}_1$ must all have magnitude in the open unit disk. The matrix $\boldsymbol{A}_3$ has eigenvalues all equal to one. Hence $\max|\lambda(\boldsymbol{E})| = 1$ and $\boldsymbol{P} = \boldsymbol{T}^{-1}\bar{\boldsymbol{\Pi}}\boldsymbol{T}^{-\top}$ is the unique strong solution to (3.14).

A.2 Proof of Theorem 5

Consider the matrix $\boldsymbol{\Gamma}_n(0,1) = \mathbf{1}_n\mathbf{1}_n^\top$. This matrix has an eigenvalue at zero with algebraic multiplicity $n-1$ and an eigenvalue at n corresponding to the eigenvector $\mathbf{1}_n$. Since $\boldsymbol{\Gamma}_n(0,1)$ is real and symmetric, it is diagonalizable and there exists $\boldsymbol{T}$ such that

$$\boldsymbol{T}^{-1}\boldsymbol{\Gamma}_n(0,1)\boldsymbol{T} = \mathsf{diag}(0,\cdots,0,n). \tag{A.2}$$

Now let $\boldsymbol{T}_s = \boldsymbol{T}\otimes\boldsymbol{I}_s$ and $\boldsymbol{T}_t = \boldsymbol{T}\otimes\boldsymbol{I}_t$. For general $\boldsymbol{A}$ and $\boldsymbol{B}$, both $t\times s$ matrices, we can write

$$\begin{aligned}
\boldsymbol{T}_s^{-1}\boldsymbol{\Gamma}_n(\boldsymbol{A},\boldsymbol{B})\boldsymbol{T}_t &= (\boldsymbol{T}\otimes\boldsymbol{I}_s)^{-1}(\boldsymbol{I}_n\otimes\boldsymbol{A} + \mathbf{1}_n\mathbf{1}_n^\top\otimes\boldsymbol{B})(\boldsymbol{T}\otimes\boldsymbol{I}_t)\\
&= (\boldsymbol{T}^{-1}\otimes\boldsymbol{A} + \boldsymbol{T}^{-1}\mathbf{1}_n\mathbf{1}_n^\top\otimes\boldsymbol{B})(\boldsymbol{T}\otimes\boldsymbol{I}_t)\\
&= \boldsymbol{I}_n\otimes\boldsymbol{A} + (\boldsymbol{T}^{-1}\mathbf{1}_n\mathbf{1}_n^\top\boldsymbol{T})\otimes\boldsymbol{B}\\
&= \boldsymbol{I}_n\otimes\boldsymbol{A} + (\mathsf{diag}(0,\cdots,0,n))\otimes\boldsymbol{B}\\
&= \mathsf{blockdiag}(\boldsymbol{A},\cdots,\boldsymbol{A},\boldsymbol{A}+n\boldsymbol{B})
\end{aligned}$$

where the second to last equality used (A.2).

When $t = s$, the matrices $\boldsymbol{A}$ and $\boldsymbol{B}$ are square and

$$\boldsymbol{T}_s^{-1}\boldsymbol{\Gamma}_n(\boldsymbol{A},\boldsymbol{B})\boldsymbol{T}_t = \mathsf{blockdiag}(\boldsymbol{A},\cdots,\boldsymbol{A},\boldsymbol{A}+n\boldsymbol{B})$$

is a similarity transformation. Now defining,

$$\begin{aligned}
\tilde{\boldsymbol{F}} &:= \boldsymbol{T}_s^{-1}\boldsymbol{F}\boldsymbol{T}_s = \mathsf{blockdiag}(\boldsymbol{F}_0, \cdots, \boldsymbol{F}_0, \boldsymbol{F}_0 + n\boldsymbol{F}_1) \\
\tilde{\boldsymbol{H}} &:= \boldsymbol{T}_t^{-1}\boldsymbol{H}\boldsymbol{T}_s = \mathsf{blockdiag}(\boldsymbol{H}_0, \cdots, \boldsymbol{H}_0, \boldsymbol{H}_0 + n\boldsymbol{H}_1) \\
\tilde{\boldsymbol{R}} &:= \boldsymbol{T}_t^{-1}\boldsymbol{R}\boldsymbol{T}_t = \mathsf{blockdiag}(\boldsymbol{R}_0, \cdots, \boldsymbol{R}_0, \boldsymbol{R}_0 + n\boldsymbol{R}_1) \\
\tilde{\boldsymbol{Q}} &:= \boldsymbol{T}_s^{-1}\boldsymbol{Q}\boldsymbol{T}_s = \mathsf{blockdiag}(\boldsymbol{Q}_0, \cdots, \boldsymbol{Q}_0, \boldsymbol{Q}_0 + n\boldsymbol{Q}_1) \\
\tilde{\boldsymbol{P}} &:= \boldsymbol{T}_s^{-1}\boldsymbol{P}\boldsymbol{T}_s = \mathsf{blockdiag}(\boldsymbol{P}_0, \cdots, \boldsymbol{P}_0, \boldsymbol{P}_0 + n\boldsymbol{P}_1)
\end{aligned}$$

we can apply this similarity transformation to rewrite (3.14) as

$$\tilde{\boldsymbol{P}} = \tilde{\boldsymbol{F}}\left[\tilde{\boldsymbol{P}} - \tilde{\boldsymbol{P}}\tilde{\boldsymbol{H}}^\top(\tilde{\boldsymbol{H}}\tilde{\boldsymbol{P}}\tilde{\boldsymbol{H}}^\top + \tilde{\boldsymbol{R}})^{-1}\tilde{\boldsymbol{H}}\tilde{\boldsymbol{P}}\right]\tilde{\boldsymbol{F}}^\top + \tilde{\boldsymbol{Q}}. \tag{A.3}$$

Since $[\boldsymbol{H}, \boldsymbol{F}]$ is completely observable, it is also detectable. Moreover, since detectability is invariant to a similarity transform, $[\boldsymbol{H}, \boldsymbol{F}]$ detectable implies $[\tilde{\boldsymbol{H}}, \tilde{\boldsymbol{F}}]$ is detectable. Hence there exists a unique strong solution $\tilde{\boldsymbol{P}}$ to (A.3) as shown in [24, Theorem 3.1].

Due to the block diagonal nature all of the matrices in (A.3), the transformed system can be viewed as n uncoupled systems, each with s states. Observe that $n-1$ of these systems have identical dynamics. Hence, there are only two distinct $s \times s$ DAREs to solve. The first DARE is given as

$$\boldsymbol{P}_0 = \boldsymbol{F}_0\Big[\boldsymbol{P}_0 - \boldsymbol{P}_0\boldsymbol{H}_0^\top(\boldsymbol{H}_0\boldsymbol{P}_0\boldsymbol{H}_0^\top + \boldsymbol{R}_0)^{-1}\boldsymbol{H}_0\boldsymbol{P}_0\Big]\boldsymbol{F}_0^\top + \boldsymbol{Q}_0.$$

Denoting $\bar{\boldsymbol{P}} = \boldsymbol{P}_0 + n\boldsymbol{P}_1$ and using similar notation for the other relevant matrices,

the second DARE can be written as

$$\bar{\boldsymbol{P}} = \bar{\boldsymbol{F}} \left[\bar{\boldsymbol{P}} - \bar{\boldsymbol{P}} \bar{\boldsymbol{H}}^\top (\bar{\boldsymbol{H}} \bar{\boldsymbol{P}} \bar{\boldsymbol{H}}^\top + \bar{\boldsymbol{R}})^{-1} \bar{\boldsymbol{H}} \bar{\boldsymbol{P}} \right] \bar{\boldsymbol{F}}^\top + \bar{\boldsymbol{Q}}.$$

Finally, note that both $\boldsymbol{P}_0$ and $\bar{\boldsymbol{P}}$ must be strong since $\tilde{\boldsymbol{P}} = \mathsf{blockdiag}(\boldsymbol{P}_0, \cdots, \boldsymbol{P}_0, \bar{\boldsymbol{P}})$ is strong if and only if $\boldsymbol{P}_0$ and $\bar{\boldsymbol{P}}$ are both strong.

Appendix B

Proofs of Propositions in Chapter 4

B.1 Proof of Proposition 1

Assume there exist optimal allocation $\boldsymbol{\tau}^*$ such that

$$\sum_{i=0}^{K} \tau_i^{(\ell_0)*} < 1$$

where $\ell_0 \in \{1, \cdots, L\}$. We can increase one $\tau_i^{(\ell_0)*}$ to make the summation to be 1. If we use $(\boldsymbol{\tau}_0^*, \boldsymbol{\tau}^*, \boldsymbol{\alpha}^*)$ and $(\tilde{\boldsymbol{\tau}}_0^*, \tilde{\boldsymbol{\tau}}^*, \boldsymbol{\alpha}^*)$ to denote the optimal solutions of **P1** and the new solution respectively, we can obtain

$$R(\boldsymbol{\tau}_0^*, \boldsymbol{\tau}^*, \boldsymbol{\alpha}^*) < R(\tilde{\boldsymbol{\tau}}_0^*, \tilde{\boldsymbol{\tau}}^*, \boldsymbol{\alpha}^*)$$

since $R(\boldsymbol{\tau}_0, \boldsymbol{\tau}, \boldsymbol{\alpha})$ is a monotonically increasing function with respect to $\tau_i^{(\ell)}$ for all indices i and ℓ, which is a contradiction to the optimality of the solutions $(\boldsymbol{\tau}_0^*, \boldsymbol{\tau}^*, \boldsymbol{\alpha}^*)$. This completes the proof of Proposition 1.

B.2 Proof of Proposition 2

First, we show that the objective function of **P3** is a concave function with respect to $(\boldsymbol{\tau}_0, \boldsymbol{\tau})$. Denote the Hessian of $R_i^{(\ell)}$ as

$$\mathcal{H}_i^{(\ell)} = \left[d_{m,n}^{(i,\ell)}\right], 0 \leq m, n \leq (K+1)L$$

where $d_{m,n}^{(i,\ell)}$ denotes the element of $\mathcal{H}_i^{(\ell)}$ at mth row and nth column. From (4.10), we can obtain the diagonal element of $\mathcal{H}_i^{(\ell)}$ as

$$d_{m,n}^{(i,\ell)} = \begin{cases} -\frac{1}{\ln 2} \frac{\tau_i^{(\ell)} \phi_{i,j}^{(\ell)2}}{\left(\tau_i^{(\ell)} + t_i^{(\ell)}\right)^2}, & m = n = O(0,j) \\ -\frac{1}{\ln 2} \frac{t_i^{(\ell)}}{\left(\tau_i^{(\ell)} + t_i^{(\ell)}\right)^2}, & m = n = O(i,\ell) \\ 0, & \text{otherwise} \end{cases} \tag{B.1}$$

The off-diagonal elements can be expressed as

$$d_{m,n}^{(i,\ell)} = d_{n,m}^{(i,\ell)} = \begin{cases} \frac{1}{\ln 2} \frac{t_i^{(\ell)} \phi_{i,j}^{(\ell)}}{\left(\tau_i^{(\ell)} + t_i^{(\ell)}\right)^2}, & m = O(i,\ell), n = O(0,j) \\ -\frac{1}{\ln 2} \frac{\tau_i^{(\ell)} \phi_{i,j}^{(\ell)} \phi_{i,k}^{(\ell)}}{\left(\tau_i^{(\ell)} + t_i^{(\ell)}\right)^2}, & m = O(0,j), n = O(0,k) \\ 0, & \text{otherwise} \end{cases} \tag{B.2}$$

for $1 \leq j, k \leq \ell, \forall i \in I, \forall \ell \in J$, where $t_i^{(\ell)} := \sum_{j=1}^{\ell} \phi_{i,j}^{(\ell)} \tau_0^{(j)}$ and $O(i,j) := (j-1)(K+1) + i + 1$. Given an arbitrary real vector $\boldsymbol{v} = [\boldsymbol{v}^{(1)\mathrm{T}}, \cdots, \boldsymbol{v}^{(L)\mathrm{T}}]^{\mathrm{T}}$, where $\boldsymbol{v}^{(\ell)} = [v_0^{(\ell)}, v_1^{(\ell)}, \cdots, v_K^{(\ell)}]^{\mathrm{T}}, \forall \ell \in J$, it can be shown from (B.1) and (B.2) that

$$\boldsymbol{v}^{\mathrm{T}} \mathcal{H}_i^{(\ell)} \boldsymbol{v} = -\frac{1}{\ln 2} \frac{1}{\left(\tau_i^{(\ell)} + t_i^{(\ell)}\right)^2 \tau_i^{(\ell)}} \left(\sum_{j=1}^{\ell} \phi_{i,j}^{(\ell)} \tau_i^{(\ell)} v_0^{(j)} - t_i^{(\ell)} v_i^{(\ell)} \right)^2 \leq 0$$

It follows that $\mathcal{H}_i^{(\ell)}$ is a negative semidefinite matrix. Thus, $R_i^{(\ell)}$ is a concave function with respect to $(\boldsymbol{\tau}_0, \boldsymbol{\tau})$. Further, $R(\boldsymbol{\tau}_0, \boldsymbol{\tau}, \boldsymbol{\alpha})$ is a concave function with respect to $(\boldsymbol{\tau}_0, \boldsymbol{\tau})$ when $\boldsymbol{\alpha}$ is fixed since it is a summation of such concave functions. From **P3**, it is noticed that the functions of the inequality constraints are convex and the functions of the equality constraints are affine. This implies that **P3** is a standard convex optimization problem, which completes the proof of Proposition 2.

B.3 Proofs of Theorem 1

From (4.13), we notice that $\tau_i^{(\ell)\star} = 0$ implies $\sum_{j=1}^{\ell} \phi_{i,j}^{(\ell)} \tau_0^{(j)\star} = 0$. We define the following set

$$\mathcal{X}^{(\ell)} = \{i \in \mathcal{I} : \tau_i^{(\ell)\star} \neq 0\}, \forall \ell \in \mathcal{J}$$

From the complementary slackness property, we know

$$\lambda_i^{(\ell)\star} = 0, \forall i \in \mathcal{X}^{(\ell)}$$

From (4.12), we notice that this implies

$$C_i^{(\ell)\star} = C_j^{(\ell)\star}, \forall i, j \in \mathcal{X}^{(\ell)} \tag{B.3}$$

From (B.3) and the relations $\sum_{i \in \mathcal{X}^{(\ell)}} \tau_i^{(\ell)\star} = 1 - \tau_0^{(\ell)\star}, \forall \ell \in \mathcal{J}$, it follows

$$\tau_i^{(\ell)\star} = \frac{\left(1 - \tau_0^{(\ell)\star}\right) \sum_{j=1}^{\ell} \phi_{i,j}^{(\ell)} \tau_0^{(j)\star}}{\sum_{i \in \mathcal{X}^{(\ell)}} \sum_{j=1}^{\ell} \phi_{i,j}^{(\ell)} \tau_0^{(j)\star}}, \ i \in \mathcal{X}^{(\ell)}, \forall \ell \in \mathcal{J} \tag{B.4}$$

We notice that the case $\tau_i^{(\ell)\star} = 0$ can also be written as the form in (B.4). Hence, after combining these two cases, we obtain uniform relations

$$\tau_i^{(\ell)\star} = \frac{\left(1 - \tau_0^{(\ell)\star}\right) \sum_{j=1}^{\ell} \phi_{i,j}^{(\ell)} \tau_0^{(j)\star}}{\sum_{i=1}^{K} \sum_{j=1}^{\ell} \phi_{i,j}^{(\ell)} \tau_0^{(j)\star}}, \forall i \in \mathcal{I}, \forall \ell \in \mathcal{J} \tag{B.5}$$

This completes the proof of Theorem 1.

B.4 Proof of Theorem 2

The Lagrange function of **P5** is

$$\mathcal{L}\left(\boldsymbol{\tau}_0, \tilde{\boldsymbol{F}}\right) = \sum_{\ell=1}^{L} \left(1 - \tau_0^{(\ell)}\right) \log_2 \left(1 + \frac{\tilde{F}^{(\ell)}}{1 - \tau_0^{(\ell)}}\right) - \lambda \left(\sum_{\ell=1}^{L} \tilde{F}^{(\ell)} - \sum_{\ell=1}^{L} \sum_{i=1}^{K} \gamma_i^{(\ell)} E_i^{(\ell)}\right)$$

and differentiating with respect to $\tilde{F}^{(\ell)}$, we can obtain

$$\frac{1 - \tau_0^{(\ell)}}{1 - \tau_0^{(\ell)} + \tilde{F}^{(\ell)}} = \pi$$

Since $\tilde{F}^{(\ell)}$ must be nonnegative, using KKT conditions, we can verify the optimal solution of $\tilde{\boldsymbol{F}}$ when fixing $\boldsymbol{\tau}_0$ is

$$\tilde{F}^{(\ell)} = \left[\frac{1 - \tau_0^{(\ell)}}{\pi^\star} - (1 - \tau_0^{(\ell)})\right]^+, \forall \ell \in \mathcal{J}$$

where $\pi^\star \in \mathbb{R}$ is selected to satisfy

$$\sum_{\ell=1}^{L} \tilde{F}^{(\ell)} = \sum_{\ell=1}^{L} \sum_{i=1}^{K} \gamma_i^{(\ell)} E_i^{(\ell)}.$$

Here $(x)^+$ denotes the positive part of x:

$$(x)^+ = \begin{cases} x & \text{if } x \geq 0 \\ 0 & \text{if } x < 0 \end{cases}$$

This completes the proof of Theorem 2.

Appendix C

Proofs of Propositions in Chapter 5

C.1 Proof of Lemma 1.

To show the NWMEHR converges to 1 from below when $T_f \to \infty$, we show $\int_{T_m}^{T} e^{-\sigma_\phi^2(T,t)}\, dt \to 0$ when $T \to \infty$. From (5.21), we have

$$\int_{T_m}^{T} e^{-\sigma_\phi^2(T,t)}\, dt \leq \sqrt{\int_0^\infty e^{-2\hat{S}_1(T,t)}\, dt} \times \sqrt{\int_0^\infty e^{-2Q_1(t)}\, dt} \tag{C.1}$$

where the equality comes from the Cauchy-Schwarz inequality and results from the nonnegativity of $e^{-2\hat{S}_1(T,t)}$ and $e^{-2Q_1(t)}$ and $[T_m, T] \subseteq [0, \infty)$. Since $\sqrt{\int_0^\infty e^{-2Q_1(t)}\, dt}$ is bounded, thus, it suffices to show $\lim_{T\to\infty} \int_0^\infty e^{-2\hat{S}_1(T,t)}\, dt = 0$. According to (5.20), it follows

$$\lim_{T\to\infty} \int_0^\infty e^{-2\hat{S}_1(T,t)}\, dt \leq \lim_{T\to\infty} \int_0^1 e^{-t^2 S_3(T)}\, dt + \lim_{T\to\infty} \int_1^\infty e^{-t^2 S_3(T)}\, dt \tag{C.2}$$

where the equality results from the nonnegativity of $S_1(T)$, $tS_2(T)$ for any $T \in [T_m, \infty)$ and $t \geq 0$. For the first term of the right-hand side (RHS) of (C.2), it follows

$$\lim_{T\to\infty} \int_0^1 e^{-t^2 S_3(T)}\, dt = \int_0^1 \lim_{T\to\infty} e^{-t^2 S_3(T)}\, dt = 0 \tag{C.3}$$

from the Lebesgue's dominated convergence theorem and $\lim_{T\to\infty} S_3(T) = \infty$ since $S_3(T)$ is the Kalman filter steady-state estimation variance of the frequency. For the second term of the RHS of (C.2), it follows

$$\lim_{T\to\infty} \int_1^\infty e^{-t^2 S_3(T)}\, dt \overset{(a)}{\leq} \lim_{T\to\infty} \frac{1}{S_3(T)} e^{-S_3(T)} \overset{(b)}{=} 0 \tag{C.4}$$

, where (a) results from $e^{-t^2 S_3(T)} \leq e^{-tS_3(T)}$ for all $t \in [1, \infty)$ with fixed T and (b) comes from the fact $\lim_{T\to\infty} S_3(T) = \infty$.

If the NWMEHR attains its maximum at infinity, then we know

$$\sup_{T_f \in [T_m/\mu_{\min}, \infty)} \mathsf{NWMEHR} = 1 \tag{C.5}$$

from prior analysis. Otherwise, the NWMEHR attains its maximum in the interval $(T_m/\mu_{\min}, \infty)$, which implies $\sup_{T_f \in [T_m/\mu_{\min}, \infty)} \mathsf{NWMEHR} \geq 1$. Hence,

$$\sup_{T_f \in [T_m/\mu_{\min}, \infty)} \mathsf{NWMEHR} \geq 1 \tag{C.6}$$

. On the other hand, if we denote $\mu_{\max} = \max\{\mu_1, \cdots, \mu_{N_r}\}$, from (5.7), it follows

$$\mathsf{NWMEHR} \leq 1 + \frac{\eta}{\overline{C}} \sum_{j=1}^{N_r} \gamma_j P_{\text{inc}}^{(j)} (\rho_j - 1)\mu_{\max} = 1 + (\overline{\rho} - 1)\mu_{\max} \tag{C.7}$$

, where $\overline{\rho}$ is defined in (5.22). This completes the proof of Lemma 1.

C.2 Proof of Lemma 2

The proof mainly involves two steps. **Step 1** shows $\hat{S}_1(T,t)$ is a monotonically increasing function of $R \in (0,\infty)$ for fixed $T \geq T_m$ and $t > 0$. **Step 2** shows that $\hat{S}_1(T,t) \to \hat{S}_1^{(0)}(T,t) = t^2\sqrt{AB + \frac{B^2}{12}T^2}$ when $R \to 0$.

Step 1: From (5.20), it suffices to prove that each element of $\boldsymbol{S}(T)$ is a monotonically increasing function of $R \in (0,\infty)$ for fixed $T \geq T_m$. If $R > 0$, then from the DARE in (5.17), it follows

$$\frac{S_1(T)R}{R-S_1(T)} = S_1(T)+2TS_2(T)+T^2S_3(T)+Q_1(T) \tag{C.8}$$

$$\frac{S_2(T)R}{R-S_1(T)} = S_2(T)+TS_3(T)+Q_2(T) \tag{C.9}$$

$$\frac{S_2^2(T)}{R-S_1(T)} = Q_3(T) \tag{C.10}$$

We then prove the monotonicity of $S_1(T)$, $S_2(T)$ and $S_3(T)$ with respect to R over $(0,\infty)$ one by one using contradictions. We first assume that $S_1(T)$ will decrease when R increases for some $R > 0$. From (C.10), we know that $S_2(T)$ will increase. From (C.8), it follows

$$S_3(T) = \frac{1}{T^2}\left(\frac{S_1^2(T)}{R-S_1(T)} - 2TS_2(T) - Q_1(T)\right). \tag{C.11}$$

Hence, $S_3(T)$ will decrease. From (C.8) and (C.9), we can obtain

$$S_3(T) = \frac{2TS_2^2(T)+S_2(T)Q_1(T)-S_1(T)Q_2(T)}{T(S_1(T)-TS_2(T))}. \tag{C.12}$$

It is noticed that the right-hand side (RHS) of (C.12) will increase, which implies that $S_3(T)$ will increase. This gives us a contradiction. Hence, we know $S_1(T)$ is a monotonically increasing function of $R > 0$. Next, we assume that $S_2(T)$ will

decrease at some point $R > 0$. From (C.10), we know that $R - S_1(T)$ will decrease. Then, from (C.11), it follows that $S_3(T)$ will increase. However, the RHS of (C.12) will decrease, which is a contradiction. Hence, $S_2(T)$ is a monotonically increasing function of $R > 0$. Finally, we assume $S_3(T)$ will decrease at some point $R > 0$. From (C.9) and (C.10), we have $\frac{S_1(T)}{S_2(T)} = \frac{TS_3(T)+Q_2(T)}{Q_3(T)}$ which implies that $\frac{S_1(T)}{S_2(T)}$ will decrease. From (C.8) and (C.9), we have $\frac{S_1(T)}{S_2(T)} = \frac{2TS_2(T)}{TS_3(T)+Q_2(T)} + \frac{Q_1(T)-Q_2(T)T}{TS_3(T)+Q_2(T)} + T$. Note that both the first term and the second term will increase and thus $\frac{S_1(T)}{S_2(T)}$ will increase, which is a contradiction, thus, $S_3(T)$ is a monotonically increasing function of R.

Step 2: From the DARE in (5.17), we can obtain a polynomial of $P_1(T)$ for fixed T as

$$\begin{aligned} &P_1^4(T) - (2U(T) + V(T))P_1^3(T) \\ &+ (U^2(T) - 2RU(T) - 5RV(T))P_1^2(T) \\ &+ (2RU^2(T) - 8R^2V(T))P_1(T) \\ &+ (R^2U^2(T) - 4R^3V(T)) = 0 \end{aligned} \tag{C.13}$$

where $U(T) = Q_1(T) - TQ_2(T)$ and $V(T) = T^2Q_3(T)$. Note that (C.13) is quartic in $P_1(T)$ for fixed T, it has four explicit solutions [3]. The *largest real* one is the (1,1) element of $\boldsymbol{P}(T)$, which is the unique solution of the DARE (5.17). To see this, we first use $P_1(T)$ to represent $P_2(T)$ and $P_3(T)$ as

$$P_2(T) = \sqrt{(P_1(T) + R)Q_3(T)} \tag{C.14}$$

$$P_3(T) = \frac{1}{T}\left(\frac{\sqrt{Q_3(T)}P_1(T)}{\sqrt{P_1(T) + R}} - Q_2(T)\right) + Q_3(T) \tag{C.15}$$

Hence, the determinant of $\boldsymbol{P}(T)$ is

$$|\boldsymbol{P}(T)| = \frac{P_1(T)}{T}\left(\frac{\sqrt{Q_3(T)}P_1(T)}{\sqrt{P_1(T)+R}} - Q_2(T)\right) - RQ_3(T). \tag{C.16}$$

It is noticed that $|\boldsymbol{P}(T)|$ is a monotonically increasing function of $P_1(T)$. Evidently, $P_1(T)$ should be real. If $P_1(T)$ is not the largest one among all the real solutions of (C.13) for fixed $T \geq T_m$, we then know that $\boldsymbol{P}(T)$ with $P_1(T)$ to be the largest real solution and $P_2(T)$ and $P_3(T)$ calculated by using (C.14) and (C.15), respectively, is also a positive definite solution of the DARE (5.17), which is a contradiction of the uniqueness of the solution. If $R = 0$, then from the DARE in (5.17), we can obtain a quadratic equation of $P_1(T)$. To distinguish the solution from that of $R > 0$, we use $P_1^{(0)}(T)$ to represent it. Among the two solutions of the quadratic equation, we choose $P_1^{(0)}(T) = \frac{(2U(T)+V(T))+\sqrt{4U(T)V(T)+V^2(T)}}{2}$ and discard the other one since we need $S_1^{(0)}(T) = P_1^{(0)}(T) - Q_1(T) > 0$. Recall that $P_1(T)$ is the largest real one of the four solutions of the quartic equation (C.13) for fixed $T \geq T_m$. If we allow R goes to zero in (C.13), then $P_1(T) \to P_1^{(0)}(T)$. From (5.19), (C.14) and (C.15), it follows $S_1(T) \to 0$, $S_2(T) \to 0$ and $S_3(T) \to \sqrt{AB + \frac{B^2}{12}T^2}$ when $R \to 0$. Therefore, $\hat{S}_1(T,t) \to \hat{S}_1^{(0)}(T,t) = t^2\sqrt{AB + \frac{B^2}{12}T^2}$ according to (5.20).

Combining **step 1** and **step 2**, it follows $\hat{S}_1(T,t) \geq \hat{S}_1^{(0)}(T,t)$ for any fixed $T \geq T_m$ and $t > 0$. This completes the proof of Lemma 2.

C.3 Proof of Proposition 3

If we define $\theta = \sqrt{\int_{t=0}^{\infty} e^{-2Q_1(t)}\,dt}$ and from (C.1), it follows

$$\int_{T_m}^{T} e^{-\sigma_\phi^2(T,t)}\,dt \leq \theta\sqrt{\int_0^{\infty} e^{-2\hat{S}_1^{(0)}(T,t)}\,dt} \tag{C.17}$$

for all $T \in [T_m, \infty)$, where we use $\hat{S}_1(T,t) \geq \hat{S}_1^{(0)}(T,t)$ for any fixed $T \geq T_m$ and $t > 0$ from Lemma 2. We then substitute the expression of $\hat{S}_1^{(0)}(T,t)$ given in (5.25) into (C.17), it follows

$$\int_{T_m}^{T} e^{-\sigma_\phi^2(T,t)}\, dt \leq \frac{\theta}{\left(\frac{8}{\pi}\hat{S}_1^{(0)}(T,1)\right)^{\frac{1}{4}}} = \Lambda(T). \tag{C.18}$$

After plugging (C.18) into (5.7), we can obtain the expression of $\Phi(T_f)$ in (5.27).

C.4 Proof of Proposition 4

From (5.7), it suffices to show $\sigma_\phi^2(\mu_j T_f, t)$ is a continuous function of $T_f \in [T_m/\mu_{\min}, \infty)$ for any j and $t > 0$. In fact, we can show $\sigma_\phi^2(T,t)$ is a continuous function of $T > 0$ for any $t > 0$. From (5.20) and (5.21), it suffices to show each element of $\boldsymbol{S}(T)$ is a continuous function of $T > 0$. It then suffices to show that each element of $\boldsymbol{P}(T)$ is a continuous function of $T > 0$ according to (5.19) since each element of $\boldsymbol{S}(T)$ is a composition of continuous functions with respect to the elements of $\boldsymbol{P}(T)$. We give T a perturbation ΔT such that $T + \Delta T \in [T_m, \infty)$ and denote $\tilde{\boldsymbol{P}}(T)$ to be a symmetric solution of the following perturbed DARE:

$$\tilde{\boldsymbol{P}}(T) = \boldsymbol{F}(T+\Delta T)\left[\tilde{\boldsymbol{P}}(T) - \frac{\tilde{\boldsymbol{P}}(T)\boldsymbol{h}^{\mathrm{T}}\boldsymbol{h}\tilde{\boldsymbol{P}}(T)}{\boldsymbol{h}\tilde{\boldsymbol{P}}(T)\boldsymbol{h}^{\mathrm{T}} + R}\right]\boldsymbol{F}(T+\Delta T)^{\mathrm{T}} + \boldsymbol{Q}(T+\Delta T). \tag{C.19}$$

From Theorem 3.1 in [122], we have $||\tilde{\boldsymbol{P}}(T) - \boldsymbol{P}(T)||_F = O(\delta_{\boldsymbol{F},\boldsymbol{Q}})$ for $\delta_{\boldsymbol{F},\boldsymbol{Q}} \to 0$, where $\delta_{\boldsymbol{F},\boldsymbol{Q}} = (\|\Delta\boldsymbol{F}\|_F^2 + \|\Delta\boldsymbol{Q}\|_F^2)^{1/2}$ with $\Delta\boldsymbol{F} = \boldsymbol{F}(T+\Delta T) - \boldsymbol{F}(T)$ and $\Delta\boldsymbol{Q} = \boldsymbol{Q}(T + \Delta T) - \boldsymbol{Q}(T)$. When $\Delta T \to 0$, it follows $\delta_{\boldsymbol{F},\boldsymbol{Q}} \to 0$ since each element of either $\boldsymbol{F}(T)$ or $\boldsymbol{Q}(T)$ is a continuous function with respect to $T > 0$. Therefore, $\lim_{\Delta T \to 0} ||\tilde{\boldsymbol{P}}(T) - \boldsymbol{P}(T)||_F = 0$, which implies that each element of $\boldsymbol{P}(T)$ is a continuous function with respect to $T > 0$. This completes the proof of Proposition 4.

Bibliography

[1] Tutorial overview of inductively coupled RFID systems, 2003.

[2] Rakon RFPO45 crystal oscillator datasheet, 2009.

[3] Milton Abramowitz. *Handbook of Mathematical Functions, With Formulas, Graphs, and Mathematical Tables,*. Dover Publications, Incorporated, 1974.

[4] H. Abubakari and S. Sastry. Ieee 1588 style synchronization over wireless link. In *Precision Clock Synchronization for Measurement, Control and Communication, 2008. ISPCS 2008. IEEE International Symposium on*, pages 127–130, Sept 2008.

[5] E. Aktas, J. Evans, and S. Hanly. Distributed decoding in a cellular multiple-access channel. *Wireless Communications, IEEE Transactions on*, 7(1):241 –250, Janurary 2008.

[6] B.D.O. Anderson. Stability properties of kalman-bucy filters. *Journal of the Franklin Institute*, 291(2):137 – 144, 1971.

[7] B.D.O. Anderson and J.B. Moore. *Optimal Filtering*. Dover, 1979.

[8] L.F. Auler and R. d'Amore. Adaptive kalman filter for time synchronization over packet-switched networks: An heuristic approach. In *Communication Systems Software and Middleware, 2007. COMSWARE 2007. 2nd International Conference on*, pages 1–7, Jan 2007.

[9] A. Avudainayagam, J.M. Shea, T.F. Wong, and Xin Li. Reliability exchange schemes for iterative packet combining in distributed arrays. In *Wireless Communications and Networking, 2003. WCNC 2003. 2003 IEEE*, volume 2, pages 832 –837 vol.2, March 2003.

[10] Yaakov Bar-Shalom, X. Rong Li, and Thiagalingam Kirubarajan. *Estimation with Applications to Tracking and Navigation*. John Wiley and Sons, 2001.

[11] Yaakov Bar-Shalom, X. Rong Li, and Thiagalingam Kirubarajan. *Estimation with Applicatins to Tracking and Navigation*. John Wiley and Sons, 2001.

[12] N.C. Beaulieu and C. Leung. On the performance of three suboptimum detection schemes for binary signaling. *Communications, IEEE Transactions on*, 33(3):241–245, 1985.

[13] P. Bidigare, M. Oyarzun, D. Raeman, D. Cousins, D. Chang, R. O'Donnell, and D.R. Brown III. Implementation and demonstration of receiver-coordinated distributed transmit beamforming across an ad-hoc radio network. In *Proc. of the 46th Asilomar Conf. on Signals, Systems, and Computers*, pages 222–226, Pacific Grove, CA, November 4-7 2012.

[14] A. Bletsas. Evaluation of kalman filtering for network time keeping. *Ultrasonics, Ferroelectrics and Frequency Control, IEEE Transactions on*, 52(9):1452–1460, Sept 2005.

[15] Stephen Boyd and Lieven Vandenberghe. *Convex Optimization*. Cambridge University Press, 2004.

[16] Richard P. Brent. An algorithm with guaranteed convergence for finding a zero of a function. *The Computer Journal*, 14(4):422–425, 1971.

[17] D.R. Brown, P. Bidigare, and U. Madhow. Receiver-coordinated distributed transmit beamforming with kinematic tracking. In *Acoustics, Speech and Signal Processing (ICASSP), 2012 IEEE International Conference on*, pages 5209–5212, March 2012.

[18] D.R. Brown, R. Mudumbai, and S. Dasgupta. Fundamental limits on phase and frequency tracking and estimation in drifting oscillators. In *Acoustics, Speech and Signal Processing (ICASSP), 2012 IEEE International Conference on*, pages 5225–5228, March 2012.

[19] D.R. Brown, Boyang Zhang, B. Svirchuk, and Min Ni. An experimental study of acoustic distributed beamforming using round-trip carrier synchronization. In *Phased Array Systems and Technology (ARRAY), 2010 IEEE International Symposium on*, pages 316–323, October 2010.

[20] William C. Brown. The history of power transmission by radio waves. *Microwave Theory and Techniques, IEEE Transactions on*, 32(9):1230–1242, Sep 1984.

[21] D. R. Brown III, Min Ni, U. Madhow, and P. Bidigare. Distributed reception with coarsely-quantized observation exchanges. In *Information Sciences and Systems, 2013. CISS 2013. 47th Annual Conference on*, Mar 20-22. 2013.

[22] D. Richard Brown III, Upamanyu Madhow, Min Ni, Matthew Rebholz, and Patrick Bidigare. Distributed reception with hard decision exchanges. *Submitted to IEEE Transactions on Wireless Communications*, in review.

[23] Kenneth R Brown Jr. The theory of the gps composite clock. In *ION GPS-91; Proceedings of the 4th International Technical Meeting of the Satellite Division of the Institute of Navigation*, volume 1, pages 223–241, 1991.

[24] Siew Wah Chan, G.C. Goodwin, and Kwai Sang Sin. Convergence properties of the riccati difference equation in optimal filtering of nonstabilizable systems. *Automatic Control, IEEE Transactions on*, 29(2):110–118, Feb 1984.

[25] Chi-Tsong Chen. *Linear System Theory and Design*. Oxford University Press, 1999.

[26] Jinho Choi and Seungwon Choi. Cooperative and distributed receiver processing based on message passing. *Vehicular Technology, IEEE Transactions on*, 60(7):3066 –3075, September 2011.

[27] Thomas F. Coleman and Yuying Li. On the convergence of reflective newton methods for large-scale nonlinear minimization subject to bounds. *Mathematical Programming*, 67(2):189–224, 1994.

[28] Thomas F. Coleman and Yuying Li. An interior trust region approach for nonlinear minimization subject to bounds. *SIAM Journal on Optimization*, 6(2):418–445, 1996.

[29] Shuguang Cui, A.J. Goldsmith, and A. Bahai. Energy-constrained modulation optimization. *Wireless Communications, IEEE Transactions on*, 4(5):2349–2360, Sept 2005.

[30] Zhiguo Ding, Caijun Zhong, D.W.K. Ng, Mugen Peng, H.A. Suraweera, R. Schober, and H.V. Poor. Application of smart antenna technologies in simultaneous wireless information and power transfer. *Communications Magazine, IEEE*, 53(4):86–93, April 2015.

[31] D.R. Brown III, P. Bidigare, and U. Madhow. Receiver-coordinated distributed transmit beamforming with kinematic tracking. In *Acoustics, Speech and Signal Processing (ICASSP), 2012 IEEE International Conference on*, pages 5209–5212, March 2012.

[32] D.R. Brown III, Patrick Bidigare, Soura Dasgupta, and Upamanyu Madhow. Receiver-coordinated zero-forcing distributed transmit nullforming. In *Statistical Signal Processing Workshop (SSP), 2012 IEEE*, pages 269–272, August 2012.

[33] D.R. Brown III and R. David. Receiver-coordinated distributed transmit nullforming with local and unified tracking. In *Acoustics, Speech and Signal Processing (ICASSP), 2014 IEEE International Conference on*, pages 1160–1164, May 2014.

[34] D.R. Brown III and H.V. Poor. Time-slotted round-trip carrier synchronization for distributed beamforming. *IEEE Trans. on Signal Processing*, 56(11):5630–5643, November 2008.

[35] D.R. Brown III, U. Madhow, S. Dasgupta, and P. Bidigare. Receiver-coordinated distributed transmit nullforming with channel state uncertainty. In *Conf. Inf. Sciences and Systems (CISS2012)*, March 2012.

[36] A. Ephremides. Energy concerns in wireless networks. *Wireless Communications, IEEE Transactions on*, 9(4):48–59, Aug 2002.

[37] Zhaoxi Fang, Xiaojun Yuan, and Xin Wang. Distributed energy beamforming for simultaneous wireless information and power transfer in the two-way relay channel. *Signal Processing Letters, IEEE*, 22(6):656–660, June 2015.

[38] K. Finkenzeller. *RFID handbook: Fundamentals and applications in contactless smart cards and indentification*. Wiley Publishing, 2003.

[39] A. Fu, E. Modiano, and J.N. Tsitsiklis. Optimal transmission scheduling over a fading channel with energy and deadline constraints. *Wireless Communications, IEEE Transactions on*, 5(3):630–641, March 2006.

[40] Lorenzo Galleani. A tutorial on the 2-state model of the atomic clock noise. *Metrologia*, 45(6):S175–S182, December 2008.

[41] G. Giorgi and C. Narduzzi. Performance analysis of kalman filter-based clock synchronization in IEEE 1588 networks. In *International IEEE Symposium on Precision Clock Synchronization for Measurement, Control, and Communication*, pages 1–6, October 12-16 2009.

[42] G. Giorgi and C. Narduzzi. Performance analysis of kalman-filter-based clock synchronization in ieee 1588 networks. *Instrumentation and Measurement, IEEE Transactions on*, 60(8):2902–2909, Aug 2011.

[43] G. Giorgi and C. Narduzzi. Performance analysis of kalman-filter-based clock synchronization in ieee 1588 networks. *Instrumentation and Measurement, IEEE Transactions on*, 60(8):2902–2909, Aug 2011.

[44] P. Grover and A. Sahai. Shannon meets tesla: Wireless information and power transfer. In *Information Theory Proceedings (ISIT), 2010 IEEE International Symposium on*, pages 2363–2367, June 2010.

[45] Simon Haykin. *Communication Systems*. Wiley, 5th edition, 2009.

[46] Jian Hou, Gangfeng Yan, Zhiyun Lin, and Wenyuan Xu. Distributed transmit beamforming via feedback-based inter-cluster synchronization. In *Decision and Control (CDC), 2012 IEEE 51st Annual Conference on*, pages 1392–1397, Dec 2012.

[47] J. Hoydis, S. ten Brink, and M. Debbah. Massive mimo: How many antennas do we need? In *Communication, Control, and Computing (Allerton), 2011 49th Annual Allerton Conference on*, pages 545–550, 2011.

[48] K. Huang and V. K. N. Lau. Enabling wireless power transfer in cellular networks: Architecture, modeling and deployment. *IEEE Transactions on Wireless Communications*, 13(2):902–912, February 2014.

[49] S. Y. R. Hui, W. Zhong, and C. K. Lee. A critical review of recent progress in mid-range wireless power transfer. *IEEE Transactions on Power Electronics*, 29(9):4500–4511, Sept 2014.

[50] R. Irmer, H. Droste, P. Marsch, M. Grieger, G. Fettweis, S. Brueck, H.-P. Mayer, L. Thiele, and V. Jungnickel. Coordinated multipoint: Concepts, performance, and field trial results. *Communications Magazine, IEEE*, 49(2):102–111, february 2011.

[51] Jouya Jadidian and Dina Katabi. Magnetic MIMO: How to charge your phone in your pocket. In *Proceedings of the 20th Annual International Conference on Mobile Computing and Networking*, pages 495–506, 2014.

[52] D. R. Jones, C. D. Perttunen, and B. E. Stuckman. Lipschitzian optimization without the lipschitz constant. *J. Optim. Theory Appl.*, 79(1):157–181, October 1993.

[53] Hyungsik Ju and Rui Zhang. Throughput maximization in wireless powered communication networks. *Wireless Communications, IEEE Transactions on*, 13(1):418–428, January 2014.

[54] Hyungsik Ju and Rui Zhang. Throughput maximization in wireless powered communication networks. *Wireless Communications, IEEE Transactions on*, 13(1):418–428, January 2014.

[55] K. Kastella, R. Mudumbai, and T. Stevens. Frequency estimation in the presence of cycle slips: Filter banks and error bounds for phase unwrapping. In *Statistical Signal Processing Workshop (SSP), 2012 IEEE*, pages 277–280, Aug 2012.

[56] Chang-Gyun Kim, Dong-Hyun Seo, Jung-Sik You, Jong-Hu Park, and B. H. Cho. Design of a contactless battery charger for cellular phone. *IEEE Transactions on Industrial Electronics*, 48(6):1238–1247, Dec 2001.

[57] Chang-Gyun Kim, Dong-Hyun Seo, Jung-Sik You, Jong-Hu Park, and B. H. Cho. Design of a contactless battery charger for cellular phone. *IEEE Transactions on Industrial Electronics*, 48(6):1238–1247, Dec 2001.

[58] Hayang Kim, Xiaoli Ma, and Benjamin R Hamilton. Tracking low-precision clocks with time-varying drifts using kalman filtering. *Networking, IEEE/ACM Transactions on*, 20(1):257–270, 2012.

[59] W. Klepczynski and P. Ward. Frequency stability requirements for narrow band receivers. In *32nd Annual Precise Time and Time Interval Meeting*, November 2000.

[60] C. Komninakis, C. Fragouli, A.H. Sayed, and R.D. Wesel. Multi-input multi-output fading channel tracking and equalization using kalman estimation. *Signal Processing, IEEE Transactions on*, 50(5):1065–1076, May 2002.

[61] G. Kramer, M. Gastpar, and P. Gupta. Cooperative strategies and capacity theorems for relay networks. *IEEE Transactions on Information Theory*, 51(9):3037–3063, Sept 2005.

[62] G. Kramer, M. Gastpar, and P. Gupta. Cooperative strategies and capacity theorems for relay networks. *Information Theory, IEEE Transactions on*, 51(9):3037 – 3063, September 2005.

[63] A. Kumar, R. Mudumbai, S. Dasgupta, M. M. U. Rahman, D. R. Brown III, U. Madhow, and T. P. Bidigare. A scalable feedback mechanism for distributed nullforming with phase-only adaptation. *IEEE Transactions on Signal and Information Processing over Networks*, 1(1):58–70, March 2015.

[64] André Kurs, Aristeidis Karalis, Robert Moffatt, J. D. Joannopoulos, Peter Fisher, and Marin Soljačić. Wireless power transfer via strongly coupled magnetic resonances. *Science*, 317(5834):83–86, July 2007.

[65] Gerard Lachapelle, ME Cannon, and G Lu. High-precision gps navigation with emphasis on carrier-phase ambiguity resolution. *Marine Geodesy*, 15(4):253–269, 1992.

[66] J. N. Laneman, D. N. C. Tse, and G. W. Wornell. Cooperative diversity in wireless networks: Efficient protocols and outage behavior. *IEEE Transactions on Information Theory*, 50(12):3062–3080, Dec 2004.

[67] Erik G. Larsson, Fredrik Tufvesson, Ove Edfors, and Thomas L. Marzetta. Massive mimo for next generation wireless systems. *submitted to IEEE Communications Magazine*, abs/1304.6690, 2013.

[68] Bert Lenaerts and Robert Puers. *Omnidirectional Inductive Powering for Biomedical Implants*. Springer Publishing Company, Incorporated, 2008.

[69] Xin Li, T.F. Wong, and J.M. Shea. Bit-interleaved rectangular parity-check coded modulation with iterative demodulation in a two-node distributed array. In *Communications, 2003. ICC '03. IEEE International Conference on*, volume 4, pages 2812 – 2816 vol.4, May 2003.

[70] Xin Li, T.F. Wong, and J.M. Shea. Performance analysis for collaborative decoding with least-reliable-bits exchange on awgn channels. *Communications, IEEE Transactions on*, 56(1):58 –69, January 2008.

[71] Che Lin, V.V. Veeravalli, and S.P. Meyn. A random search framework for convergence analysis of distributed beamforming with feedback. *Information Theory, IEEE Transactions on*, 56(12):6133–6141, Dec 2010.

[72] Liang Liu, Rui Zhang, and Kee-Chaing Chua. Wireless information and power transfer: A dynamic power splitting approach. *Communications, IEEE Transactions on*, 61(9):3990–4001, September 2013.

[73] Vincent Liu, Aaron Parks, Vamsi Talla, Shyamnath Gollakota, David Wetherall, and Joshua R. Smith. Ambient backscatter: Wireless communication out of thin air. In *Proceedings of the ACM SIGCOMM 2013 Conference on SIGCOMM*, pages 39–50, 2013.

[74] X. Lu, P. Wang, D. Niyato, D. I. Kim, and Z. Han. Wireless networks with rf energy harvesting: A contemporary survey. *IEEE Communications Surveys Tutorials*, 17(2):757–789, 2015.

[75] R.K. Mehra. On the identification of variances and adaptive kalman filtering. *Automatic Control, IEEE Transactions on*, 15(2):175–184, Apr 1970.

[76] N. Michelusi, K. Stamatiou, and M. Zorzi. On optimal transmission policies for energy harvesting devices. In *Information Theory and Applications Workshop (ITA), 2012*, pages 249–254, Feb 2012.

[77] D.L. Mills, A. Thyagarajan, and B.C. Huffman. Internet timekeeping around the globe. In *Proc. Precision Time and Time Interval (PTTI) Applications and Planning Meeting*, pages 365–371, December 1997.

[78] K. Miwa, H. Mori, N. Kikuma, H. Hirayama, and K. Sakakibara. A consideration of efficiency improvement of transmitting coil array in wireless power transfer with magnetically coupled resonance. In *2013 IEEE Wireless Power Transfer (WPT)*, pages 13–16, May 2013.

[79] M. R. V. Moghadam and R. Zhang. Multiuser wireless power transfer via magnetic resonant coupling: Performance analysis, charging control, and power region characterization. *IEEE Transactions on Signal and Information Processing over Networks*, 2(1):72–83, March 2016.

[80] L. Mohjazi, M. Dianati, G.K. Karagiannidis, S. Muhaidat, and M. Al-Qutayri. RF-powered cognitive radio networks: technical challenges and limitations. *Communications Magazine, IEEE*, 53(4):94–100, April 2015.

[81] X. Mou and H. Sun. Wireless power transfer: Survey and roadmap. In *2015 IEEE 81st Vehicular Technology Conference (VTC Spring)*, pages 1–5, May 2015.

[82] R. Mudumbai, G. Barriac, and U. Madhow. On the feasibility of distributed beamforming in wireless networks. *IEEE Trans. Wireless Commun.*, 6(5):1754–1763, May 2007.

[83] R. Mudumbai, D.R. Brown, U. Madhow, and H.V. Poor. Distributed transmit beamforming: challenges and recent progress. *Communications Magazine, IEEE*, 47(2):102–110, February 2009.

[84] R. Mudumbai, S. Dasgupta, A. Kumar, B. Peiffer, U. Madhow, and D.R. Brown III. Wideband retrodirective distributed transmit beamforming with endogenous relative calibration. In *Signals, Systems and Computers, 2015 49th Asilomar Conference on*, Nov 2015.

[85] R. Mudumbai, D.R. Brown III, U. Madhow, and H.V. Poor. Distributed transmit beamforming: Challenges and recent progress. *IEEE Communications Magazine*, 47(2):102–110, February 2009.

[86] R. Mudumbai, J. Hespanha, U. Madhow, and G. Barriac. Scalable feedback control for distributed beamforming in sensor networks. In *IEEE International Symp. on Information Theory (ISIT)*, pages 137–141, Adelaide, Australia, September 2005.

[87] R. Mudumbai, J. Hespanha, U. Madhow, and G. Barriac. Distributed transmit beamforming using feedback control. *IEEE Trans. on Information Theory*, 56(1):411–426, January 2010.

[88] R. Mudumbai, B. Wild, U. Madhow, and K. Ramchandran. Distributed beamforming using 1 bit feedback: from concept to realization. In *44th Allerton Conf. on Comm., Control, and Computing*, pages 1020–1027, Monticello, IL, September 2006.

[89] Raghuraman Mudumbai, Ben Wild, Upamanyu Madhow, and Kannan Ramch. Distributed beamforming using 1 bit feedback: From concept to realization. In *in Allerton Conference on Communication, Control, and Computing*, 2006.

[90] J. O. Mur-Miranda, G. Fanti, Y. Feng, K. Omanakuttan, R. Ongie, A. Setjoadi, and N. Sharpe. Wireless power transfer using weakly coupled magnetostatic resonators. In *2010 IEEE Energy Conversion Congress and Exposition*, pages 4179–4186, Sept 2010.

[91] J. Murakami, F. Sato, T. Watanabe, H. Matsuki, S. Kikuchi, K. Harakawa, and T. Satoh. Consideration on cordless power station-contactless power transmission system. *IEEE Transactions on Magnetics*, 32(5):5037–5039, Sep 1996.

[92] P. J. Napier, A. R. Thompson, and R. D. Ekers. The very large array: Design and performance of a modern synthesis radio telescope. *Proceedings of the IEEE*, 71(11):1295–1320, Nov 1983.

[93] R. P. Narrainen and F. Takawira. Performance analysis of soft handoff in cdma cellular networks. *IEEE Transactions on Vehicular Technology*, 50(6):1507–1517, Nov 2001.

[94] A. Nayagam, J.M. Shea, and T.F. Wong. Collaborative decoding in bandwidth-constrained environments. *Selected Areas in Communications, IEEE Journal on*, 25(2):434 –446, February 2007.

[95] D. W. K. Ng, E. S. Lo, and R. Schober. Wireless information and power transfer: Energy efficiency optimization in OFDMA systems. *IEEE Transactions on Wireless Communications*, 12(12):6352–6370, December 2013.

[96] D. W. K. Ng and R. Schober. Secure and green SWIPT in distributed antenna networks with limited backhaul capacity. *IEEE Transactions on Wireless Communications*, 14(9):5082–5097, Sept 2015.

[97] K. Ota, H. Mizutani, R. Ishikawa, and K. Honjo. Bi-directional wireless power transfer technology for wireless sensor/power networks. In *2013 IEEE-APS Topical Conference on Antennas and Propagation in Wireless Communications (APWC)*, pages 786–789, Sept 2013.

[98] Ipek Ozil and D.R. Brown III. Time-slotted round-trip carrier synchronization. In *Proceedings of the 41st Asilomar Conference on Signals, Systems, and Computers*, pages 1781–1785, Pacific Grove, CA, November 4-7 2007.

[99] Joseph A. Paradiso and Thad Starner. Energy scavenging for mobile and wireless electronics. *IEEE Pervasive Computing*, 4(1):18–27, 2005.

[100] A.N. Parks, A.P. Sample, Yi Zhao, and J.R. Smith. A wireless sensing platform utilizing ambient RF energy. In *Radio and Wireless Symposium (RWS), 2013 IEEE*, pages 331–333, Jan 2013.

[101] William H. Press, Saul A. Teukolsky, William T. Vetterling, and Brian P. Flannery. *Numerical Recipes 3rd Edition: The Art of Scientific Computing.* Cambridge University Press, 3 edition, 2007.

[102] R. Preuss and D.R. Brown III. Two-way synchronization for coordinated multi-cell retrodirective downlink beamforming. *IEEE Trans. Signal Process.*, 59(11):5415–5427, November 2011.

[103] R.D. Preuss and D.R. Brown III. Retrodirective distributed transmit beamforming with two-way source synchronization. In *Information Sciences and Systems (CISS), 2010 44th Annual Conference on*, pages 1–6, March 2010.

[104] C. Qiu, K. T. Chau, C. Liu, and C. C. Chan. Overview of wireless power transfer for electric vehicle charging. In *2013 World Electric Vehicle Symposium and Exhibition (EVS27)*, pages 1–9, Nov 2013.

[105] Rakon RFPO45 SMD oven controlled crystal oscillator datasheet, 2009.

[106] D.C. Rife and R.R. Boorstyn. Single-tone parameter estimation from discrete-time observations. *IEEE Trans. Inf. Theory*, 20(5):591–598, September 1974.

[107] A. Sample and J.R. Smith. Experimental results with two wireless power transfer systems. In *Radio and Wireless Symposium, 2009. RWS '09. IEEE*, pages 16–18, Jan 2009.

[108] A. Sanderovich, S. Shamai, Y. Steinberg, and G. Kramer. Communication via decentralized processing. *IEEE Transactions on Information Theory*, 54(7):3008–3023, July 2008.

[109] A. Sanderovich, S. Shamai, Y. Steinberg, and G. Kramer. Communication via decentralized processing. *Information Theory, IEEE Transactions on*, 54(7):3008 –3023, July 2008.

[110] Edward Sazonov and Michael R. Neuman, editors. *Wearable Sensors: Fundamentals, Implementation and Applications*. Academic Press, Oxford, 2014.

[111] A. Scaglione, D. L. Goeckel, and J. N. Laneman. Cooperative communications in mobile ad hoc networks. *IEEE Signal Processing Magazine*, 23(5):18–29, Sept 2006.

[112] D. Scherber, R. O'Donnell, M. Rebholz, M. Oyarzun, C. Obranovich, W. Kulp, P. Bidigare, and D.R. Brown III. Coherent distributed techniques for tactical radio networks: Enabling long range communications with reduced size, weight, power and cost. In *MILCOM 2013*, San Deigo, CA, November 18-20 2013.

[113] A. Sendonaris, E. Erkip, and B. Aazhang. User cooperation diversity. part i. system description. *IEEE Transactions on Communications*, 51(11):1927–1938, Nov 2003.

[114] A. Sendonaris, E. Erkip, and B. Aazhang. User cooperation diversity. part ii. implementation aspects and performance analysis. *IEEE Transactions on Communications*, 51(11):1939–1948, Nov 2003.

[115] A. F. M. Shahen Shah and Md. Shariful Islam. A survey on cooperative communication in wireless networks. *International Journal of Intelligent Systems and Applications(IJISA)*, 6(7):66–78, June 2014.

[116] Z. Sheng, Z. Ding, and K. K. Leung. Distributed and power efficient routing in wireless cooperative networks. In *2009 IEEE International Conference on Communications*, pages 1–5, June 2009.

[117] Y.S. Shmaliy. An unbiased fir filter for tie model of a local clock in applications to gps-based timekeeping. *Ultrasonics, Ferroelectrics, and Frequency Control, IEEE Transactions on*, 53(5):862–870, May 2006.

[118] Paris Smaragdis and Petros Boufounos. Learning source trajectories using wrapped-phase hidden markov models. In *Applications of Signal Processing to Audio and Acoustics, 2005. IEEE Workshop on*, pages 114–117. IEEE, 2005.

[119] J. R. Smith. *Wirelessly Powered Sensor Networks and Computational RFID*. Springer, 2013.

[120] S.R. Stein and R.L. Filler. Kalman filter analysis for real time applications of clocks and oscillators. In *Frequency Control Symposium, 1988., Proceedings of the 42nd Annual*, pages 447–452, Jun 1988.

[121] S. Sudevalayam and P. Kulkarni. Energy harvesting sensor nodes: Survey and implications. *Communications Surveys Tutorials, IEEE*, 13(3):443–461, Mar 2011.

[122] J.G. Sun. Sensitivity analysis of the discrete-time algebraic riccati equation. *Linear Algebra and its Applications*, 275-276:595–615, 1998.

[123] Tianjia Sun, Xiang Xie, and Zhihua Wang. *Wireless Power Transfer for Medical Microsystems*. Springer Publishing Company, Incorporated, 2013.

[124] Vamsi Talla, Bryce Kellogg, Benjamin Ransford, Saman Naderiparizi, Shyamnath Gollakota, and Joshua R. Smith. Powering the next billion devices with Wi-Fi. Preprint, 14 pages, available online arXiv:1505.06815v1, 2015.

[125] N. Tesla. Apparatus for transmitting electrical energy., December 1 1914. US Patent 1,119,732.

[126] Anuradha Tomar and Sunil Gupta. Wireless power Transmission: Applications and Components. *International Journal of Engineering Research & Technology*, 1(5), July 2012.

[127] T.C. Tozer and J. Kollerstrom. Penalties of hard decision in signal detection. *Electronics Letters*, 16(5):199–200, 1980.

[128] J. Traa and P. Smaragdis. A wrapped kalman filter for azimuthal speaker tracking. *Signal Processing Letters, IEEE*, 20(12):1257–1260, Dec 2013.

[129] Y.S. Tu and G.J. Pottie. Coherent cooperative transmission from multiple adjacent antennas to a distant stationary antenna through AWGN channels. In *IEEE Vehicular Technology Conf. (VTC)*, volume 1, pages 130–134, Birmingham, AL, May 2002.

[130] L.R. Varshney. Transporting information and energy simultaneously. In *Information Theory, 2008. ISIT 2008. IEEE International Symposium on*, pages 1612–1616, July 2008.

[131] R. Vaze and K. Jagannathan. Finite-horizon optimal transmission policies for energy harvesting sensors. In *Acoustics, Speech and Signal Processing (ICASSP), 2014 IEEE International Conference on*, pages 3518–3522, May 2014.

[132] A. J. Viterbi, A. M. Viterbi, K. S. Gilhousen, and E. Zehavi. Soft handoff extends cdma cell coverage and increases reverse link capacity. *IEEE Journal on Selected Areas in Communications*, 12(8):1281–1288, Oct 1994.

[133] Y. w. Hong, W. j. Huang, F. h. Chiu, and C. c. J. Kuo. Cooperative communications in resource-constrained wireless networks. *IEEE Signal Processing Magazine*, 24(3):47–57, May 2007.

[134] I. H. Wang and D. N. C. Tse. Interference mitigation through limited receiver cooperation: Symmetric case. In *Information Theory Workshop, 2009. ITW 2009. IEEE*, pages 579–583, Oct 2009.

[135] I-Hsiang Wang and D.N.C. Tse. Interference mitigation through limited receiver cooperation: Symmetric case. In *Information Theory Workshop, 2009. ITW 2009. IEEE*, pages 579 –583, October 2009.

[136] R. Wang and D. R. Brown. Throughput maximization in wireless powered communication networks with energy saving. In *2014 48th Asilomar Conference on Signals, Systems and Computers*, pages 516–520, Nov 2014.

[137] Rui Wang and D.R. Brown III. Feedback rate optimization in receiver-coordinated distributed transmit beamforming for wireless power transfer. In *Information Sciences and Systems (CISS), 2015 49th Annual Conference on*, March 2015.

[138] X.C. Wei and E.P. Li. Simulation and experimental comparison of different coupling mechanisms for the wireless electricity transfer. *Journal of Electromagnetic Waves and Applications*, 23(7):925–934, 2009.

[139] Robert L. Williams II and Douglas A. Lawrence. *Linear State-Space Control Systems*. Wiley, 2007.

[140] T.F. Wong, Xin Li, and J.M. Shea. Distributed decoding of rectangular parity-check code. *Electronics Letters*, 38(22):1364 – 1365, October 2002.

[141] T.F. Wong, Xin Li, and J.M. Shea. Iterative decoding in a two-node distributed array. In *MILCOM 2002. Proceedings*, volume 2, pages 1320 – 1324 vol.2, October 2002.

[142] Liguang Xie, Yi Shi, Y.T. Hou, and A. Lou. Wireless power transfer and applications to sensor networks. *Wireless Communications, IEEE*, 20(4):140–145, August 2013.

[143] Jie Xu, Liang Liu, and Rui Zhang. Multiuser MISO beamforming for simultaneous wireless information and power transfer. *Signal Processing, IEEE Transactions on*, 62(18):4798–4810, Sept 2014.

[144] Jie Xu and Rui Zhang. Energy beamforming with one-bit feedback. *Signal Processing, IEEE Transactions on*, 62(20):5370–5381, Oct 2014.

[145] G. Yang, M. R. V. Moghadam, and R. Zhang. Magnetic beamforming for wireless power transfer. In *2016 IEEE International Conference on Acoustics, Speech and Signal Processing (ICASSP)*, pages 3936–3940, March 2016.

[146] S. Yi, S. Kalyanaraman, B. Azimi-Sadjadi, and H.Y. Shen. Energy-efficient cluster-based cooperative fec in wireless networks. *Wireless Networks*, 15(8):965–977, November 2009.

[147] Su Yi, B. Azimi-Sadjadit, S. Kalyanaraman, and V. Subramanian. Error control code combining techniques in cluster-based cooperative wireless networks. In *Communications, 2005. ICC 2005. 2005 IEEE International Conference on*, volume 5, pages 3510 – 3514 Vol. 5, May 2005.

[148] K. Zarifi, S. Affes, and A. Ghrayeb. Collaborative null-steering beamforming for uniformly distributed wireless sensor networks. *IEEE Trans. on Signal Processing*, 58(3):1889 –1903, Mar. 2010.

[149] Rui Zhang and Chin Keong Ho. Mimo broadcasting for simultaneous wireless information and power transfer. *Wireless Communications, IEEE Transactions on*, 12(5):1989–2001, May 2013.

[150] Rui Zhang and Chin Keong Ho. MIMO broadcasting for simultaneous wireless information and power transfer. *Wireless Communications, IEEE Transactions on*, 12(5):1989–2001, May 2013.

[151] Xun Zhou, Rui Zhang, and Chin Keong Ho. Wireless information and power transfer: Architecture design and rate-energy tradeoff. *Communications, IEEE Transactions on*, 61(11):4754–4767, November 2013.